DEVELOPMENT OF MICROFLUIDIC MODULES FOR DNA PURIFICATION VIA PHENOL EXTRACTION AND ANALYTE CONCENTRATION USING TRANSVERSE ELECTROKINETICS

by

MERCEDES C. MORALES

A dissertation submitted to the

Graduate School-New Brunswick

Rutgers, The State University of New Jersey

and

The Graduate School of Biomedical Sciences

University of Medicine and Dentistry of New Jersey

In partial fulfillment of the requirements

For the degree of

Doctor of Philosophy

Graduate Program in Biomedical Engineering

Written under the direction of

Professor Jeffrey D. Zahn

And approved by

_____

_____

_____

_____

New Brunswick, New Jersey

January, 2012

ABSTRACT OF THE DISSERTATION

DEVELOPMENT OF MICROFLUIDIC MODULES FOR DNA PURIFICATION VIA PHENOL EXTRACTION AND ANALYTE CONCENTRATION USING TRANSVERSE ELECTROKINETICS

By MERCEDES C. MORALES

Dissertation Director: Professor Jeffrey D. Zahn

In this work, microfluidic platforms have been designed and evaluated to demonstrate microscale DNA purification via organic (phenol) extraction as well as analyte trapping and concentration using a transverse electrokinetic force balance.

First, in order to evaluate DNA purification via phenol extraction in a microdevice, an aqueous phase containing protein and DNA and an immiscible receiving organic phase were utilized to evaluate microfluidic DNA extraction under both stratified and droplet-based flow conditions using a serpentine microfluidic device. The droplet based flow resulted in a significant improvement of protein partitioning from the aqueous phase due to the flow recirculation inside each droplet improving material convective transport into the organic phase. The plasmid recovery from bacterial lysates using droplet-based flow was high (>92%) and comparable to the recovery achieved using commercial DNA purification kits and standard macroscale phenol extraction.

Second, a converging Y-inlet microfluidic channel with integrated coplanar electrodes was used to investigate transverse DNA and protein migration under uniform direct current (DC) electric fields. Negatively charged samples diluted in low and high ionic

strength buffers were co-infused with a receiving buffer of the same ionic strength into a main channel where transverse electric fields were applied. Experimental results demonstrated that charged analytes could traverse the channel width and accumulate at the positive bias electrode in a low electroosmotic mobility and high electrophoretic mobility condition (high ionic strength buffer) or migrated towards an equilibrium position within the channel when both electroosmotic mobility and electrophoretic mobility are high (low ionic strength buffer). The different behaviors are the result of a balance between the electrophoretic force and a drag force induced by a recirculating electroosmotic flow generated across the channel width due to the bounding walls.

The miniaturization of DNA phenol extraction and the novel electrokinetic trapping techniques presented in this research are the initial steps towards an efficient DNA sample preparation chip which could be integrated with post-extraction DNA manipulations for genomic analysis modules such as capillary electrophoretic separations.

ACKNOWLEDGEMENTS

First at all, I would like to thank my advisor, Professor Jeffrey Zahn. He gave me the opportunity to get involved in stimulating laboratory experiences that made me acquire technical skills as well as inspire my creativity. His mentorship and continuous encouragement have helped me to stay motivated and guided me during the process of this research.

In the same way, I want to thank Professor Hao Lin for his guidance as a member of my committee, and Professor Li Cai and Professor Laura Fabris for providing helpful comments and advises to this research.

I thank all my colleagues at the Biomedical Engineering Department for making my work in the lab more enjoyable. I would like to specially acknowledge Larry Sasso, Kiana Aran, Alex Fok, Jack Zheng and Jean Lo, for their support, help and sense of humor.

In addition, I would like to express my sincere appreciation to the faculty and administrative staff at the Biomedical Engineering Department for their advice and help during these years.

Thanks to all my friends in Argentina, in the United States and now in other countries for all their support during this time. Thank you Nuria, Nachi, Valeria, Greg, Jose, Loreto, Bahar, Chris, Marcos, Rocio, Alberto and Mosteiro family.

A gigantic thank-you goes to Mete Rodoper for all his care, enormous patience and companionship during these years.

Finally, I would like to acknowledge and give my profound gratitude to my parents Eduardo and Consuelo and my siblings Eduardo, Cecilia and Julieta for their support and encouragement from a distance that kept me standing in the darkest times.

DEDICATION

A mis dos gigantes, mis padres, Eduardo y Consuelo

por todo su amor, educación y apoyo.

To my two giants, my parents, Eduardo and Consuelo

for all their love, education and support.

TABLE OF CONTENTS

LIST OF TABLES

LIST OF ILLUSTRATIONS

Chapter 1

Introduction

1.1 Significance of DNA Purification

Since recombinant DNA technology development, DNA has been recognized as an important component for biological and biomedical research because of its ability to code for proteins and enzymes required for cell life, replication and adaptation to changing environments as well as establishing the genetic basis of disease. DNA-based studies and genetic engineering have greatly benefited from DNA's chemical stability, ease of manipulation and analysis. DNA is purified from cells (bacterial or eukaryotic) or tissue lysates, cut into individual fragments using highly specific restriction endonucleases, amplified via polymerase chain reaction (PCR) and analyzed by gel electrophoresis and southern blotting techniques.

Nucleic acid purification is widely utilized in a large number of applications throughout the biomedical sciences. Some of these applications are important health-related areas in where detection of specific DNA fingerprints is required including: the determination of genetic markers or gene mutations implicated in diseases such as sickle cell anemia or the identification of certain gene alleles which increase the risk of certain cancers,

genotyping of viral infections in humans, such as influenza, human immunodeficiency virus (HIV), or hepatitis C virus (HCV) to direct treatment options, as well as the detection of biowarfare agents.

In addition to the biomedical sciences applications, the discovery of DNA has resulted in tremendous advances in agriculture; for example, where it is being use to genetically modify the seeds to create crops with attributes that they do not have naturally. By manipulating plant genes, agricultural yields have been improved achieving much higher productivity and pest-resistant varieties.

DNA can be also used to investigate historic and prehistoric events. By reconstructing gene changes and homology, modifications in DNA sequences can provide useful information to understand how a specie evolves in time. In addition, since mitochondrial DNA is passed on through the maternal lineage, it has been used to trace the migration of humans over the planet.

In addition, the use of DNA for identification of people is largely utilized in forensics which represent fundamental criminal evidence as well as in paternity and maternity disputes through genetic finger printing of specific DNA polymorphisms found in the human genome. A particular and important example of DNA analysis is the development of DNA-based identity test which has recently provided valuable information for identification of missing people during catastrophes or massive attacks, such as the identification of September 11th victims.

An area that also became important is the use of DNA analysis for defense; DNA analysis for rapid and unequivocal detection of potential biological warfare agents is a

major objective for military authorities and has been used to trace the anthrax spores used in the 2001 attacks.

Also, another growing area for DNA extraction is nucleic acid-based pathogen detection in processed and unprocessed food products [1]. The presence of pathogenic bacteria can cost consumers and the food industry many millions of dollars every year due to food recalls and can cause many deaths each year around the world. Therefore, the rapid bacterial detection by DNA-based analysis could help stop distribution of contaminated foodstuffs.

As can be recognized, there are multiple areas of applications that can benefit from advances in DNA preparation techniques. With recent developments in microfluidic technologies, standard DNA extraction protocols can be improved by using smaller and faster devices which can be integrated with other processes such as downstream PCR amplification or capillary electrophoresis (CE) separation [2, 3] in a more integrated, automated and compact fashion to allow autonomous sample preparation and analysis modules. By using modern engineering technologies developed for the microchip fabrication in the last decades, it is now possible to make the process of DNA isolation, purification and analysis much faster, less expensive and more portable.

Focusing on the biomedical applications, the healthcare sector can greatly benefit by rapid nucleic acid-based tests when fast diagnostics play a crucial role in saving people's lives. One example is the rapid pathogenic agent detection to avoid epidemics. In isolated and poor regions, the portability and inexpensive characteristics of lab-on-chip technologies can make a significant improvement in rural health clinics. The use of low volumes in comparison with standard methods makes this emerging technology suitable

for situations where the biological sample available is scarce such as in prenatal and neonatal DNA diagnosis. Finally, this new technology brings the possibility of integration and automation of multiple and complex analytical processes required in biological diagnosis into a single platform and allowing more reliable results.

1.2 The Need for Sample Pre-concentration

As mentioned above, the growing developments of microfluidic technologies in recent decades have guided a paradigm shift in the way chemical and biological samples can be analyzed. Significant research efforts have been undertaken to develop miniaturized platforms to purify, amplify, separate and analyze DNA in microchannels, with additional efforts considering other important analytes like proteins, cells, organelles, and bacteria.

One important challenge as assay scale decreases is the sample pre-concentration which often must be investigated to improve the sensitivity of a microchip assay. Usually a pre-conditioning of the sample needs to be conducted prior the sample analysis to assure purity and a minimal concentration required to provide an unequivocal detection. Besides the enhancement in the detection sensitivity, sample pre-concentration also improves the reliability of analysis by increasing the signal-to-noise ratio.

Along these lines, numerous microfluidic approaches have been investigated for concentrating dilute analytes for example prior to micro-capillary electrophoretic (μCE) separations in order to increase the signal at the output of the device. In some applications, pre-conditioning of samples is critical to increase an analyte concentration above the detection limit or to improve sample injection reproducibility which can be

negatively affected by diffusion, hydrodynamic and electrodynamic broadening, Joule heating, and electromigration dispersion [4].

Different researchers have suggested several mechanisms for pre-concentration. Some of methods for both DNA and proteins have included using electrokinetic phenomena such as electrophoresis, electroosmosis and dielectrophoresis. For example, microfluidic devices have been developed to investigate electrophoretic sample stacking techniques including field-amplified sample stacking (FASS), isotachophoresis (ITP), and pH-mediated stacking which are one successful example of the necessary preconditioning step prior an efficient electrophoretic sample analysis. In addition to this, other concentration mechanisms such as the use of specific chemical binding of DNA to a solid phase or utilization of size exclusion membranes have been also exploited. A review of these methods can be found in Chapter 4.

The trapping and concentration of analytes are needed in multiple biomedical applications. The most extended use is as μCE preconditioning step that helps to achieve minimal concentration limits and enhance signal-to noise ratio prior the electrophoretic separation and analysis. Another important use is to maintain the sample of interest concentrated and separated from contaminants or undesired substances. For instance, electrokinetic methods have been used to isolate and sort cell components [5]. Additionally, having the sample locally constrained could be useful to enhance chemical reactions as other chemicals are infused conjunctly.

1.3 Dissertation Overview

In this work two main ideas have been explored. The first part of this dissertation refers to the design, fabrication, and performance of microfluidic devices used as platform for DNA extraction by organic solvents. The main aims were to quantify protein partitioning between the aqueous and the organic phase and DNA purification within the device, and to evaluate two modes of extraction, passive diffusion through stratified flows and droplet enhancement of extraction efficiency. The second part of this work is focused in the behavior of DNA and other analytes during the application of transverse electric fields. The main aims for this section were to understand the forces involved in the electrokinetic migration of DNA under transverse fields and to investigate the buffer solution influence in the analyte migration and concentration.

In chapter one, an introduction to the DNA extraction significance in the biomedical field and the need for sample pre-concentration are addressed to understand the importance and relevance of the research.

The second chapter presents an overview of the DNA extraction methods, a state-of-art review of recent research towards DNA extraction chips, the theoretical framework for two-phase systems in microfluidic devices, the partitioning mechanism and lastly, different mixing methods to enhance protein partition.

Chapter three examines the criteria used to design the DNA extraction devices, the fabrication process and the materials used in the experiments followed by the results obtained from experiments. Protein partitioning and DNA purification were analyzed for stratified flows and droplet-based flows in this section. A DNA recovery comparison

between the designed microfluidic device, standard phenol extraction and a commercial extraction kit was made by using bacterial lysates and summarized in this chapter.

In chapter four, as an introduction to the second part of this dissertation, an introduction to electrokinetic theory is provided which will be useful to understand the trapping mechanisms of the sample pre-concentration module presented in Chapter 5. In addition, a review of different sample trapping and concentration enhancement methods is presented.

Chapter five contains the fabrication methods of the device proposed including the embedded electrode traces manufacture. The sample and buffers utilized are detailed in this chapter as well as the buffer characterization. The results obtained using transverse electric fields and the different trapping mechanisms are explained in this section.

In chapter six the results obtained for DNA extraction via phenol extraction and sample pre-concentration using transverse electrokinetic forces are summarized and discussed. Finally, future prospects for improving this research and steps required towards creating integrated DNA extraction and analysis devices are addressed.

Chapter 2

Background of DNA Liquid Extraction

2.1 Standard DNA extraction methods

DNA can be separated and purified by two leading methods; by using organic solvents, also called phenol extraction, and by solid-phase-based extraction techniques. A description of these two methods is provided:

Phenol Extraction

Phenol extraction is an organic-aqueous liquid extraction technique that separates DNA and RNA from cellular components and proteins based on their affinity to different immiscible solvent phases. The procedure consists of the digestion and lysis of cells or tissue, mixing of the phases where proteins and lipids segregate into the organic phase while DNA stays in the aqueous phase, microcentrifugation, separation and precipitation of DNA with ethanol [6].

First, the cell lysis takes place which is a process of breaking open cells to release the DNA into the solution and leave it accessible. Typical methods include the use of

protease enzymes, chemical agent such as detergents, or mechanical disruption of cell membranes.

Second, the extraction is usually prepared in a 1.5 ml microcentrifuge tube with a minimum volume of 100 µl required for easy manipulation with micropipette tools. The aqueous sample with the lysed cell extract and an equal volume of phenol:chloroform:isoamyl alcohol (25:24:1 v/v) are incorporated into the tube and vortexed vigorously for 5 minutes to mix the phases. During this process, the cell components distribute into either the aqueous phase or the organic phase in order to minimize interaction energies. The cell membrane lipid components and proteins will partition to the organic phase and DNA will stay in the aqueous phase due to its polar nature having greater affinity to the aqueous phase. The separation occurs at the organic-aqueous interface. Increasing the interfacial interaction area is central to maximize the effective partitioning. In macroscopic systems this is accomplished through the vortex mixing.

Following partitioning, centrifugation is the next step to separate the two phases by density differences. The aqueous phase, the upper one in the tube due to its lower density, is now removed with a micropipette tool. This extraction and centrifugation process can be repeated to remove more components and to completely separate the phases.

The aqueous phase is then mixed with 2.5 volumes of ice cold 100% ethanol, and microcentrifuged at high speed which precipitates the DNA into a pellet. The supernatant solution is removed. Finally, 70%-80% ethanol is added, mixed and discarded to wash the remaining pellet removing excess salts. After washing, the DNA is resuspended in 50-100 µl of Tris-EDTA (TE) buffer.

Solid Phase Extraction (SPE)

This technique is based on the absorption of DNA onto a silica solid phase under high chaotropic salt concentration condition to separate DNA from the cell components. Many purification kits are commercially available (e.g. Qiagen, Promega, Biorad, Epicentre). Commercial kits usually utilize solid phases like silica gel, glass matrix, or membranes to bind and purify DNA. The main steps for solid phase extraction are lysis of the cells, absorption of DNA, washing, and elution of DNA [7].

Cell lysis is done under alkaline conditions and the solution is then loaded into the purification kit which consists of a packed silica column. In presence of high concentration chaotropic salts, the DNA binds to the silica surface because of electrostatic shielding between the DNA and the silica surface while other cell components do not bind.

A washing step is required after the DNA adsorption to flush proteins and other contaminants from the column. Via the introduction of an elution buffer, the purified DNA is then recovered at low salt concentration which promotes the detachment of the DNA molecules from silica.

When comparing these two techniques advantages and disadvantages to each procedure can be found. SPE does not have the inconvenience of dealing with organic solvents like phenol extraction. Residual phenol can denature protein and quench further chemical reactions if phenol contamination is present. However, solid phase extraction is limited by the exposed surface area to which DNA can attach to and the extraction efficiency

obtained with this technique is lower than the phenol extraction-ethanol precipitation procedure and is more susceptible to protein contamination due to non-specific binding. Furthermore, SPE is a fundamentally batch process requiring sequential introduction of solutions over a fixed column, whereas liquid extractions have the possibility to be run under continuous flow conditions.

2.2 Microfluidic DNA Extraction

The transfer of traditional analytical techniques into microscale platforms has allowed the automation and optimization of analytical processes and point-of-care medical systems. For this reason, integrating cell lysis, purification, amplification and analysis of nucleic acids into a micrototal analytical system (μTAS) represents the driving goal of many research groups all over the world. Microfluidic approaches towards integrating DNA handling processes have focused mainly on miniaturization of solid phase extraction, studying different materials, and microfabrication methodologies to bind DNA efficiently. Some approaches are reviewed here:

Silicon pillars

In 1999, Christel et al. developed of a cartridge where lysed cells are introduced into a DNA purification module followed by a PCR amplification module [8, 9]. The DNA extraction chip consists of silicon pillars, made by deep reactive ion etching (DRIE), where DNA binds (Fig. 2.1a). The use of these columns increases the surface area to volume ratio, providing a high binding capacity which is approximately 40 ng/cm^2.

Washing and elution step are incorporated to the chip as well as PCR thermal cycles to amplify DNA quantities in cases of low concentration samples. The integrated cartridge with the different process chambers is shown in Fig. 2.1b. The extraction efficiency was found about 50% using bacteriophage λ DNA as the target and DNA extraction was successful with both low and high concentrations of DNA samples (100-1000 ng/ml).

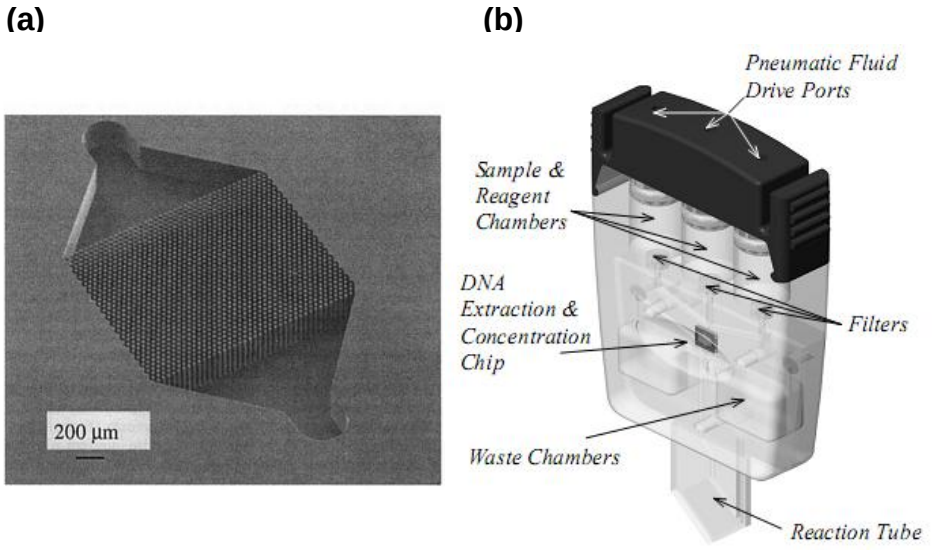

Figure 2.1: (a) SEM photograph of a pillar-based DNA extraction chip. (b) Integrated microfluidic cartridge containing the pillar-based DNA chip and a PCR reaction tube [8, 9].

Silica bead/sol-gel systems

Another solid phase that has been explored is silica beads in order to enhance the surface area. In 2003, Landers's group proposed silica beads immobilized within a sol-gel instead of silicon or glass pillars [10]. Beads packed in the microfluidic device increase the absorption area where DNA will bind. The channel is first loaded with the beads and then

filled with sol-gel to immobilize the silica particles (Fig. 2.2C) that involves the transition of the solution form liquid (colloidal “sol”) into solid form (“gel”). In addition, to keep the beads trapped in the device, the gel helps keep them separated, avoiding clogging, and increases the effective absorption surface area. The chip consists of a simple channel as shown in Fig. 2.2A. It requires an outside lysis step and external loading of sample, washing buffer, and elution buffer. This device was tested with blood and bacterial samples and has demonstrated an extraction efficiency of 50% for human genomic DNA and 70% for λ DNA [10].

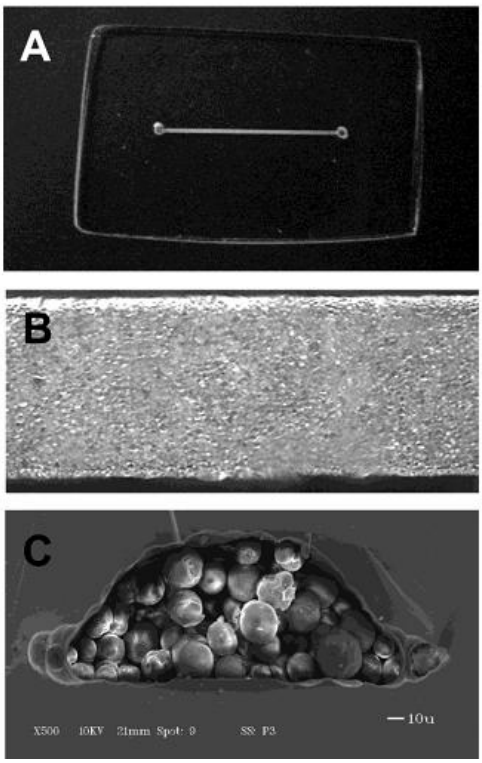

Figure 2.2: Silica particle-based microchip with sol-gel immobilization. A) 1x magnification; B) 10x magnification; C) 500x magnification of cross section [10].

In 2004, Quake's group presented a fully integrated microfluidic device using silica beads loaded previously to the chip where DNA samples are attached and eluted by the use of pneumatic valves [11]. The DNA extraction is followed by PCR amplification to achieve minimal concentration for analysis. The fabricated integrated chip was made using soft lithography techniques and all the processes involved in the purification of nucleic acids were integrated in one chip (Fig 2.3) [11].

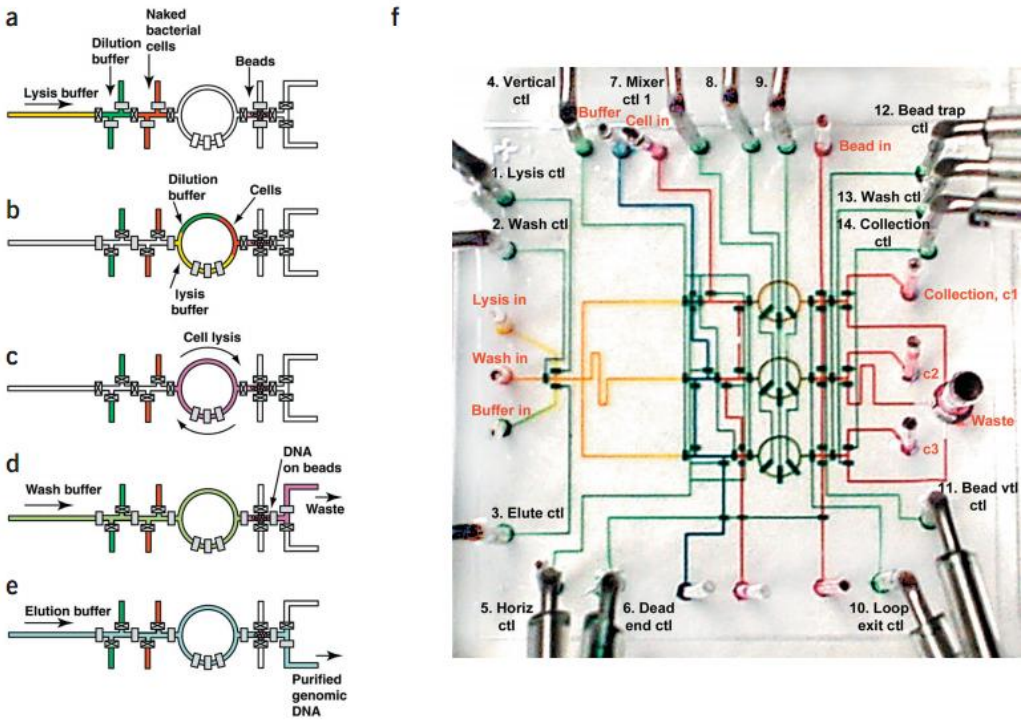

Figure 2.3: (a)-(e) Schematic steps of bacteria lysis and DNA purification process. (f) Image of the DNA microfluidic chip with parallel architecture [11].

By external pneumatic activation, valves can control the trafficing of the different buffers and samples to the corresponding chamber, and isolate units from the rest of the chip. The main units are lysis buffer chamber, dilution chamber, and cell chamber. In Fig 2.3a, cell sample, dilution buffer and lysis buffer are introduced first into the device and

pumped through a rotary mixer which is also controlled by hydraulic valves that constantly open and close the entrance of fluids. The function of this step is to mix the components and reduce the time taken for lysis of the cells. Then, the mixture is flushed over beads which are preloaded in the device. DNA binds the beads and a washing buffer is used to flush the waste. Finally, the elution buffer is added and DNA is collected. In this fully automatic fashion, DNA extraction can be performed with a very little user handling.

Other novel phases

More recently, other phases have been investigated to address two main issues: increase the surface area (loading capacity) of the phase and reduce the non-specific binding of proteins. The use of beads increased the surface area but also increased the back pressure within the device, while the use of DRIE silicon pillars involves a high microfabrication cost. Some new alternatives to these original methods proposed by other researchers are organic monolithic phases [12-15] which improved the extraction efficiency up to 70%. The use of porous silicon devices [16] resulted also in high DNA recovery (~80) as well as chitosan coatings [17], which reported to obtain extraction efficiencies within a range of 70% to 85%. Finally, instead a silicon substrate, Witek and co-workers explored genomic DNA purification from bacteria using photoactivated polycarbonate devices with high recovery (~85%) and DNA binding capacity (~150 ng) [18].

Microfluidic Phenol Extraction

Zahn's group conducted the preliminary phenol extraction studies using microfluidics by examining firstly the organic-aqueous interface stabilization [19]. Furthermore, experimental and computational evaluation was made by using droplet-based flows (Figure 2.4) as a proposed mixing procedure for DNA extraction [20]. Electrohydrodynamic instability (EHD) mixing [21] and diffusion limited approaches to protein and DNA partitioning [22] were also addressed. Lately, droplets-based flows were utilized to extract DNA plasmid from lysate solution and compared with standard extraction methods, achieving ~92% DNA recovery. These recent developments of the microfluidic phenol extraction, compiled in a journal paper [23], are part of this work and are discussed in detail in Chapter 3.

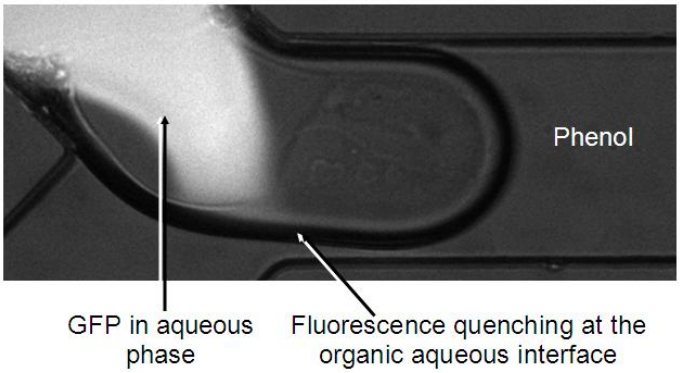

Figure 2.4: Photograph of aqueous droplet formation containing cell lysates, including green fluorescent protein GFP which partition to organic phase [20].

2.3 Theoretical background: Mechanism of Partitioning

In a two-phase system, partitioning consists of a selective distribution of solute according to their properties [24]. The solutes are affected by multiple forces including hydrogen bonding, ionic, hydrophobic, van der Waals and other weak forces with the surrounding fluid phase and interactions with other molecules which affect the transport [24]. The contribution of each force is difficult to calculate; however, the net effect can be characterized by the partition coefficient:

$$K = \frac{C_1}{C_2} \tag{2.1}$$

where C_1 and C_2 are the concentrations of the partitioned molecule at equilibrium in each phase [24]. The partition coefficient is function of the properties of the two phases, molecular characteristics, such as size and charge, and temperature, but ideally independent of concentration [24].

In a two-phase system, the distribution of the molecules is driven by two main phenomena, the thermal motion of the molecules that distributes them in each phase, and the partitioning forces, mentioned previously, which move the solute from one phase to the other. These interactions can be related as:

$$\frac{C_1}{C_2} = e^{-\Delta E / kT} \tag{2.2}$$

where ΔE is the energy required to move a molecule from phase 1 to phase 2, k is the Boltzmann constant, and T is the temperature [24].

2.4 Theoretical background: Two-Phase Microfluidic Systems

Multiphase flow is defined as two or more different immiscible fluids present in a system. Multiphase flows at microscale are complex because the flow involves multiple forces that are not significant at macroscale dimensions. However, these systems have several attractive characteristics which make them very practical for applications in microfluidics [25]. In recent years, many efforts have been done to understand multiphase fluid behavior and to find methods to control droplet-based and stratified flows, as well as several applications of these systems [25-30].

The description of fluid dynamics at small scales is quite different if it is compared to large-volume systems [31]. The Navier-Stokes equations and the continuity equation describe the fluid physics in the two bulk fluids, assuming conditions of constant density ρ and viscosity μ and incorporating the interfacial effects γ:

$$\rho\left(\frac{\partial \boldsymbol{u}}{\partial t}+\boldsymbol{u}\cdot\nabla\boldsymbol{u}\right)=-\nabla p+\mu\nabla^2\boldsymbol{u}+\boldsymbol{f} \tag{2.3}$$

$$\nabla\cdot\boldsymbol{u}=0 \tag{2.4}$$

where *u* is the velocity of the fluid, p is the pressure and *f* represents body force density.

In microscale systems, the inertial forces are much smaller compared to viscous forces and the nonlinear term in (2.1) can be then neglected, leaving the Stokes equation [25, 31]:

$$\rho\left(\frac{\partial \boldsymbol{u}}{\partial t}\right)=-\nabla p+\mu\nabla^2\boldsymbol{u}+\boldsymbol{f} \tag{2.5}$$

In this work presented here, the driving force is always pressure provided by a syringe pump but other external forces can be applied to microfluidics such as electrical, magnetic and thermal [31, 32].

In addition to the bulk fluid forces, the force equilibrium condition at the interface located between the two phases requires that

$$\iint_A (\boldsymbol{T} - \hat{\boldsymbol{T}}) \cdot \boldsymbol{n} dA + \int_C \gamma \boldsymbol{t} dl = 0 \tag{2.6}$$

where $\boldsymbol{T}$ and $\hat{\boldsymbol{T}}$ are total bulk stress in the flow above and under the surface element *A*, respectively, $\boldsymbol{n}$ is the unit vector normal to the interface, γ is the interfacial tension, and $\boldsymbol{t}$ is the unit vector tangential to the interface and normal to the boundary curve C.

Applying Stokes's theorem to (2.6) and considering an arbitrary surface element *A*, it follows that

$$(\boldsymbol{T} - \hat{\boldsymbol{T}}) \cdot \boldsymbol{n} + grad\, \gamma - \gamma \boldsymbol{n} (\nabla \cdot \boldsymbol{n}) = 0 \tag{2.7}$$

To obtain the normal stress balance, inner product is applied to (2.7) and T is replaced by $\boldsymbol{T_{ij}} = -p\boldsymbol{\delta_{ij}} + \boldsymbol{\tau_{ij}}$ where p is pressure and τ is the shear stress component $\boldsymbol{\tau_{ij}} = \mu \left(\frac{\partial \boldsymbol{u}_j}{\partial x_i} + \frac{\partial \boldsymbol{u}_i}{\partial x_j} \right)$, this gives

$$(\hat{p}_{tot} - p_{tot}) + [((\boldsymbol{\tau} - \hat{\boldsymbol{\tau}}) \cdot \boldsymbol{n}) \cdot \boldsymbol{n}] - \gamma (\nabla \cdot \boldsymbol{n}) = 0 \tag{2.8}$$

Equation 2.8 states the relationship between pressure, shear stress, interfacial tension and curvature at the intersection of the two phases. The changes of interface curvature compensate for the differences in pressure and shear stress in both bulk phases to maintain the stress equilibrium at the interface.

In fluid mechanics it is common the use of dimensionless numbers which relate the competition between different forces. In Squires and Quake's review [31], a complete list of dimensionless number used in microfluidics is shown. However, if we consider the following forces: buoyancy, gravitational, inertial, viscous and interfacial forces, the importance of each force will dramatically change as the scale goes from the macro to microscale. In microfluidics, buoyancy, gravitational and inertial forces become less important and can be neglected. On the other hand, viscous and interfacial forces, usually ignored in the macroscale, become very important to explain the fluid behavior in microchannels [25].

The Reynolds number is the most representative number to characterize flows and it is the ratio between inertial and viscous forces:

$$\mathrm{Re} = \frac{\rho U L}{\mu} \tag{2.10}$$

where U is the average flow velocity and L is the characteristic flow dimension [32]. In microscales, Re for liquid flows usually vary between the order of 10 and 10^{-4} [25]. Therefore, the inertial forces can be ignored and only laminar flow is expected. In addition, in simple channels and pressure-driven flows the velocity profiles are parabolic. More about fluids under low-Re-number conditions can be found in the literature [33, 34].

In multiphase systems, the capillary number is the most significant dimensionless number. It relates the viscous forces which act tangential to the interface elongating it and the interfacial forces which act normal to the interface minimizing the interfacial area by inducing droplet formation [19]. The capillary number can be expressed as:

$$Ca = \frac{\mu U}{\gamma} \tag{2.11}$$

If the viscous forces are more significant than the interfacial forces, the multiphase flow behavior is parallel or stratified (Ca>>1). Segmented or droplet-based flow occurs when interfacial forces are predominant (Ca<<1). Other regimes appear in the transition such as pearl-necklace and pears regimes [35, 36]. The analysis of multiphase flow behavior has been done in multiple channel configurations such as T, Y and cross junction configurations [25].

Multiphase flow pattern are influenced by multiple factors. The fluid behavior depends on interfacial forces between the fluids and channel walls, individual fluid viscosities, fluid velocities, and the geometric characteristics of the channel [35, 37-39].

First, interfacial forces can be altered using surfactants which will stabilize the interface due to the reduction of the interface tension [19]. Wall surface treatment, guide-structure microchannels and self assembled monolayer modifications are other methods to control flow behavior in microchannels [40-42].

Second, viscosity can be chosen to influence flow patterns in a desirable way. Stratified flows are more frequent with high viscosity fluids or high viscosity ratios between fluids [35, 39]. The fluid viscosity can be altered by adding components to make it more viscous such as polymers, or by changing temperature [25].

Third, the most widely used method to control multiphase flows is by tuning fluid velocity. Pumping methods used in microfluidics can easily modulate flow rate that control fluid behavior and droplets sizes [27, 28]. By increasing the flow rates, the flow pattern will become stratified due to prevalence of viscous forces [20, 35, 36, 38]. In

addition, when velocity difference increases, the shear forces to normal forces ratio increases and segmented flow turns into stratified flow [35, 37].

And finally, the flow behavior can be also influenced by channel geometry. It has been shown that channels with higher aspect ratios enhance droplet formation [37]. There is no report of the influence of the channel length. The entrance configuration is also another parameter to take into consideration to enhance one behavior or the other and to control droplet size [25, 27, 28, 43].

All these factors give the framework that designers will use to delineate multiphase microfluidic systems. The aims of many researchers are to achieve reproducibility and fully control of microscale multiphase flows to use these systems in multiple applications. Some examples of multiphase applications are: microreactions and molecular transport (enzyme kinetics, protein crystallization, syntesis of nanoparticles) [30, 41, 42, 44, 45], solvent extraction [19-21, 40], drug encapsulation and mixing [25, 27, 28].

2.5 Convective Transport Enhancements

In microfluidics, one of the major challenges is to achieve rapid and effective mixing. This is because at microscales the flow is laminar and mixing is usually diffusion limited.

The Péclet number (Pe) is defined as

$$Pe = \frac{LU}{D} \tag{2.12}$$

where L is the channel characteristic diffusion length (here assumed to be the half width of the microchannel corresponding to the diffusion length of protein from the aqueous to the phenol phase), U is the average fluid velocity and D is the protein diffusivity. When considering mixing in microfluidic channels using stratified adjacent flow streams, the Péclet number is usually very high implying long channel lengths and long diffusion times to achieve full mixing.

In the case of two-phase systems, both diffusion within the phase and diffusion across the solution interface need to be maximized. Next, two different techniques that could be easily adapted to enhance mixing in a multiphase system are discussed.

Mixing enhancement using droplets

Rapid mixing with droplets can be achieved due to the convective enhancement within droplets produced by two recirculating flows inside of each phase. Figure 2.5 shows the two flows generated in a droplet as it moves forward. As the droplet moves, the fluid interface needs to recirculate or ‘tank-tread’ and this shear is transported into the droplet causing the recirculation vortices. Two recirculating flows are also present in the continuous phase but they are not shown in the figure. These circulating flows mix the molecules within each phase and also increase the diffusion through the interface by enhancing the molecule mass transport to the fluid-fluid interface [20, 30]. In addition to convection enhancement, droplets increase molecule partitioning across interfaces due to the total interface surface area is being increased.

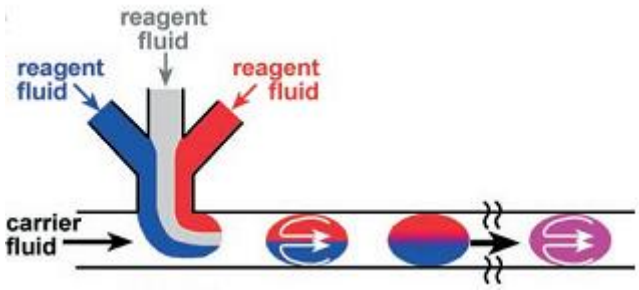

Figure 2.5: Illustration of multiple reagent mixing in a droplet by recirculating flows [30].

Chaotic Advection

Chaotic advection mixers are three-dimensional structures that mix the flow by reorienting the flow alternatively which produce the stretching and folding of the fluid stream. Three-dimensional serpentine microchannels (two-layers device) have been developed with significantly mixing improvements [46]. In addition, Stroock et al designed a chaotic mixer by using asymmetric herringbone-like grooves that produce a three-dimensional twisting flow [47].

In the case of a two-phase system, the plugs already have inside a two-dimensional flow due to the internal recirculation. Mixing can be easily enhanced by using serpentine-liked structures (three dimensional twist) without the requirement of two-layer fabrication. In each direction change, the mixing inside of each phase is enhanced due to the stretching and folding of the droplets [30, 48, 49].

Both stratified and droplet-based flows benefit by this passive mixing. In Figure 2.6, droplet enhancement and chaotic advection mixing strategies are combined showing how

recirculating flows are reoriented from the direction of the droplet movement, streached and fold, resulting in a more efficient mixing.

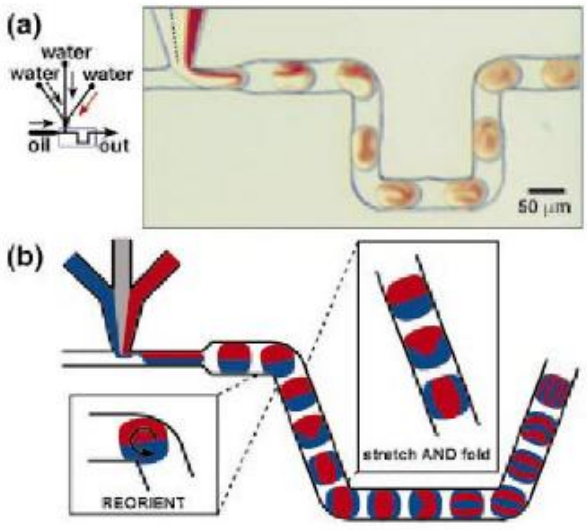

Figure 2.6: Droplets moving through a winding microchannel, (a) experimental results and (b) schematic of the droplet folding [50].

This review of the theoretical aspects of multiphase microfluidic system provides the central guidelines for the design of the DNA purification module addressed in the following chapter.

Chapter 3

Microfluidic DNA purification via phenol extraction

In this chapter, microfluidic platforms are described and tested using organic solvents to investigate the protein partitioning while DNA can be extracted from an aqueous phase. Device design, fabrication and materials used for the extraction are presented followed by the results obtained for bacterial lysates using microfluidic platforms, standard macro-scale method for phenol extraction and a commercial DNA purification kit.

3.1 Device Design

During phenol extraction, the cell components distribute into either the aqueous phase or the organic phase to reduce interaction energies with component partitioning occurring at the organic-aqueous interface. Therefore, maximizing the interfacial interaction area is critical to effectively partition the different cellular components. In macroscopic systems this is accomplished through mixing using a vortex mixer to create chaotic and vortical flow fields interspersing the two fluid phases. Within microfluidic systems, these types of flow profiles cannot be easily generated so mixing and partitioning must rely on diffusive mass transport or droplet interspersion of the phases as described in previous chapter.

When the two phases are infused as a stratified flow the flow rate must be large enough so that a stable stratified flow can be maintained, while the residence time of the fluid within the microchannel must be long enough for complete diffusive mixing. As has been long recognized in the microfluidics field, when the two fluid streams flow at a high linear velocity (~mm/s or greater) minimal diffusive mixing between the streams is expected. In order to design the microchannel three parameters were considered: the Péclet number, capillary number and diffusion time required.

The Péclet number $Pe = \frac{LU}{D}$ relates the convective transport of the material flowing down the length of the channel (LU) to the transverse diffusion of proteins (D) across the channel width from the aqueous phase to the organic-aqueous interface. In microfluidic platforms the Pe is usually very high (~100 or greater); while the length of channel required to ensure full diffusive mixing varies linearly with Pe, implying a long microchannel is required.

The operating flow velocity, U, used in this study is constrained by the interfacial forces. In microfluidic multiphase systems, the flow patterns are determined by a variety of factors such as fluid choice, flow velocity, viscosity ratio, interfacial tension, device wettability and geometry of the channels, as addressed in Chapter 2.

One of the most important factors in determining multiphase flow structure has relied on the capillary number $Ca = \frac{\mu_c U_c}{\gamma}$, which relates the relative importance of viscous shear forces on the continuous fluid phase ($\mu_c U_c$) which act tangentially to the interface, elongating it with the interfacial forces (γ), which act normal to the interface, minimizing the interfacial area by inducing droplet formation [19]. As the viscous forces become

more significant than the interfacial forces, the multiphase flow behavior is parallel or stratified (*Ca*~1 or greater). Segmented or droplet-based flow occurs when the interfacial forces are dominant (*Ca*<<1).

The preliminary microfluidic device design was made considering a stratified flow condition assuming *Ca* is equal to 1 which constrains the fluid velocity. The diffusion time required for the protein to reach the organic-aqueous interface was estimated as:

$$t_D = \frac{w^2}{4D} \tag{3.1}$$

where *w* is the half width of the microchannel and *D* is the diffusion coefficient of the molecules to be extracted. The diffusion time was calculated assuming *w* equal to 30, 40 and 50 μm and a BSA diffusivity in water equal to 5.9×10^{-11} m^2/s [51]. By setting the required diffusion time equal to the fluid residence time inside of the device, the microchannel length was calculated using the fluid velocity fixed by the capillary number condition where the required channel length, $L_{channel}$ is equal to $U * t_D = U * w^2/4D = Pe * w/4$. The channel lengths were 41.8, 57 and 64.8 cm, for the corresponding half width of 30, 40 and 50 μm, respectively.

Based on these assumptions for passive diffusion across a stratified flow, long serpentine devices were first fabricated to investigate protein partitioning into an organic phase using both a stratified flow and droplet-based flow. A second device was also fabricated after the results using the long serpentine and the design modifications were addressed in the next section.

3.2 Device fabrication

All microchannels designed were fabricated using the soft lithography approach as described in the literature [52]. The microchannel designs were patterned onto a silicon master using standard photolithography techniques followed by casting of polydimethylsiloxane (PDMS) and bonding to glass. A schematic of the photolithography and soft lithography techniques is shown in Figure 3.1 where each step of the fabrication is presented. A detailed protocol for the device fabrication is provided in Appendix A.

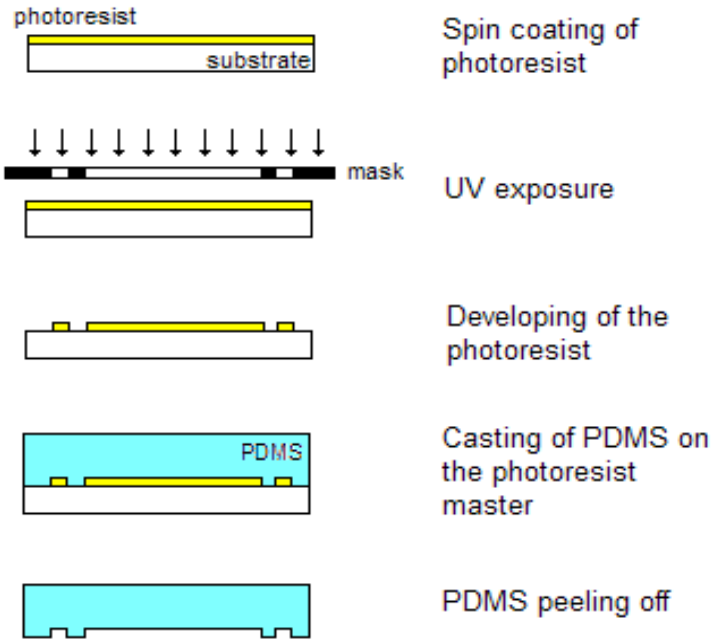

Figure 3.1: Fabrication steps of photolithography and soft lithography techniques.

The master mold was lithographically patterned on a spin coated SU-8 negative photoresist (MicroChem, Newton, MA). The PDMS structure was cast by mixing the elastomer base and curing agent (Sylgard 184 Silicone Elastomer Kit, Dow Corning, Midland, MI) at a ratio of 10:1 and poured on top of the master mold. After degassing in

a vacuum chamber, the PDMS cast was cured in an oven at 65˚C for 1 hour. The PDMS structure was then irreversibly bonded to a glass slide following surface activation of the PDMS and glass using a corona discharge generator [53].

The device was connected with 0.254 mm ID Tygon tubes (Small Parts Inc., Miami Lakes, FL) and sealed with glue (J-B KWIK, Sulphur Springs, TX), specially selected due to their compatibility with the organic phase. The serpentine devices consisted of a long microchannel where the two phases were co-infused into a converging channel geometry with channel width and length described previous section and height of 20 μm (Figure 3.2).

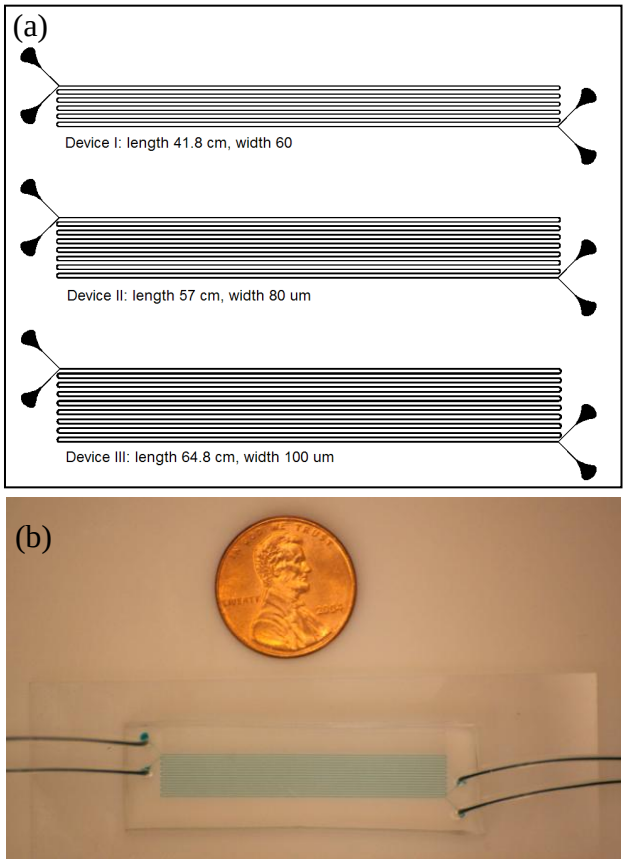

Figure 3.2: (a) Serpentine mask designs and (b) photograph of the microfluidic chip.

In experiments using droplet-based flows, the channel height was increased to 40 μm to promote droplet formation. A second design was developed to be used with bacterial lysates and under only droplet-based flows. Due to the mass transfer enhancement enabled by droplet flows, the total length of the device could be reduced to 10 cm, while the channel width and height were 100 and 40 μm, respectively, and the entrance configuration of the microchannel was changed from a Y-type to T-type inlet to facilitate the droplet formation.

3.3 Materials and Experiment setup

Aqueous phase preparation

The aqueous phase consisted of phosphate buffered saline (PBS) (150 mM NaCl, 8.4 mM $Na_2HPO_4 \cdot 7H_2O$ 1.8 mM $NaH_2PO_4 \cdot H_2O$ pH 7.5) (HyClone, Thermo Scientific, Logan, UT) with DNA and protein analytes introduced to investigate protein partitioning and DNA extraction. The analytes were bovine serum albumin protein (BSA) (Omnipur, fraction V; EMD Biosciences) conjugated with rhodamine fluorescent dye and unlabeled 2-log DNA ladder (0.1 to 10.0 kb; New England Biolabs, Beverly, MA).

The conjugation of BSA to 5-6-carboxy-tetramethylrhodamine (TAMRA) succinimidyl ester dye (Fluka, Switzerland) was made at a 10:1 molar ratio of dye to protein, and the complete protocol can be found in Appendix B. The labeled protein solution was then filtered through a PD-10 desalting column (Sephadex G-25M; GE Healthcare) to remove the unconjugated dye from the solution. The output fraction with the labeled proteins was collected, stored at -20°C and diluted in PBS prior to use.

Bacterial lysates preparation

E. coli HB101 K-12 (Bio-Rad, Hercules, CA) was transformed using a Bio-Rad Transformation kit to insert a green fluorescent protein coding pGLO (5.371 kb) plasmid. The bacteria colony was cultured at 37 °C for 14 hours in Luria-Bertani liquid medium with 100 μg/μl ampicillin and 2% arabinose (Teknova Inc., Hollister, CA). Following culturing, the bacterial cells were pelleted in 1.5 ml Eppendorf tubes by centrifugation at 10000 rpm at 4°C for 15 min. The bacterial lysates were prepared using Qiagen plasmid purification buffers (Qiagen, Valencia, CA) as indicated in the Qiagen Plasmid Purification Handbook [7]. See Appendix B for bacteria transformation, plate and liquid culture protocols.

Bacterial pellets were resuspended in 300 μl Qiagen buffer P1 (50 mM Tris-Cl, pH 8.0; 10 mM EDTA; 100 μg/ml RNase A) and an equal volume of lysis buffer P2 (200 mM NaOH, 1% sodium dodecyl sulfate (SDS) (w/v)) was added and incubated for 5 minutes. Finally, 100 μl of neutralization buffer P3 (3.0 M potassium acetate, pH 5.5) at 4°C was added and incubated for 5 minutes on ice to precipitate large debris and SDS. After centrifugation at 10000 rpm for 10 minutes, the supernatant was removed and used in three tested experimental conditions; the microfluidic DNA extraction as well as in a standard phenol extraction and Qiagen plasmid purification kit for extraction comparison purposes.

Experimental procedure

The infusion of the aqueous and organic phases, contained in glass syringes (Hamilton, Reno, NV), was made by using syringe pumps (PicoPlus 22, Harvard apparatus, Holliston, MA) to control the infusion flow rates. The aqueous phase consisted of a PBS buffer solution with the addition of 0.5% (w/v) SDS (J. T. Baker Chemical Co., Phillipsburg, NJ), in order to reduce the interfacial tension between the aqueous and phenol phases and achieve a stable stratified interface between the phases [19].

The BSA protein concentration was diluted to 0.3 μg/μl in PBS, which had sufficient fluorescence intensity for flow visualization while preventing precipitation of protein within the microchannel. Protein precipitation was seen using BSA concentrations of 0.5 μg/μl or higher, causing obstruction of the flow within the microchannels. The final DNA ladder concentration was diluted to 0.075 μg/μl.

The phenol phase was a mixture of three organic components: phenol, chloroform, and isoamyl alcohol, at 50, 48 and 2% by volume concentration, respectively purchased from Pierce (Rockford, IL) and used as received. The organic phase viscosity was previously determined to be 3.52×10^{-3} Pa-s and the interfacial tension with the aqueous phase was 0.1 mN/m [19].

To analyze the fluorescence intensity of rhodamine in the channel, a Nikon Eclipse TE2000U inverted microscope (Nikon, Tokyo, Japan) operating in epifluorescence mode, a TRITC filter cube and charged coupled device (CCD) camera (PowerView 1.4 MP, TSI Incorporated, Shoreview, MN) were used to acquire images. All the images were acquired using a 10× objective, neutral density filter ND1 for the epifluorescence arc

lamp and a 26 ms exposure time. The average intensity of the fluorescently labeled BSA in the aqueous phase at the entrance and at the outlet of the device were calculated using ImageJ software, following subtraction of the average image intensity from each image background, and compared to evaluate the protein depletion.

Additionally, spectrophotometric analysis was used for protein partitioning quantification (Appendix B). Aliquots from the aqueous phase at the inlet and from the aqueous phase collected at the outlet were measured using a 1 ml cuvette and a DU 730 spectrophotometer (Beckman Coulter, Fullerton, CA), at a dilution factor of 6. The protein depletion was evaluated comparing rhodamine absorption at 555 nm of the aqueous inlet and the aqueous outlet aliquots.

Finally, DNA extraction was quantified by gel electrophoresis analysis using 1% agarose gel in 1× Tris-acetate-EDTA (TAE) buffer (see Appendix B for gel electrophoresis protocol). Images of gel were taken by BioDoc-it Imaging System (UVP, Upland, CA) and ImageJ was used to quantify extraction efficiencies comparing total intensity of the DNA fragments of the inlet and outlet solutions. For all data presented here a set of four experiments were used for statistical analysis.

3.4 Results and Discussion

Review of serpentine device comparison

As part of previous work (Master of Science Thesis), the serpentine designs were compared based on their BSA depletion efficiency. The first experiments were realized using the largest device (device III in Figure 3.2a, 100 μm wide and 64.8 cm long). For

this particular geometry, the parallel flow pattern was achieved in the entire serpentine structure only at high flow rates (3 µl/min for the aqueous phase and 1.3 µl/min for the phenol phase).

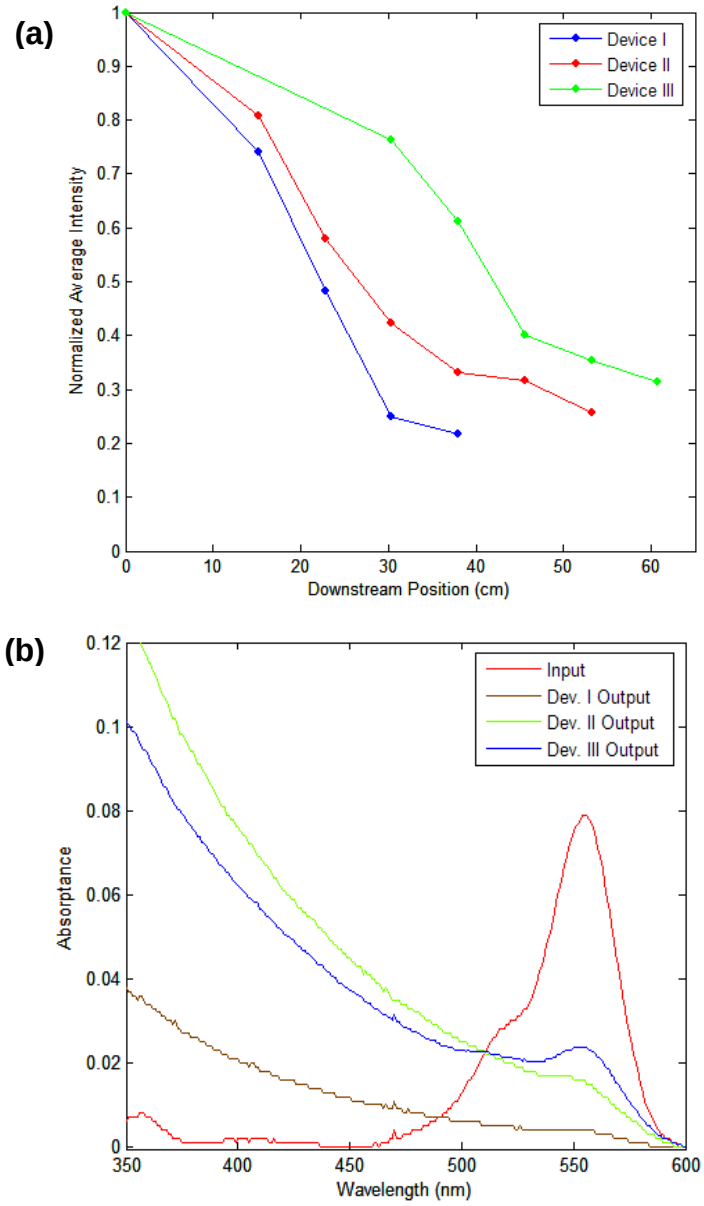

Figure 3.3: Comparison of the serpentine device design based on the protein depletion. (a) using epi-fluorescent image analysis and (b) absorption spectra analysis.

The resulting mean velocity of the aqueous phase was 5 cm/s. When the velocity was lowered, the spontaneous generation of droplets at the entrance or in other sections of the device was observed.

The comparison of protein extraction efficiency between the three different devices was conducted at the same mean velocity (5 cm/s) in the aqueous phases for each of them. The aqueous flow rates were 2.4 μl/min and 1.8 μl/min for device II and I, respectively, with flow rates for the phenol phase of 1 μl/min and 1.3 μl/min in the same devices to achieve a stratified flow profile.

Images of the phases were taken at different positions along each device and analyzed, obtaining the average intensity of the aqueous phase at those positions and normalized to the average intensity at the inlet. The BSA depletion comparison in each device is shown in Figure 3.3a as a function of downstream position. As expected, the protein depletion in the aqueous phase is faster in the narrow channel device (device I) than in wider ones (device II and III). The partitioning efficiencies using the fluorescence intensity method were 78%, 74.3% and 68.5% for device I, II and III, respectively.

The aqueous phase outputs from the three devices were collected and quantified by spectrophotometry. From the spectra of the inlet and the outlet solutions in Figure 3.3b, the high absorption at low wavelength was found in all the aqueous outputs after leaving the device which is due to phenol contamination forming small micelles at the interface. Using the absorption ratio at 555 nm between the inlet sample and the outputs solutions from the three devices, the partitioning efficiencies were 90%, 78% and 69% for device I, II and III, respectively.

Since the diffusion time is proportional to the square of the diffusion path from one phase to the other (half width of the channel), as the microchannel width decreases the required diffusion time decreases as well. From the device comparison presented above, device I appears to be the most efficient at partitioning protein due to the small channel width; however, reduced channel width can lead to other problems like high operating pressures or channel obstruction by the accumulation of protein precipitates or cell debris. For the following experiments, device II was chosen for flow comparison tests to avoid clogging due to narrow inlets as in device I.

Review of flow pattern comparison

Once the device selection was made, two flow conditions, stratified or parallel flow and droplet-based flow, were tested to investigate the protein partitioning into the organic phase.

To produce a stable stratified flow profile with each fluid phase being half the channel width, a flow rate of 2 μl/min for the aqueous phase and 0.6 μl/min for the phenol phase were utilized resulting in a capillary number *Ca* of 0.72.

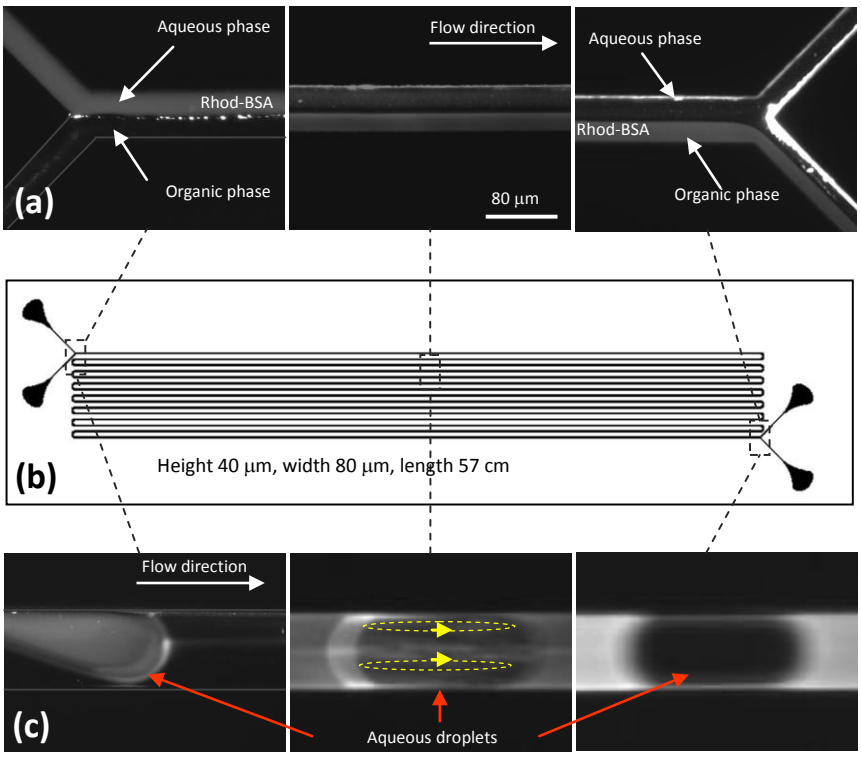

Figure 3.4: Serpentine device: (a) images of BSA partition into organic phase using stratified flow, (b) the device geometry and dimensions, and (c) images of BSA partition using droplet-based flow.

Using the CCD camera, images at different positions along the length of the device, shown in Figure 3.4a, were taken to quantify the fluorescently labeled BSA in each phase and evaluate the partitioning from one fluid phase into the other. According to epifluorescence microscopy analysis and using a set of four experiments, 78 ±11.57% of the rhodamine labeled BSA protein was removed from the aqueous phase through the device length by passive diffusion.

During these experiments, the multiphase outputs were collected and analyzed by spectrophotometry to evaluate the total partitioning, resulting in 78.4 ±15.2% depletion

according this method. Absorption spectra of the inlet and outlet solution are shown in Figure 3.5a.

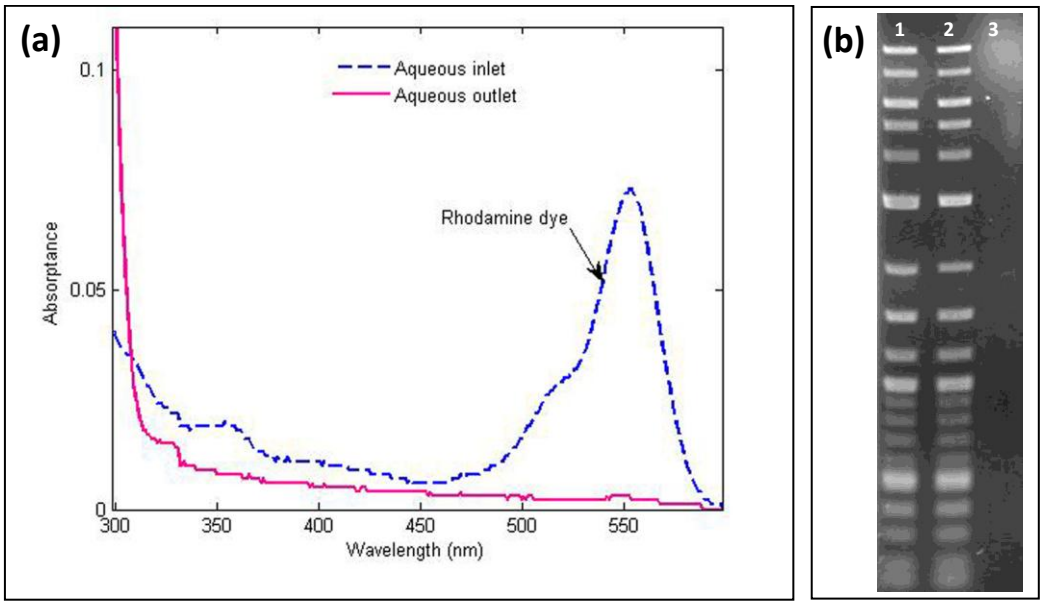

Figure 3.5: Analysis of inlet and outlet aliquots for stratified flow using (a) dye absorption spectra and (b) DNA gel electrophoresis (1: inlet, 2: aqueous outlet, 3: organic outlet).

On the other hand, the high DNA recovery in the aqueous outlet was found using gel electrophoretic analysis and the recovery using this type of flow resulted in 89.3 ±7.5% (Figure 3.5b).

However, working with multiphase systems in microchannels allows the formation of droplets which could have several advantages for DNA purification. First, the use of droplets increases the interfacial area between the phases so proteins can quickly partition into the phenol phase. Second, rapid mixing within the droplets can be achieved due to the convective enhancement produced by two recirculating flows seen inside of each

droplet, which mixes the analytes within the aqueous phase which in turn improves the transport to the organic-aqueous interface [20, 54, 55].

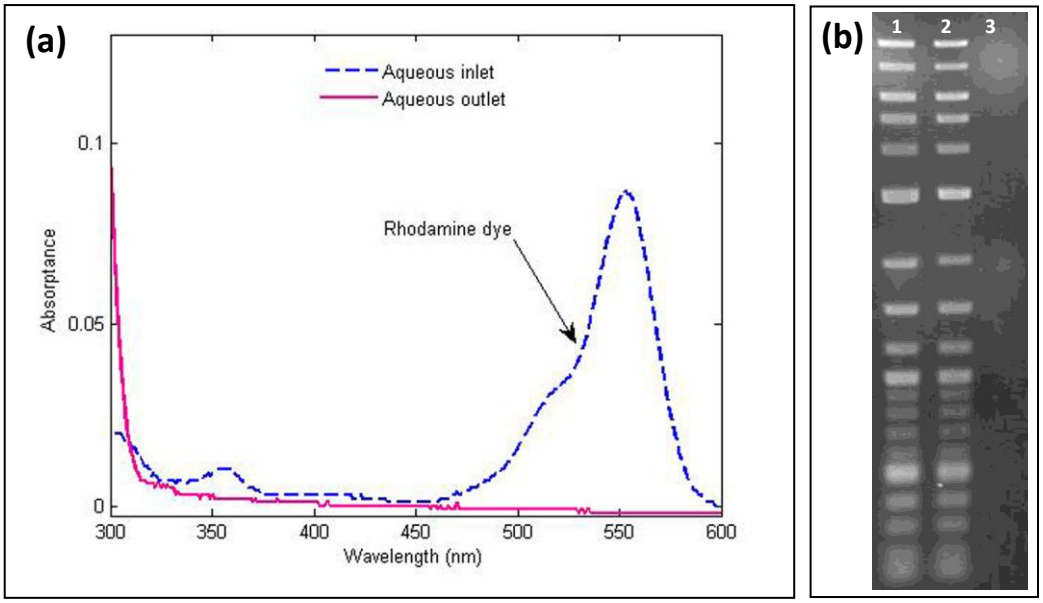

Figure 3.6: Analysis of inlet and outlet aliquots for droplet-based flow using (a) dye absorption spectra and (b) DNA gel electrophoresis (1: inlet, 2: aqueous outlet, 3: organic outlet).

Droplet formation was investigated using the same serpentine platform and BSA-DNA mixture used to study partitioning and extraction under stratified flow. In this case, the flow rates used were 0.4 μl/min for the aqueous phase and 0.5 μl/min for the phenol phase at a Ca of 0.07. Fluorescence images at the entrance and at the outlet of the device are shown in Figure 3.4c. It can be seen from these images that the protein partitioning was greatly improved by the convective transport enhancement from the droplet based flow compared to the experiments using stratified flow conditions. The protein partitioning by fluorescence microscopy analysis was 91.6 ±5.1% and confirmed via spectrophotometry analysis with a depletion efficiency of 96.27 ±1.73% (Figure 3.6a).

The DNA recovery using droplet-based flow was calculated by gel electrophoresis analysis (Figure 3.6b) as in the previous stratified flow experiments and the percentage recovered was 97.4 ±1.32%.

Plasmid DNA Purification from Bacterial Lysates

Based on the information collected during the droplet-based experiments, the serpentine device, originally designed to perform extraction using stratified flows, was replaced by a shorter device (Figure 3.7) which was redesigned for segmented (droplet) flow. In the previous experiment, droplets were shown to enhance mixing, removing the BSA from the aqueous droplets to produce clear plugs, at a downstream distance of approximately 10 cm from the entrance of the device.

This finding allowed a dramatic reduction in the length of the device; and consequently a residence time reduction. In addition to the channel length shortening, the device entrance was modified to a T-type junction to promote the droplet formation. T-type channels have been used by other researchers to investigate droplet formation [35-39], and it allows for the generation of stable droplets more easily than the Y-type entrance due to the crosschannel blocking and pinch-off mechanisms of droplet formation observed by other research groups [36, 37].

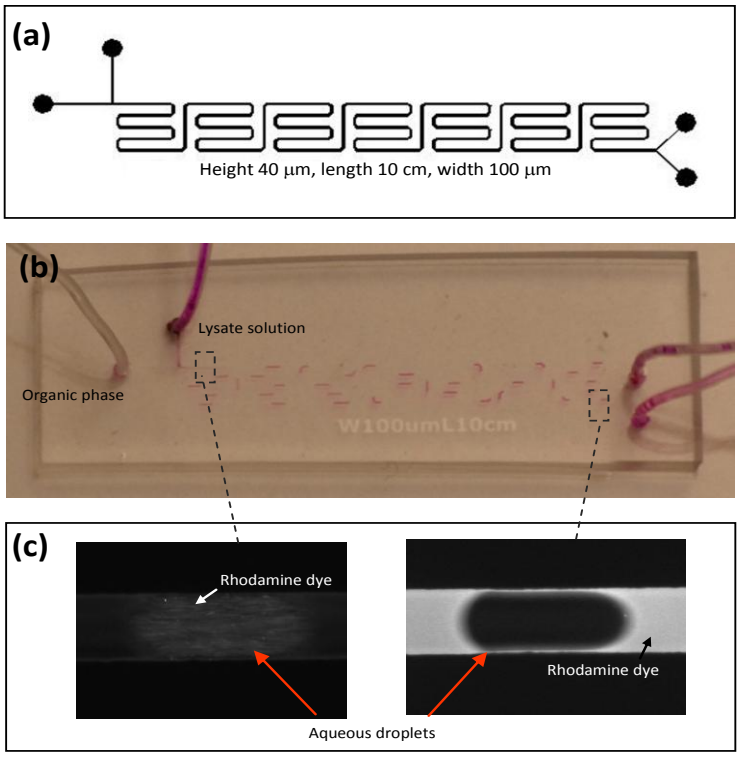

Figure 3.7: (a) Redesigned device geometry and diamensions, (b) photograph of the new shorter device and (c) images of rhodamine-labeled BSA partitioning from aqueous phase into organic phase.

Having demonstrated the device's capability to extract DNA from a protein solution, the next step was to perform plasmid DNA extraction from a bacterial culture and compare the purification efficacy with other traditional methods. The shorter redesigned device was utilized in this case, using bacteria lysates from transformed E. coli containing a green fluorescent protein coding pGLO (5.371 kb) plasmid.

The lysates solutions were prepared from a bacterial culture using Qiagen buffers for lysis, as described in previous section. Next, the solutions were used in the microfluidic device, Qiagen extraction column and standard macro-scale phenol extraction to compare their extraction efficiencies.

The lysates were then infused conjunctly with the phenol phase into the microfluidic device demonstrating successful recovery of plasmid in the aqueous phase, based on the gel electrophoresis results presented in Figure 3.8a.

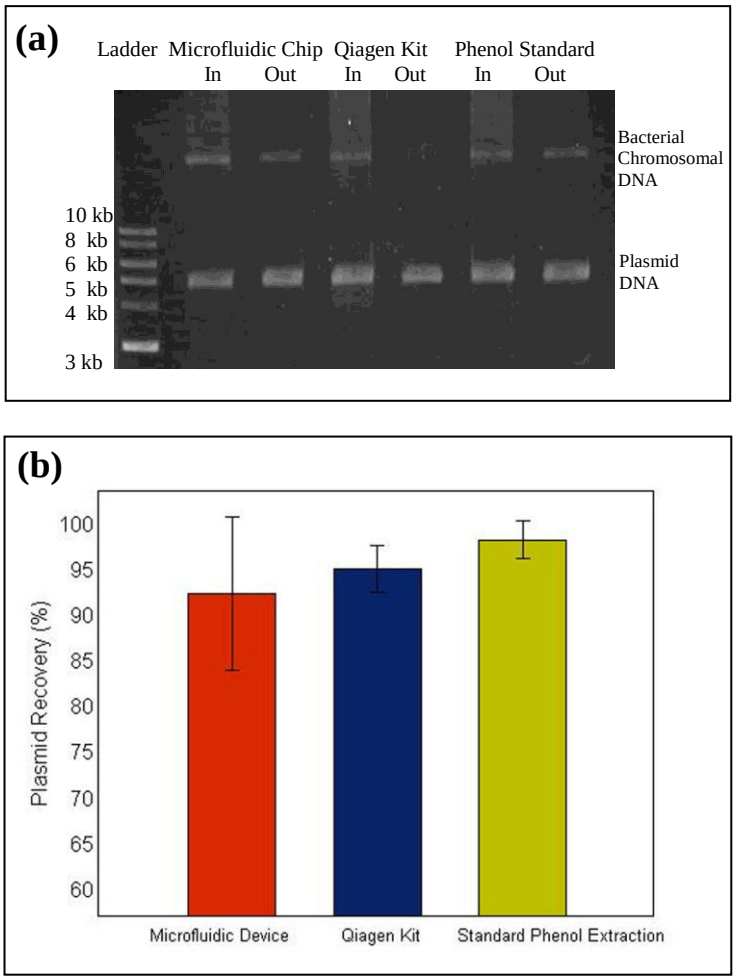

Figure 3.8: Comparison using the redesigned microfluidic device, Qiagen kit and standard macroscale phenol extraction: (a) gel electrophoresis analysis and (b) total plasmid recovery from bacterial lysates at the aqueous outlet.

The supercoiled plasmid form was clearly identified on the gel and seems to migrate through the gel close to the velocity of a 5 kb linear fragment. Because the plasmid is circular it will migrate through the gel at a rate which can be different from a linear DNA

fragment. Intact circular (supercoiled) plasmids will migrate through the gel faster than their linear counterparts.

Based on band intensity, the pGLO concentration was estimated at 0.56 ng/μl. Bacterial chromosomal DNA was also found in the recovered solutions in the case of microfluidic extraction and standard phenol extraction. In addition to this, a higher background intensity can be seen in all of the sample inlet lanes on the gel for each of the three purification methods. The recovered sample lanes have much lower background intensity indicative of the successful removal of contaminants from the lysates using all three extraction methods.

The efficacy of the plasmid extraction was compared with those obtained with a commercial DNA kit (Qiagen) and standard phenol extraction. Using the same volume of bacterial lysates, the plasmid recoveries using the microfluidic device, a Qiagen SPE extraction kit and traditional phenol extraction, were 92.4 ± 8.4%, 95.1 ±2.5%, 98.3 ± 2.08%, respectively (Figure 3.8b). Therefore, the microfluidic phenol extraction shows high recovery of DNA which is similar to efficiencies obtained with traditional extraction methods.

In addition, the DNA extraction efficiencies found via microfluidic phenol extraction are also comparable to the other microfluidic approaches using solid-phase extraction. Wen et al work provides a comparison table of the solid-phase extraction device where the DNA extraction efficiencies found to vary from 30% to 85% depending of the phase material and the sample [56]. In comparison, the method proposed here would recover a larger mass of DNA due to the lack of attachment and detachment steps present in the solid-phase methods.

On the other hand, the protein quantification was not possible to achieve with the microfluidic phenol extraction due to the phenol contamination found in the aqueous phase. The phenol trace has a very high light absorption which impedes the DNA purity analysis by absorbance ratios of 260nm/230nm and 260nm/280nm for organic contaminants and protein content, respectively. Additionally, the bicinchoninic acid (BCA) protein assay was also affected by the organic contamination.

The presence of a phenol trace in the aqueous phase is the main challenge of this work in order to make this device suitable for integration with downstream processes required for DNA manipulation as restriction cutting and PCR. In Chapter 6, some approaches to address this issue are discussed.

Summarizing the first part of this work, microfluidic platforms were designed to perform miniaturized liquid-phase extraction and to evaluate DNA purification and protein partitioning efficiencies as well as plasmid extraction from bacterial lysates. Dual inlet-dual output serpentine devices were utilized as prototype for the initial studies of protein partitioning using stratified flow and droplet-based flow. Experiments infusing fluorescently labeled proteins and DNA demonstrated the ability of the device to partition proteins from the aqueous phase into the phenol phase and allowed a high percentage DNA recovery in the aqueous phase with minimal DNA loss into the organic phase. A redesigned device was fabricated to conduct DNA extraction from bacterial cell lysates using only droplet-based flow, due to the mass transfer enhancement enabled by this flow. Finally, plasmid extraction from transformed bacteria was conducted using this microfluidic platform with DNA recoveries comparable to the recovery obtained by standard macroscale extraction methods.

In Chapters 4 and 5 the electrokinetic manipulation of DNA is addressed as potential continuation after the purification module presented here, as a pre-conditioning step prior to other downstream analysis processes. Conclusions of this purification module and the future work needed after this experimentation are discussed in Chapter 6.

Chapter 4

Background of Electrokinetic Sample Concentration

Most surfaces in contact with an electrolyte solution acquire a net charge due to various charging mechanisms. As a result, these charged surfaces attract opposite-charge ions (counterions) in the solution while repelling equal-charge ions (co-ions) leading to the formation of an electric double layer (EDL) at the surface [57]. The thickness of this double layer is commonly referred to as the Debye length λ_D. Electrokinetic phenomena is a term applied to four distinct phenomena (electroosmosis, electrophoresis, streaming potential, and sedimentation potential) that arise when the mobile region of the EDL and an external electric field interact with a viscous shear layer near the charged surfaces [58].

In this work, two of these phenomena, electroosmosis and electrophoresis, are considered within a confined geometry by the application of a transverse electric field across the width of a microchannel. A theoretical description of these phenomena is provided next with the inclusion of the dielectrophoresis definition which will be later on required in the discussion of the experimental results of a sample pre-conditioning module in Chapter 5. In addition to the theoretical background, an up-to-date review of on-chip sample pre-concentration methods is included here.

4.1 Electroosmosis

An electroosmotic flow is created by a net migration of ions of the EDL at a solid charged surface due to the application of an external electric field as can be observed in the right side of Figure 4.1. This ionic movement is transmitted to the bulk fluid due to viscous forces causing a net fluid flow (slip velocity) relative to the stationary surface [57, 58].

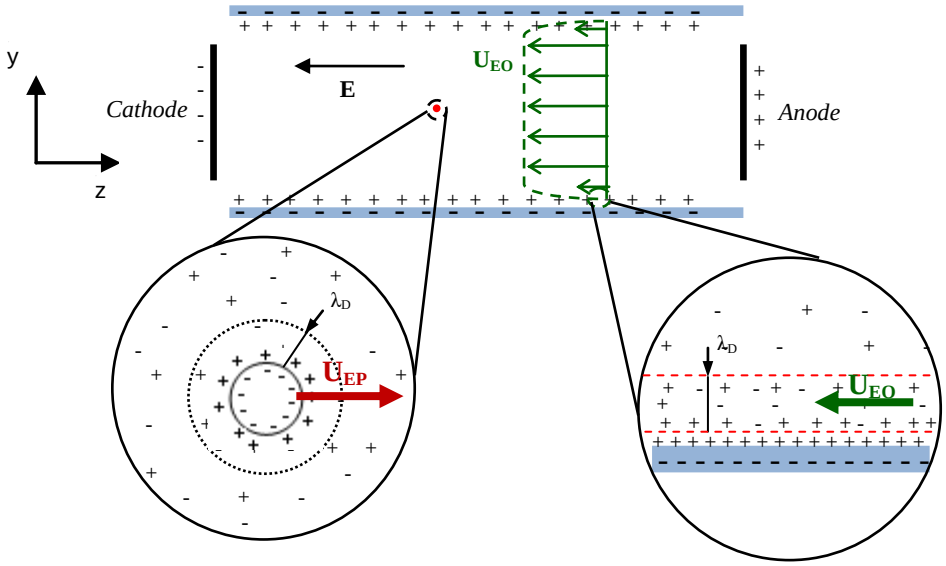

Figure 4.1: Schematic of the EP particle motion and the EO flow in an open channel.

In order to obtain the electroosmotic velocity, the equations of conservation of momentum (Navier-Stokes equations) need to be solved incorporating the electric body force per unit volume given by $\boldsymbol{f}_E = \rho_E \boldsymbol{E}$, where ρ_E is the charge density. Eq. 2.3 can be rewritten as follows:

$$\rho\left(\frac{\partial \boldsymbol{u}}{\partial t}+\boldsymbol{u}\cdot\nabla\boldsymbol{u}\right)=-\nabla p+\mu\nabla^2\boldsymbol{u}+\rho_E\boldsymbol{E} \tag{4.1}$$

If the flow is considered to be an inertia free capillary flow with no pressure gradient, then Eq. 4.1 reduces to:

$$\mu\nabla^2\boldsymbol{u} = -\rho_E\boldsymbol{E} \tag{4.2}$$

On the other hand, if we also consider Poisson's equation that relates the spatial distribution of the electric field ($E=-\nabla\phi$) to the charge distribution:

$$\nabla^2\phi=-\frac{\rho_E}{\varepsilon} \tag{4.3}$$

where ε is the permittivity of the solution and then plugging Eq. 4.3 in 4.2 we obtain:

$$\mu\nabla^2\boldsymbol{u} = \varepsilon\nabla^2\phi\boldsymbol{E} \tag{4.4}$$

Considering the reference system showed in Figure 4.1, the electric field has only component in the z direction; therefore the flow velocity resulting is in that direction, u_z. In addition, the potential and u_z are only function of y and their derivatives with respect z are zero. Now, Eq. 4.4 can be reduced to the one-dimensional form as follows:

$$\mu\frac{\partial^2 u_z}{\partial y^2} = \varepsilon\frac{\partial^2\phi}{\partial y^2}E_x \tag{4.5}$$

Integrating Eq. 4.5 gives

$$\mu\frac{\partial u_z}{\partial y} = \varepsilon\frac{\partial\phi}{\partial y}E_z \tag{4.6}$$

by setting at the bulk of the fluid ($y\rightarrow\infty$) $\partial u_z/\partial y$ and $\partial\phi/\partial y$ equal to zero. Integrating again and setting at the hydrodynamic slip plane (y=0) u_z=0 and $\phi=\zeta_w$. This then gives

$$U_{EO}=-\frac{\varepsilon\zeta_w}{\mu}E_z \tag{4.7}$$

This is the electroosmotic velocity developed by the bulk flow and it is called the Smoluchowski slip velocity equation [58]. The electroosmotic (EO) mobility is then defined as

$$\mu_{EO} = -\frac{\varepsilon \zeta_w}{\mu} \tag{4.8}$$

Summarizing, when applied axially along a channel and under constant longitudinal electric field, the electroosmotic velocity developed by the bulk flow is proportional to the electric field and it is equal to the Smoluchowski slip velocity.

The zeta potential of the wall determines the magnitude of the EO flow. The wall zeta potential is affected by ionic strength, counterion type and pH of the solution [59-63], but is also dependant on the surface properties of the wall. The effect of channel material and/or surface modifications to the development of the EDL has been widely investigated to enhance or suppress EO flow [64-67].

Nevertheless, the most important use of the EO flow is to drive bulk fluids in microchannels and it provides the advantage over other methods that the electrodes can be embedded within the chip allowing compact microchips and precise fluid control [32, 68].

4.2 Electrophoresis

Electrophoresis is defined as the motion of a charged particle through an electrolyte solution under an applied external electric field [58]. The electrophoretic force induced by the external field is given by

$$F_{EP} = qE \tag{4.9}$$

where q is the net charge between the charge particle and the concentric Debye length (λ_D) as depicted in Figure 4.1 (left side). Considering a large Debye length, where λ_D is larger compared with the analyte radius a and balancing the electrical force with the Stokes drag force, it gives:

$$qE = 6\pi\mu U_{EP} a \tag{4.10}$$

From the definition of surface charge, the potential can be written as [58]:

$$\zeta_P = \frac{q}{4\pi\varepsilon(a+\lambda_D)} \tag{4.11}$$

where ζ_p is the zeta potential of the particle in that solution. Now the particle velocity with a large Debye length results in:

$$U_{EP} = \frac{2}{3}\frac{\zeta_P \varepsilon(1+a/\lambda_D)E}{\mu} \approx \frac{2}{3}\frac{\zeta_P \varepsilon E}{\mu} \tag{4.12}$$

However, the migration velocity due to the electrophoretic effect for a thin diffuse EDL at the particle surface can be reduced to the Helmholtz-Smoluchowski equation [58]:

$$U_{EP} = \frac{\varepsilon\zeta_P}{\mu}E \tag{4.13}$$

The electrophoretic (EP) mobility is similarly defined as

$$\mu_{EP} = \frac{\varepsilon\zeta_P}{\mu} \tag{4.14}$$

It should be noted that the EP mobility for thin EDL is not dependent of the shape and size of the particle. The size effect is implicitly contained in the zeta potential. The zeta

potential of the particle, directly affecting the particle mobility, is a function of the net charge resulting of the charged particle exposed to the electrolyte solution. However, larger DNA fragments are free draining so the free solution mobility has been found to be independent of the molecule size, and size fractionation can only be produced by physical interaction of DNA within a confining geometry like capillaries, sieving gels or nanostructures where fragment motion is retarded based on their size [69]. Stellwagen *et. al.* measured DNA free solution mobility for various sized DNA fragments in the most commonly used electrophoretic buffers, demonstrating size independence on DNA free solution mobility for fragments lengths greater than 400 bp [67].

It has also been shown that the DNA EP mobility decreases with increasing buffer ionic strength and conductivity due to the compression of the EDL and the reduction of the zeta potential. Lastly, counterion type can affect DNA mobility, where the DNA mobility is significantly reduced in the presence of high NaCl concentration buffers, such as phosphate-buffered saline (PBS), due to electrostatic shielding of surface charges on DNA phosphodiester backbone [70, 71].

4.3 Combined electrophoresis and electroosmosis in confining geometries

As a result of EP and EO phenomena, charged analytes will move at a velocity that depends on both the EP mobility of the analyte and any induced EO flow. The net velocity of a particle is therefore a superposition of the EP velocity and EO velocity due

to drag on the particle from the EO flow. In a unidirectional linear flow field the net velocity of a charged particle is

$$U_P = U_{EP} + U_{EO} = (\mu_{EP} + \mu_{EO})E \tag{4.15}$$

Thus, the velocity of a DNA or protein molecule will be not only affected by its net charge but also by the flow convection due to the EO flow as shown in Figure 4.2.

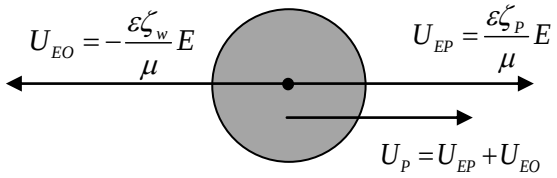

Figure 4.2: Net particle velocity *Up* as a result of the EP force and the EO flow drag force.

If the driving electric field is applied across the width of a microchannel, the electroosmotic velocity at the top and bottom of the channel is predicted by Eqn. 4.7. However, since the channel has bounding walls the flow must recirculate in order to conserve fluid mass similar to the classic lid driven (Couette) cavity flow problem.

In this situation, the top and bottom walls move at the slip velocity (U_{EO}) depending on their wall zeta potentials. This original movement imposes a constant pressure gradient for the conservation of mass which leads to the one-dimensional Navier-Stokes equation:

$$\frac{\partial^2 u_z}{\partial y^2} = -\frac{1}{\mu}\frac{\partial P}{\partial z} = 2a \tag{4.16}$$

Integrating Eq. 4.16 twice gives:

$$u_z = ay^2 + by + c \tag{4.17}$$

Let consider now the following boundary conditions:

$$u_z = ay^2 + by + c = U_{EO_{bottom}} \quad at\ y = 0 \tag{4.18}$$

$$u_z = ay^2 + by + c = U_{EO_{top}} \quad at\ y = H \tag{4.19}$$

where *H* is the thickness of the channel. Finally, the mass conservation condition needs to be satisfied:

$$\int_0^H u_z dy = 0 \Rightarrow \int_0^H \left(ay^2 + by + c\right) dy = 0 \Rightarrow \frac{a}{3}H^3 + \frac{b}{2}H^2 + cH = 0 \tag{4.20}$$

Therefore, from Eq 4.18, when y=0, *c* can be obtained, $c=U_{EObottom}$. Then, *a* and *b* can be found using equations 4.19 and 4.20 resulting in:

$$a = \frac{3}{H^2}\left(U_{EO_{top}} + U_{EO_{bottom}}\right) \tag{4.21}$$

$$b = -\frac{2}{H}\left(U_{EO_{top}} + 2U_{EO_{bottom}}\right) \tag{4.22}$$

The recirculation profile is shown schematically in Figure 4.3a with the velocity profile as a function of channel depth at the center of the channel. The net flow rate of the recirculation is zero due to conservation of mass. An uncharged particle (μ_{EP}=0) would follow the streamlines set up by this flow profile.

Such transverse electroosmotic flow profiles have previously investigated but for micromixing enhancement purposes to actively mix two solutions [72]. These flows can be divided into DC electroosmosis (time-independent), where non-uniform zeta potentials are used to induce a change in the surface charge distribution to mix fluids,[72-74] and AC electroosmosis (time-dependent), where high frequency (~1 khz) and low frequency

(~1 hz) EO flow recirculation has been studied [75-78]. In addition, by using spatially patterned electrodes integrated along the length of a microchannel, a helical recirculation path down the length of the channel was produced which promoted mixing of rhodamine B dye using DC fields [79, 80].

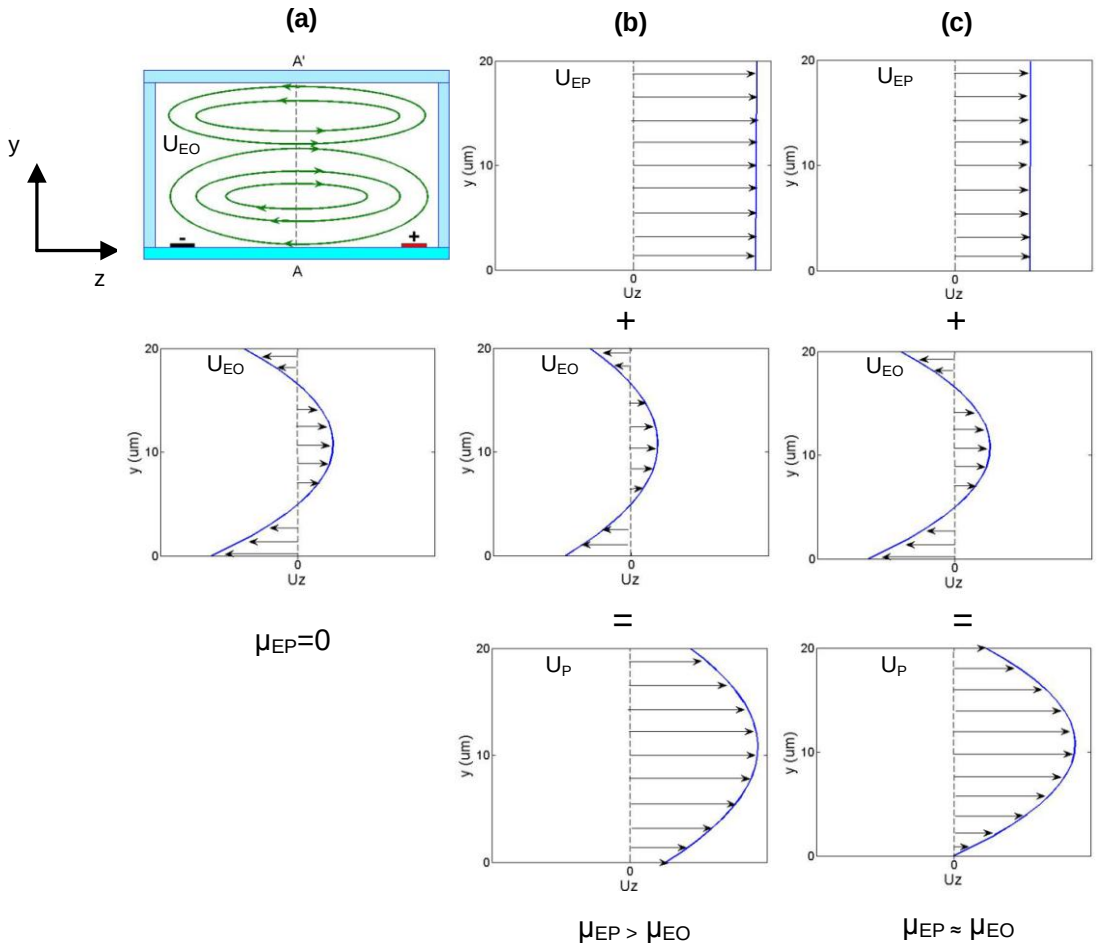

Figure 4.3: EP velocity, transverse EO flow velocity and net particle velocity in a closed glass/PDMS microchannel (cross-sectional view). (a) EO flow only ($\mu_{EP}=0$), (b) EO flow and high EP force ($\mu_{EP}>\mu_{EO}$), and (c) EO flow and EP force with similar mobility values ($\mu_{EP}\approx\mu_{EO}$).

However, if the particle has a significant surface charge, it will feel an additional EP force where the local particle velocity is the superposition of the EP velocity with the EO flow velocity. When the EP mobility is larger than the EO mobility ($\mu_{EP} > \mu_{EO}$) then the particle velocity at the channel center is estimated look like Figure 4.3b and have a positive magnitude throughout the depth of the channel. In this case, the particle can migrate towards the biased electrode, traverse the channel width, and ultimately collect at the electrode surface.

If the EP mobility and EO mobility are approximately of equal magnitude ($\mu_{EP} \approx \mu_{EO}$) then the particle velocity at the channel center will behave as shown in Figure 4.3c. In this case, the wall velocity is now expected to be close to zero while the rest of the velocity profile is in the positive direction. Any particle flowing with a net positive velocity (away from the channel top and bottom) will ultimately recirculate around and back across the channel due to the recirculation flow profile set up by the bounding wall. This particle will ultimately migrate to an equilibrium position where the net velocity is zero (either at the wall or in the center of a vortex), allowing trapping of the particle at this position.

4.4 Dielectrophoresis

The dielectrophoretic phenomenon is defined as particle motion generated by an induced dipole moment within the dielectric particle when the particle is exposed to a nonuniform electric field. The DEP dielectrophoretic force does not require a net charge on the particle but involves is brought about due to the relative difference in polarizability of the

particle and surrounding medium through the complex dielectric particle permittivity (ε_p) and a dielectric medium permittivity (ε_m) to induce the particle dipole moment. The effective dipole moment for a spherical particle with radius a is given by [68]

$$p = 4\pi\varepsilon_m a^3 \left(\frac{\varepsilon_p^* - \varepsilon_m^*}{\varepsilon_p^* + 2\varepsilon_m^*} \right) E \tag{4.16}$$

The complex dielectric constant is defined as $\varepsilon^* = \varepsilon + \frac{\sigma}{j\omega}$ where ε is the respective dielectric constant, σ is the electrical conductivity, ω is the electric field frequency, and j the imaginary number. The term in parenthesis is also known as the Clausius-Mossotti factor (f_{CM}). The DEP force can be described by

$$F_{DEP} = \left(p \cdot \nabla \right) E \tag{4.17}$$

Then the effective DEP force is given by [68]

$$\left\langle F_{DEP} \right\rangle = 2\pi\varepsilon_m a^3 \,\mathrm{Re}\left[f_{CM} \right] \nabla \left| E \right|^2 \tag{4.18}$$

From the preceding equation it can be noticed that the DEP force is dependent on the particle size and the electric field gradient squared. Additionally, the field polarity does not affect the migration due to the square dependence and therefore, the force can be then generated by either AC and DC fields.

Moreover, the Clausius-Mossotti factor f_{CM} plays an important role in the DEP force, giving the resulting sign of the force. This factor is frequency dependent then there is a crossover frequency where the force changes sign. When real part of f_{CM} is positive, the particle moves toward areas of high field (positive DEP), typically electrode edges, while when it is negative, particle moves away from high field regions (negative DEP). Due to

this frequency dependence of f_{CM}, DEP can be modulated from positive to negative DEP and vice versa simply modulating the driving frequency above the cross over frequency specific to a particle type using applied AC fields. DEP has been used as an attractive technique to concentrate or separate particles them from other analytes through differences in relative polarizability.

4.5 State-of-the-art of sample concentration devices by electrokinetics forces

To date, the concentration techniques utilized to concentrate both DNA and proteins in diluted sample have included the use of electrophoretic and dielectrophoretic forces. The electrophoretic methods are sample stacking techniques including field-amplified sample stacking (FASS), isotachophoresis (ITP), and pH-mediated stacking. FASS is one of the most widely used pre-concentration methods for both DNA and proteins because it is one of the simplest techniques; achieved by preparing the sample solution with conductivity lower than that of a background electrolyte. An abrupt change in conductivity between the sample and background electrolyte from low conductivity to high conductivity causes a rapid reduction of the local electric field which slows the electrophoretic velocity of an analyte as it passes into the high conductivity region. This velocity reduction ultimately produces a local accumulation of the analyte at the conductivity interface (Figure 4.4). Theoretical and experimental studies were presented first by Burgi and Chien [81] and then Santiago's group provided a mathematical model of the sample concentration [82]. Moreover, FASS has been investigated in combination with μCE injection strategies

improving up to 160-fold the original signal [83]. Also, the use of porous polymer structures to enable a pressure driven injection scheme while avoiding instabilities due to high-conductivity gradients demonstrated a signal increase by a factor of 1100 in fluorescein and Bodipy electrophoretic separations [84].

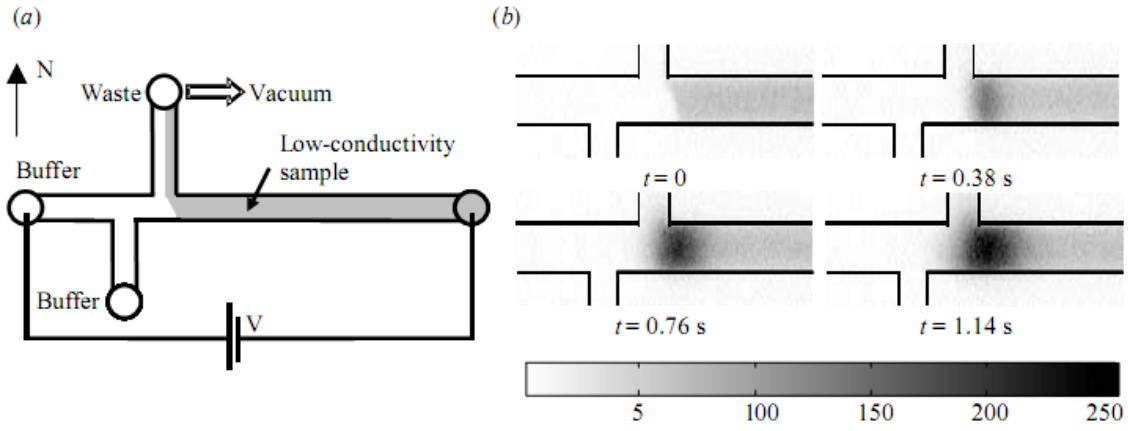

Figure 4.4: FASS stacking: (a) schematic of the low-conductivity sample loading into a high-conductivity buffer and (b) epi-fluorescence images during the stacking [82].

In ITP, a multi-analyte sample is sandwiched between two electrolytes, termed leading and terminating electrolytes, with faster and slower electrophoretic mobilities than the sample solution, respectively. Analytes move forward during voltage application forming discrete high concentration zones according to their electrophoretic mobilities. After a transient period where the discrete zones are formed, the samples stack when moving at constant velocity in the direction of the leader as it is shown in Figure 4.5. ITP has been reported for on-line sample preparation to enrich analytes with low initial concentrations with enhancements in range from 40 fold for SDS-protein [85], 400 folds in ITP-zone electrophoresis chip [86] and up to 100 000 folds for small ions [87]. ITP is not commonly used for the separation of nucleic acids, but rather as a pre-concentration step,

since DNA free solution mobility is relativity constant over a large range of DNA sizes (>0.4 kb) [67].

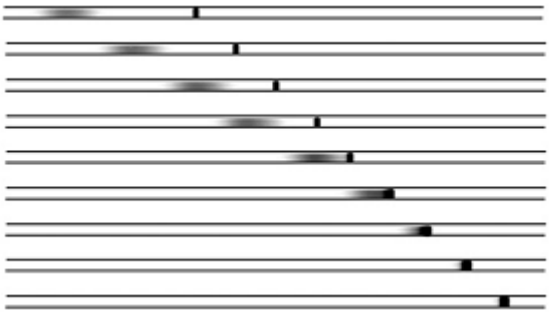

Figure 4.5: Images of isotachophoresis stacking of two samples with different electrophoretic mobility [88].

pH-mediated stacking is another method to pre-concentrate samples by using a pH gradient to decelerate and stack samples (Figure 4.6) similar to the FASS approach described before. A plug containing a sample in a low pH matrix is injected into a microchannel previously filled with a high pH background electrolyte.

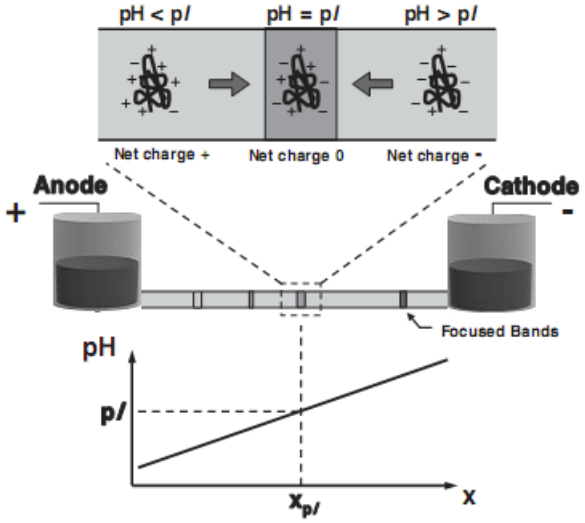

Figure 4.6: Schematic of pH-mediated stacking methodology where analytes migrate to the isoelectric point [5].

A steep pH boundary is developed at the front end of the plug where cationic analytes dissolved in the low pH plug are made anionic once they enter the high pH background electrolyte. This effect focuses the analytes at the pH interface by retarding their movement as they migrate to a detection zone [89]. This approach can not only be used as a pre-concentration method but also as an analyte separation technique using differences in isoelectric point [5, 90]. pH mediated stacking is most applicable to protein solutions due to their widely varying isoelectric points. DNA mobility, on the other hand, is fairly constant over a wide pH range [91].

In addition to purely electrophoretic methods for sample concentration, DEP has been investigated as an additional electrokinetic technique used for sample trapping. As previously noted, when exposed to a non-homogenous electric field, polarizable particles including cells, proteins and DNA can develop a strong electric dipole moment depending upon the relative polarizability of the particle with respect to the surrounding electrolyte that can be used to move them toward (positive DEP) or away (negative DEP) from areas of high electric fields in order to concentrate or separate them from other particles.

Since the dielectrophoretic force is dependent on the square of the field gradient, it often employs alternating current (AC) fields in order to avoid any additional electrophoretic effects, with the polarizability of the particle (positive or negative DEP) being AC frequency dependant as explained previously. Trapping of DNA has been investigated by using DEP with AC electric fields [92, 93] as can be seen in Figure 4.7. In addition, DEP was used in combination with electrode geometric configurations which create non-uniform fields [94, 95] as well as with AC electroosmotic flows [96].

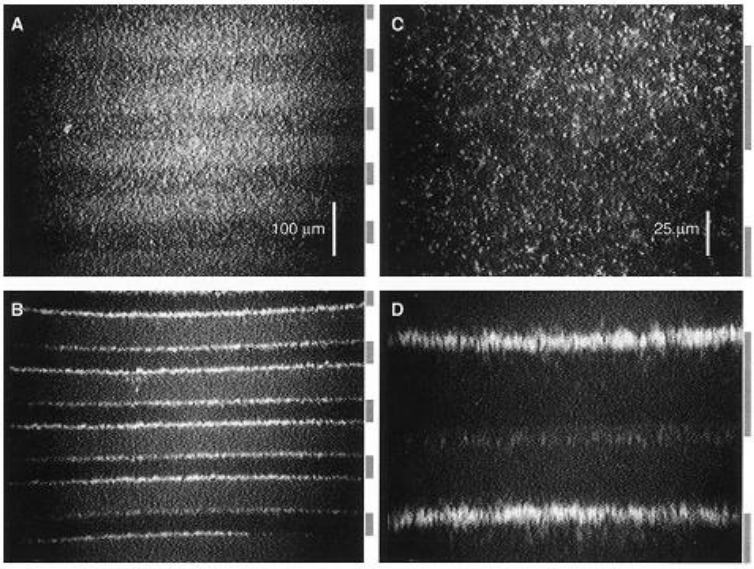

Figure 4.7. Trapping of DNA molecules at the edges of gold-film strips using dielectrophoresis. (a) and (c) before field application, (b) and (d) 1 min after applying a 30-Hz, 200-V p-p signal, nearly all of the molecules became trapped [93].

Additionally, other methods have been explored to capture and concentrate samples using chemical binding through the use of streptavidin-coated magnetic beads,[97] photoactivated polycarbonate surfaces [18] for DNA concentration, and the utilization of membranes for protein concentration enhancements [98, 99]. A size exclusion membrane and the chip schematic used for protein concentration amplification are shown in Figure 4.8.

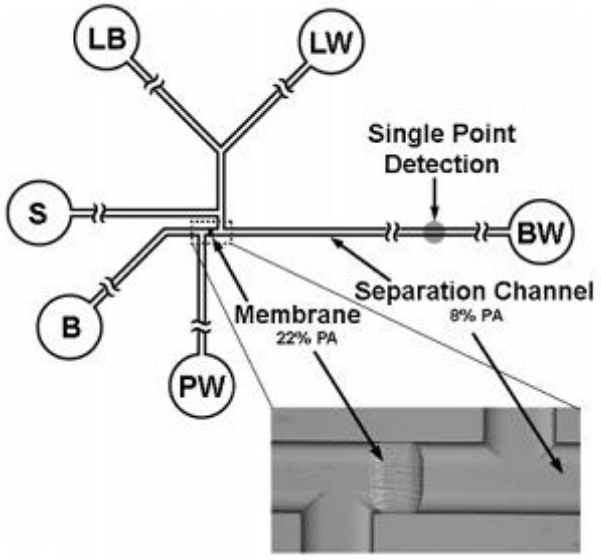

Figure 4.8: Chip layout and image of a photopolymerized size exclusion membrane where analytes are trapped and concentrated [98].

In next chapter, a novel concentration method is demonstrated to continuously enhance DNA and protein sample signal by balancing the electrophoretic force with a transverse electroosmotic flow employing uniform electric fields applied across the width of a microchannel.

Chapter 5

Sample Trapping and Concentration

In this chapter, a converging Y-inlet microfluidic channel with integrated coplanar electrodes is described and tested using transverse uniform DC and AC electric fields to assess the ability of DNA and protein to traverse and concentrate as a preconditioning step for downstream processes.

5.1 Device Fabrication

The microfluidic channel was designed as a two inlet converging and two outlet diverging geometry with a daughter channel 20 μm in depth, 300 μm wide and 5 cm long. It was fabricated using photolithography and soft lithography techniques as previously described in the Chapter 3. The master mold was lithographically patterned using SU-8 negative photoresist (MicroChem, Newton, MA) and then cast in polydimethylsiloxane (PDMS) by mixing the elastomer base and curing agent (Sylgard 184 Silicone Elastomer Kit, Dow Corning, Midland, MI) at a ratio of 10:1 and poured on top of the master mold. The PDMS was degassed in a vacuum chamber and then cured in an oven at 65˚C for 1 hour.

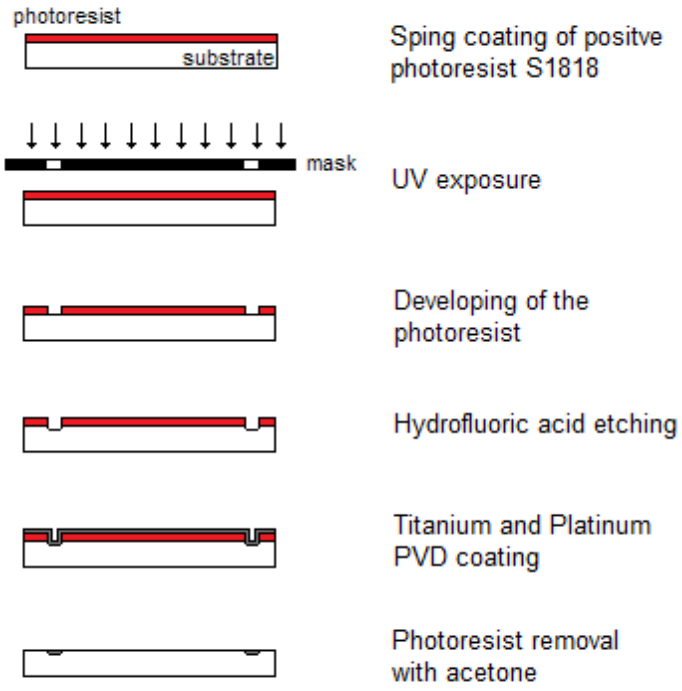

Figure 5.1: Schematic of the fabrication steps required to obtain metal electrodes on glass substrate.

On the other hand, the electrode design was a pair of co-planar electrodes with a center to center separation distance of 231 μm and electrode width and length of 45 μm and 5 cm, respectively. The fabrication was made by patterning the feature from a mask onto a glass slide using a lift-off technique as described in Figure 5.1. First, the slide was lithographically patterned and developed using Microposit S1818 positive photoresist (Microposit, Marlborough, MA, USA). In the exposed area, the positive photoresist washed away during developing leaving the glass exposed for deposition. Then, the patterned glass slides were recessed slightly by submerging the slides in 5:1 buffered

hydrofluoric acid for 1 minute. Subsequently, the etched slides were placed in a metal sputtering system (Kurt Lesker PVD 75, Kurt J. Lesker Company, Pittsburgh, PA) to deposit titanium and platinum resulting in a total electrode thickness of 290 nm. Finally, the photoresist was removed by dissolution in acetone bath using a sonicator. An electrical connection was made by depositing CW2400 conductive epoxy (Chemtronics, Kennesaw, GA) onto the terminals of the patterned electrodes and attaching wires connected to an external power supply. The electrode fabrication steps and settings are also described in more detail in Appendix A.

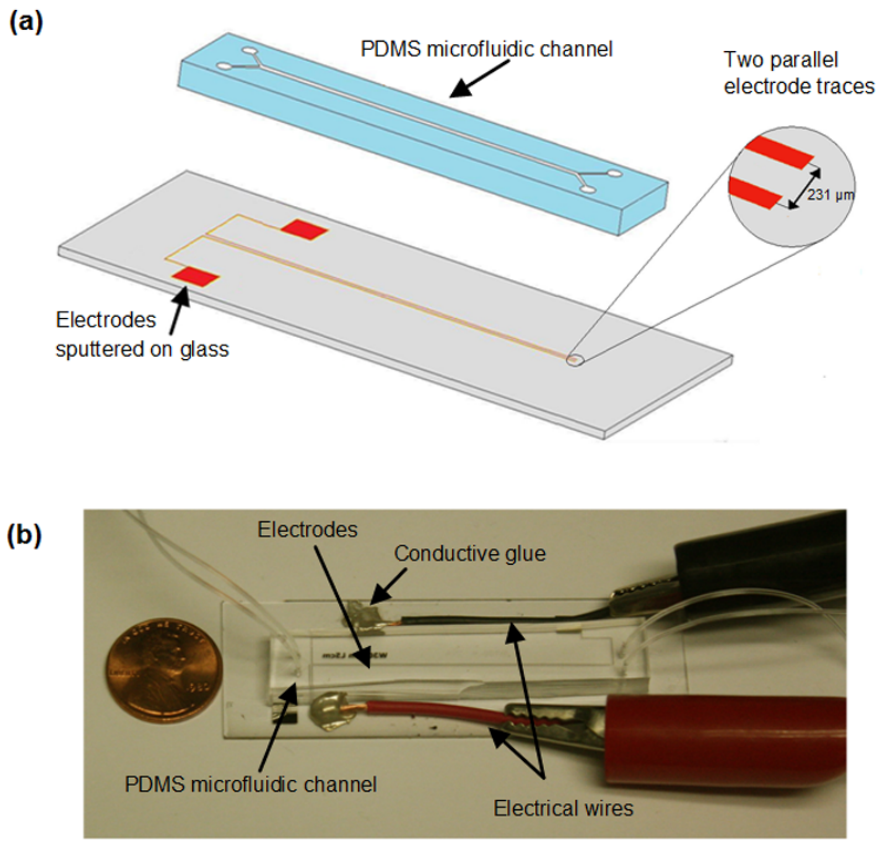

Figure 5.2: (a) Schematic of the electrical and microfluidic components of the device and (b) photograph of the PDMS microchannel with co-planar electrodes.

The glass slide containing the electrode pattern was then irreversibly bonded to the PDMS microchannel structure by surface activation of the glass and PDMS with oxygen plasma at 100 W, 300 mTorr, for 60 sec. Small drops of methanol were placed on both the glass and PDMS surfaces after the surface modification to provide lubrication during the alignment process. The two components were aligned under a microscope and brought into contact to initiate the bonding process. The bonded device was cured at 65°C for one hour. Figure 5.2 shows a schematic of the two device components (Fig 5.2a), PDMS microfluidic channel and the patterned electrodes on the glass slide, as well as a photograph of the assembled device with both electrical and fluid connections (Fig 5.2b).

5.2 Materials and Buffer Characterization

DNA and protein samples of known concentrations were infused into the device diluted in three different buffers to investigate their influence in the DNA migration. The buffer was either 1× TBE buffer (89 mM Tris Base, 89 mM Boric Acid, 2 mM EDTA pH 8.0) (Rockland, ME), 1× TE buffer (10 mM Tris-HCl, 1 mM EDTA pH 8.0) (Rockland, ME), or 1× PBS (HyClone, Thermo Scientific, Logan, UT). Lambda phage DNA (48 kbp) and pUC19 vector (2,686 bp) were purchased from New England BioLabs (Beverly, MA) and labelled using a fluorescent YOYO-1 intercalating dye as described in Chapter 3. All DNA samples were prepared at a 0.05 μg/μl as final concentration. BSA protein (Omnipur, fraction V; EMD Biosciences) was conjugated with 5-6-carboxy-tetra-methylrhodamine (TAMRA) succinimidyl ester dye (Fluka, Switzerland), using the same labeling procedure explained in Chapter 3, and finally diluted at a 0.25 μg/μl

concentration in the appropriate buffer solutions (1× TE buffer and 1× TBE buffer). The sample preparation protocol is described in Appendix B.

The buffer characterization was also made to obtain electrical properties of the buffers used in this work. That includes electrical conductivity, ionic strength, zeta potential and electroosmotic velocity, summarized in Table 5.1.

The electrical conductivity is the buffer's ability to conduct an electric current and can be calculated as $\sigma = F^2 \sum_{i=1}^{n} c_i \nu_i z_i^2$, where F is the Faraday constant, c_i is the molar concentration, ν_i the ionic mobility and z_i the charge of species i [58]. The total buffer conductivity was measuring using a digital conductivity meter (Oakton Instruments, Vernon Hills, IL, USA). For each buffer, three different readings were taken and then averaged, with prior rinsing of meter probe in DI water between the buffer measurements to assure a correct reading.

Table 5.1. Comparison of electroosmotic mobilities for buffer used

Solution	*Conductivity (μS/cm)*	*Ionic Strength (mM)*	*Zeta Potential (mV)*	*EO Mobility (cm^2/Vs)*
TBE	859	105	-48.05	3.40×10^{-4}
TE	739	13	-68.13	4.80×10^{-4}
PBS	15000	137	-22	1.50×10^{-4}

The ionic strength is the measurement of the ion concentration in that solution which plays a central role to describe the formation of the electrical double layer at the wall. For

each buffer, the ionic strength was calculated using the expression $I = \frac{1}{2}\sum_{i=1}^{n} c_i z_i^2$ [100]. Finally, the zeta potential resulting in glass/PDMS microchannel walls wetted with the buffers used in here were found in literature [101] and used to calculate the electroosmotic mobility by employing Eq. 4.5, where $\varepsilon = \varepsilon_o \varepsilon_r$ and considering water properties (ε_r = 80 and μ = 0.001 Pa·s).

5.3 Experimental Setup

The microfluidic device was connected with 0.254 mm ID Tygon tubing (Small Parts Inc., Miami Lakes, FL) to glass syringes (Hamilton, Reno, NV) and the fluid infusion was made via syringe pumps (PicoPlus 22, Harvard apparatus, Holliston, MA).

Since the center to center electrode spacing is 231 μm, a relatively large electric field can be generated at low DC voltages (3 V_{DC} or less) in order to avoid solution electrolysis. The electric field was applied as a constant DC field using a DC power supply (Agilent Technologies, model E3631A). A pulsed DC and AC fields were also be employed by using a signal generator (Agilent Technologies, model 33220A) and high-voltage amplifier (Tegam model 2350, Tegam Inc., Madison, OH).

In order to visualize the YOYO-1 labelled DNA the fluorescence intensity in the microchannel was observed using a Nikon Eclipse TE2000U inverted microscope (Nikon, Tokyo, Japan) operating in epifluorescence mode with a FITC filter cube (Chroma Technology, Brattleboro, VT) and a charged coupled device (CCD) camera (PowerView 1.4 MP, TSI Incorporated, Shoreview, MN) was used to acquire microscopy

images. All the images were acquired using a 10× objective, neutral density filter ND1 for the epifluorescence arc lamp (Nikon, Tokyo, Japan), a 100-ms exposure time at 5 frames per second. The intensity profiles of the images were determined using NIH-ImageJ software (National Institutes of Health), employing *plot profile* function, saving the XY values and plotting them in Matlab (Mathwork Inc.) for better visualization. Concentration enhancement was determined by pixel intensity analysis of the acquired epifluorescent images. These images were used to obtain intensity profiles after background elimination. Concentration enhancement was calculated by normalizing the peak fluorescence intensity of the concentrated DNA after field application to the mean intensity of the solution prior to the application of the electric field. Mass conservation was estimated by using the intensity integral of the DNA concentration profile by the sum of the pixel intensity values above a set threshold across the image width.

5.4 Results and Discussion

Transverse migration of DNA in 1× TBE

In order to investigate the DNA migration within a transversely applied electric field, initially DNA samples diluted in 1× TBE buffer were pumped at a fixed flow rate (0.5 μl/min) conjunctly with a clean 1× TBE buffer solution into the main channel where a DC voltage was applied transversally across the channel via the coplanar electrode pair.

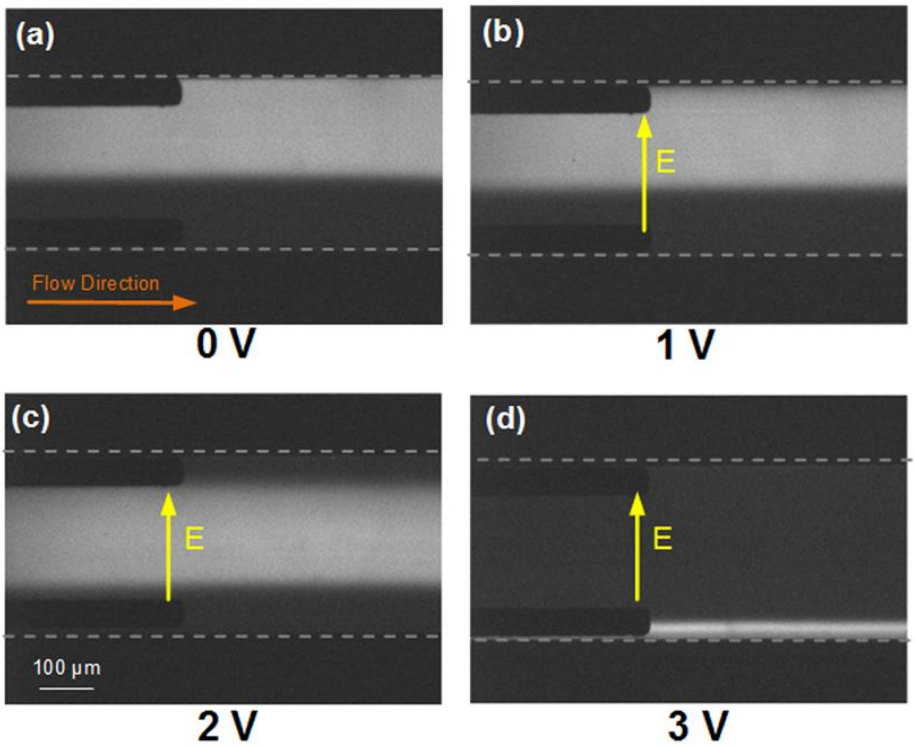

Figure 5.3: Transverse electrophoretic migration of pUC19 vector in 1× TBE buffer (bottom-up view). (a) No field is applied, (b) when 1 V_{DC} was applied, (c) 2 V_{DC} and (d) 3 V_{DC}.

Pictures of pUC19 samples at the outlet of the device under different field conditions are shown in Figure 5.3. When a 1 V_{DC} voltage (E_{ave}=43.29 V·cm^{-1}) was applied (Figure 5.3b) DNA migration was not observed and the infused fluids moved parallel to each other just as when no field was applied (Figure 5.3a). When the voltage was increased to 2 V_{DC} (E_{ave}=86.58 V·cm^{-1}), the electrophoretic force was sufficient to produce transverse DNA migration toward the positive electrode located at the bottom of the images. However, the DNA residence time in the microchannel was not long enough for the DNA to traverse the entire width of the channel (Figure 5.3c). When the voltage was increased to 3 V_{DC} (E_{ave}=129.87 V·cm^{-1}), the DNA EP velocity was then high enough that the DNA

could accumulate at the positive electrode and was convected to the device outlet by the axial pressure-driven flow (Figure 5.3d). The DNA would concentrate at the electrode in approximately 15 seconds after turning on the power supply.

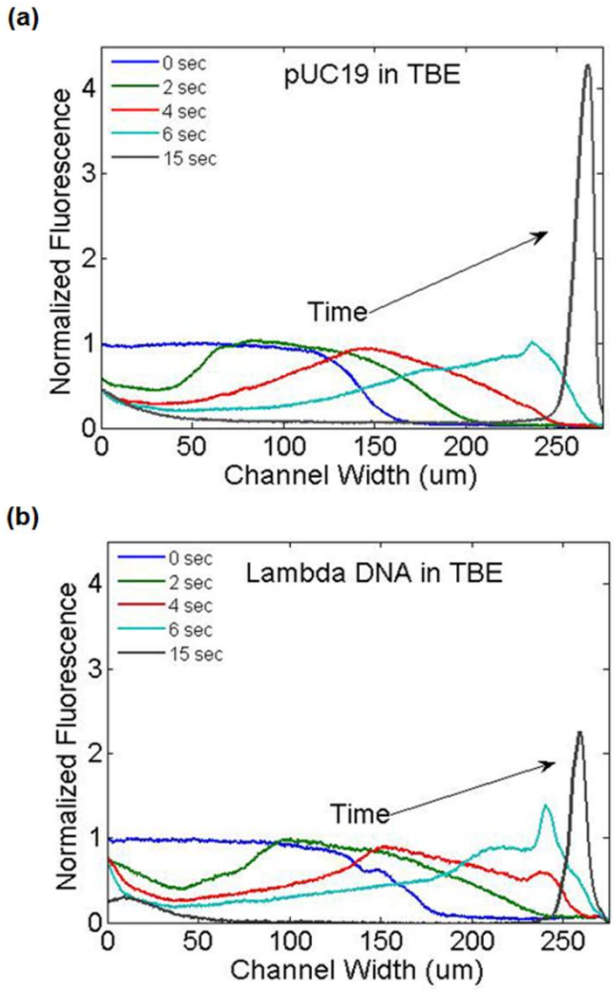

Figure 5.4: Fluorescence intensity profiles of pUC19 (a), and λ-phage DNA samples (b) in 1× TBE buffer across the channel width and at different times after the field is applied showing the transverse DNA migration.

In addition to the experiments using pUC19, circular double-stranded DNA plasmid (2,686 bp), same experimental conditions were repeated using λ-phage DNA, linear

double-stranded linear DNA (48 kbp), observing the same electrophoretic movement towards the positive electrode. Intensity profiles for both types of DNA at the outlet of the device as a function of time are shown in Figure 5.4. DNA was found to be increased 4 fold for pUC19 and 2 fold for λ-phage DNA over the original infused DNA intensity according to the peak fluorescence intensity.

The area under the fluorescence intensity profile was also calculated, comparing the intensity integral between the initial (no field) and final (concentrated) DNA solutions to estimate the total amount of DNA in the images. The concentrated intensity areas were 169% and 110% compared to the original intensity profile without an applied field, for pUC19 and λ-phage DNA respectively.

No significant difference was found in the temporal evolution of the DNA trapping at the positive electrode between the short (pUC19) or long (λ-phage) DNA types, agreeing with previously observed results demonstrating size independence during free solution electrophoresis for DNA fragments bigger than 400 bp [67].

Transverse migration of DNA in 1× TE

Following, the same experimental conditions were repeated except that the solution buffer was changed, replacing the TBE buffer with 1× TE buffer in both the DNA solution and the receiving buffer. By changing the electrolyte solution to a low ionic strength buffer, the DNA then showed a different migration behavior (Figure 5.5) compared to when 1× TBE was used as a buffer (Figure 5.3).

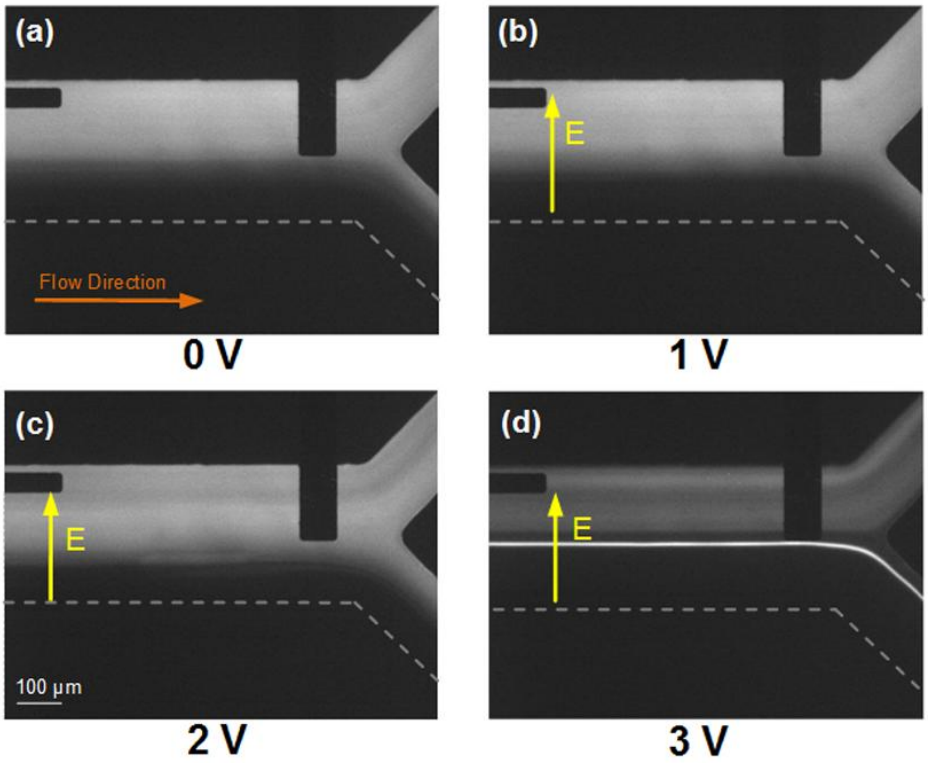

Figure 5.5: pUC19 electrophoretic migration and concentration in 1× TE buffer (bottom-up view). (a) No field is applied, (b) when 1 V_{DC} was applied, (c) 2 V_{DC} and (d) 3 V_{DC}.

The DNA solution in TE buffer using different voltages values are depicted in Figure 5.5. As shown in Figure 5.5b-c, the lower applied voltages produce very little DNA migration across the channel width. However, when the voltage is raised to 3 V_{DC} (Figure 5.5d), the DNA migrates towards the positive electrode but it reached a stable position in the center of the channel where it was trapped and concentrated. This is in contrast to Figure 5.3d where the DNA migrates completely across the channel to the positive electrode. Following the application of voltage, it takes the DNA approximately 10 seconds to migrate to its trapped position.

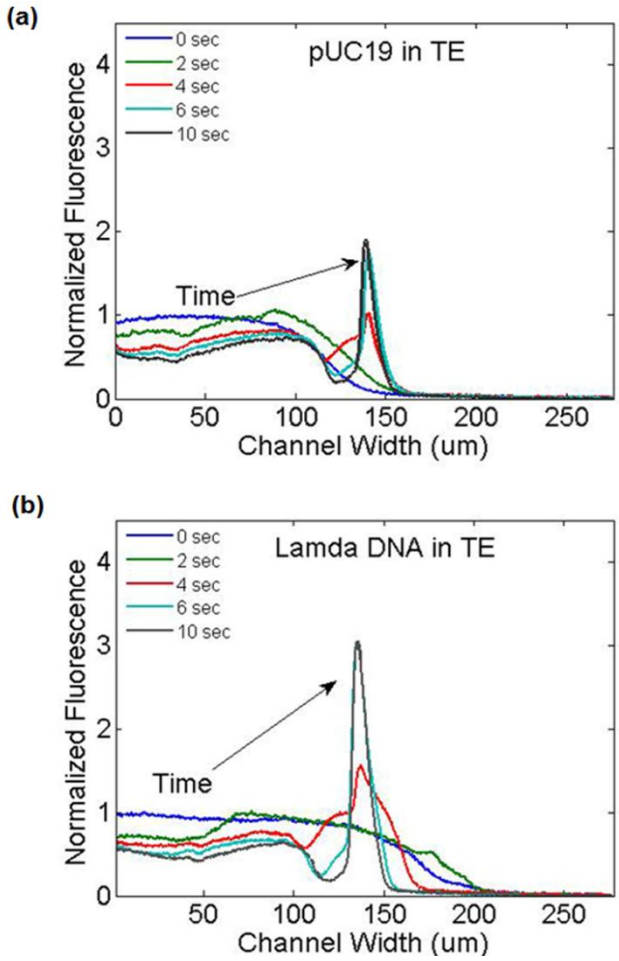

Figure 5.6: Fluorescence intensity profiles of pUC19 (a) and λ-phage DNA samples (b) in 1× TE buffer across the channel width and at different times after the field is applied showing DNA trapping and concentration at the channel center.

Figure 5.6 compares the temporal intensity profiles for both pUC19 and λ-phage DNA as they migrate to their steady state position in the center of the channel, again independent of the DNA size and basepair number as observed in Figure 5.4. The peak fluorescence intensity of the concentrated DNA increased 2 fold for pUC19 and 3 fold for λ-phage DNA over the infused DNA intensity. In addition, the concentrated intensity areas were

73% and 129% compared to the zero field intensity profile, for pUC19 and λ-phage DNA respectively.

For both experiments using TBE and TE buffers, the trapping location and transient behavior were highly reproducible over multiple experiments (n=3 for TBE, n=5 for TE). The absolute concentration enhancement varied between experiments, but based on the fluorescence intensity profile of the DNA after it had concentrated at its equilibrium position in both TBE and TE buffers, the DNA concentration clearly increased several fold over the initial infused concentration.

When analyzing fluorescence intensity profiles, it was found that the concentrated intensity integrals which are predictive of DNA mass were usually within ± 30% compared to the zero field intensity profile. Errors in mass quantification are attributed to two main factors, fluorescence quantification and non-specific DNA absorption onto the microchannel surfaces. Since the DNA concentrates to a thin line, the concentrated intensity integrals are only summed over a pixel width of ~50 pixels which can lead to errors in the integral quantification. Second, due to non-specific absorption of DNA to the channel surfaces DNA could be lost in other areas of the channel or accumulate at the location where the DNA concentrated leading to a larger measured fluorescence intensity. This was particularly apparent when using a low ionic concentration buffer such as TE, where a non-specific background fluorescence intensity can be seen in the top half of the channel even after the DNA was concentrated (Figure 5.5d). It was also found that when channels were flushed with buffer following DNA concentration, the area where the DNA was concentrated was still slightly fluorescent indicating non-specific adsorption of the DNA to the channel surface (data not shown).

Transverse migration of proteins

In addition to experiments using DNA samples, experiments were conducted to assess the ability to trap and concentrate proteins. When using anionic BSA protein (pI=4.7), the same trapping behavior seen when using DNA in both TE and TBE buffers was observed (Figure 5.7). When TBE was used as a buffer, the protein migrated completely to the positive electrode (Figure 5.7b) but was trapped and concentrated in the channel center when diluted in TE buffer (Figure 5.7c), similar to the DNA behavior in Figure 5.3 and 5.5, respectively.

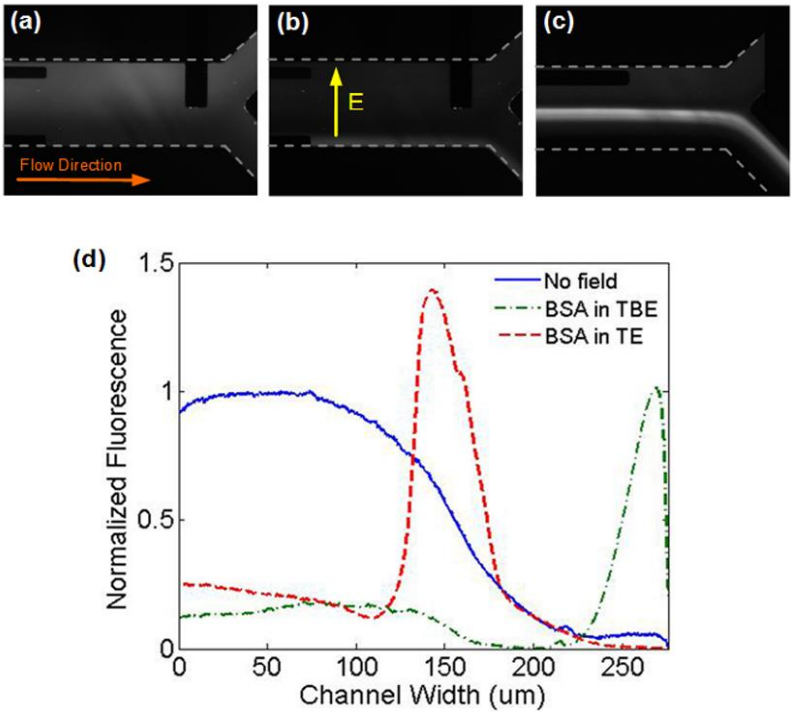

Figure 5.7: Rhodamine labeled BSA migration using 1× TBE buffer and 1× TE buffer. (a) image of BSA when no field was applied, (b) BSA in 1× TBE buffer when 3 V_{DC} is applied, (c) BSA in 1× TE buffer when 3 V_{DC} is applied, and (d) fluorescence profiles across the channel width.

The intensity profiles are shown in Figure 5.7d and appear to be slightly wider than those observed when using DNA. The possibility of concentrating proteins gives this method a new prospective to assess lower detection points for multiple diagnostic applications.

Further investigation of migration dynamics using pure AC field and pulsed field

In experiments using either TBE or TE buffers, the electrical conductivity across the width of the channel is homogeneous, so the electric field should also be constant across the width of the device so other electrokinetic phenomena like FASS, isotachophoresis or dielectrophoresis are not expected.

Several experiments were conducted to better understand the dynamics of DNA migration observed in order to rule out other mechanisms such as DEP, axial flow dependence, to enhance the migration, and to observe the recirculation flow profile predicted in Figure 4.3a.

First, a pure AC field or square wave was applied across the electrodes to investigate the occurrence of dielectrophoresis effects due to field inhomogeneities. Figure 5.8 shows the DNA sample diluted in 1× TE buffer and infused at 0.5 μl/min during the application of an square wave ($3V_{peak}$ at 1 MHz). As a result, the DNA did not migrate transversely across the channel as seen when using DC electric fields. When using AC or square wave fields, the time averaged applied voltage is zero so analytes move in one direction during the first half cycle of the wave and in the opposite direction during the other half cycle, resulting no noticeable net migration. It is noted that the trapping observed using DC fields is the result of the field polarity. In addition, this demonstrates that DNA

dielectrophoresis, which is polarity independent, is not the trapping mechanism seen in this work.

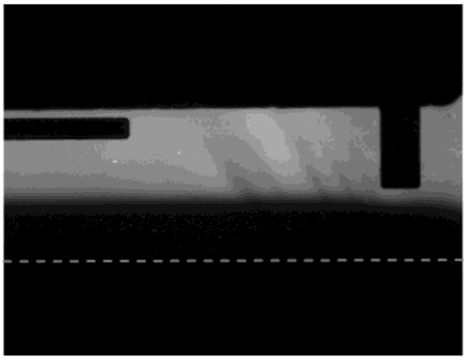

Figure 5.8: DNA sample under alternative square wave 3 $V_{peak\text{-}to\text{-}peak}$ (bottom-up view).

To observe any influence of the axial parabolic flow on the DNA migration, the perfusion flow rate was also varied. In Figure 5.9, images of pUC19 in 1× TE buffer were acquired at the entrance of the channel, where three flow rates were compared: 0.5 μl/min (5.9b), 0.3 μl/min (5.9c) and 0.1 μl/min (5.9d). The flow rate affects the position along the length of the channel where the DNA concentrates but not the transverse location and width of the concentrated DNA plug. A decrease in the axial velocity allows the DNA to concentrate closer to the entrance of the channel, since the DNA is convected forward at a slower velocity. At 0.5 μl/min, the initial DNA migration can be seen but DNA trapping occurs further down the channel and was not observed at entrance region. At 0.3 μl/min and 0.1 μl/min, the DNA begins to concentrate towards the center of the channel and is captured in the images at the channel entrance. As shown here, the pressure driven flow only affects in the residence time of the trapping but the transverse location and width of the concentrated DNA plug did not change.

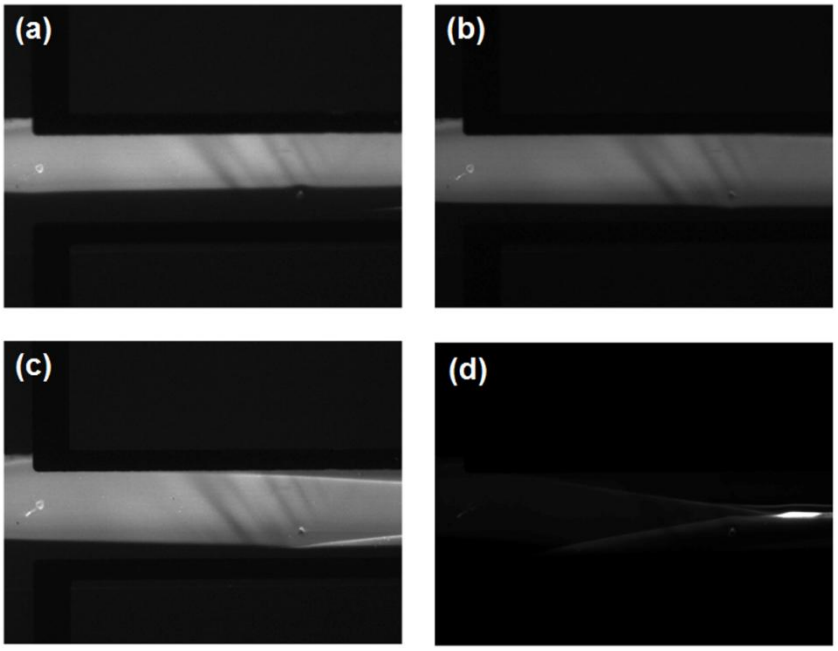

Figure 5.9: Images at the main channel entrance of DNA samples in 1× TE buffer at different flow rates (bottom-up view). (a) No field, 0.5 µl/min flow rate, (b-d) 3 V_{DC} was applied when the flow rate was (b) 0.5 µl/min, (c) 0.3 µl/min, and (d) 0.1 µl/min.

The voltage used to promote DNA migration was limited by buffer hydrolysis. At applied voltages larger than 3 V_{DC}, formation of electrolysis bubbles was apparent. Experiments were also conducted using a pulsed DC field which showed identical DNA trapping and concentration at the same channels positions as a continuous DC field (Figure 5.10). The pulsed electric field consists of a pulse signal of 15 V_{DC} at a 1 MHz frequency and 20% duty cycle (so the pulse is only applied for 200 ns followed by a 800 ns rest period).

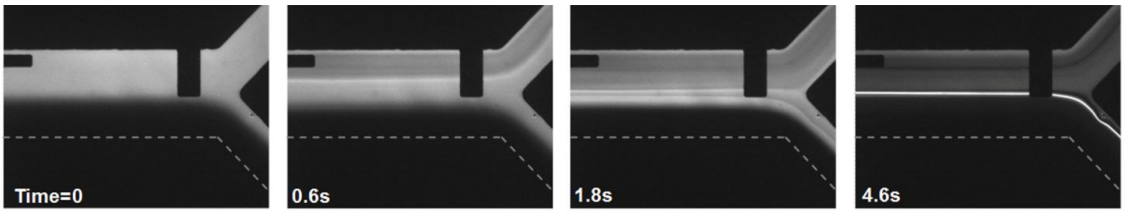

Figure 5.10: Images of pUC19 sample in TE buffer as time increases under a pulsed electric field of 15 V_{DC} at a 1 MHz frequency and 20% duty cycle (bottom-up view).

In this manner the DC field is not applied long enough at each pulse for electrolysis bubbles to nucleate. This allows a higher total electric field to be applied without solution electrolysis. The same DNA concentration behavior is seen as when using a constant electric field, but the DNA accumulates at its equilibrium position much faster that the DC case, reaching the steady state in approximately 5 sec.

Effect of EO and EP mobility on DNA migration and concentration

After discharging the dielectrophoresis force as the driving force for the trapping seen in TE buffer, in this section the other two electrokinetic phenomena, EO flow and EP force are analyzed to explain the mechanism which trap and concentrate DNA and proteins in the center of the channel or accumulate them in the positive electrode, depending of the buffer chosen.

As noted previously, the buffer ionic strength plays an important role in the zeta potential formation. As the ionic strength increases, the double layer becomes compressed resulting in a lower zeta potential and hence lower electroosmotic mobility [61-63]. Therefore, the electroosmotic velocity will be faster in low ionic strength buffers like TE

buffer and slower in TBE and PBS buffers. The EO mobilities are calculated to be 4.80×10^{-4}, 3.40×10^{-4} and 1.50×10^{-4} $cm^2\cdot V^{-1}\cdot s^{-1}$ in TE, TBE and PBS respectively (Table 5.1).

The free-solution EP mobility of DNA is also buffer dependent, decreasing monotonically as the buffer conductivity and salt concentration increase [70, 71]. From literature, the DNA electrophoretic mobility in TBE was found to be 4.5×10^{-4} $cm^2\cdot V^{-1}\cdot s^{-1}$ [67]. No report was found regarding DNA mobility in PBS or TE buffer. However, based on the conductivities of these buffers (Table 5.1), the DNA mobility in TE is expected to be slightly higher that the TBE mobility while the DNA mobility in PBS is expected to be much smaller due to the high NaCl salt concentration (137 mM) and electrostatic shielding [70, 71].

The observed migration behavior of DNA in different buffers could be explained by a balance of EP and EO forces and the effect of the different buffers on the relative EP and EO mobility, as illustrated in Figure 4.3. By changing the solution buffer, the EP and EO mobility can be parametrically changed to observe different migration dynamics and equilibrium DNA positions. The effect of varying buffers is shown in Figure 5.11. The images were acquired at the device outlet showing pUC19 concentration at different locations along the width of the channel depending on the buffer conditions. When a transverse electric field (3 V_{DC}) and pressure-driven flow (0.5 μl/min) were applied, different concentration dynamics were observed using three different buffers.

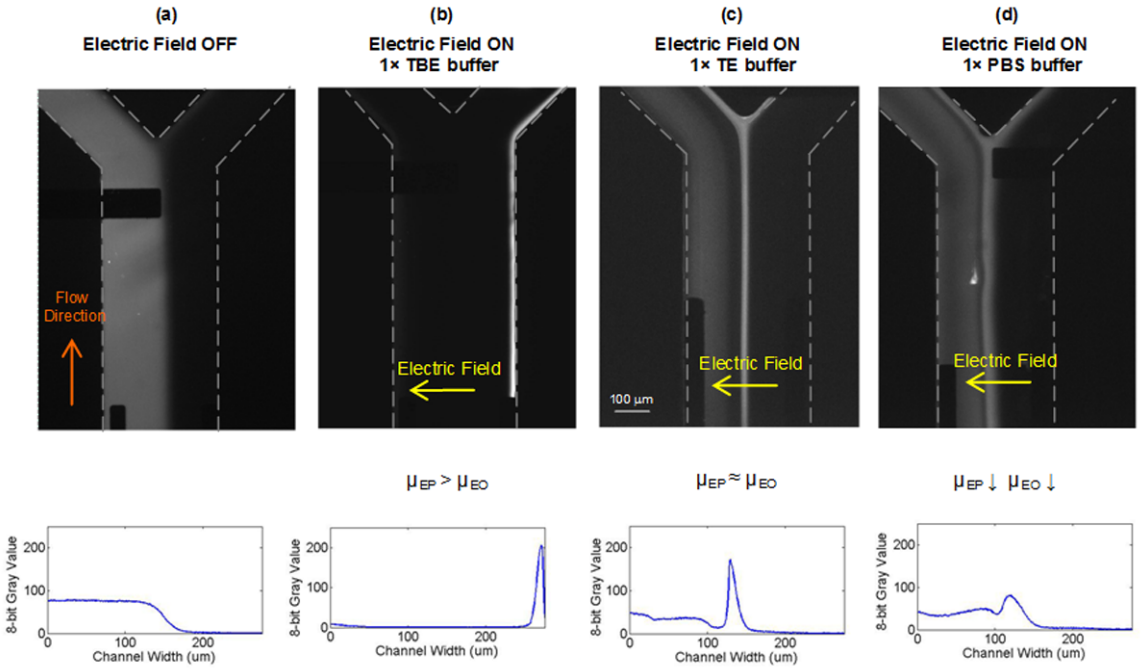

Figure 5.11: Effect of buffer selection on pUC19 migration under transverse DC electric field. (a) No field applied, (b-d) 3 V_{DC} was applied while pUC19 was diluted in three different buffers: (b) 1× TBE, (c) 1× TE, (d) 1× PBS.

When TBE was used as a buffer, the EP mobility (4.50×10^{-4} $cm^2 \cdot V^{-1} \cdot s^{-1}$) is larger than the EO mobility (3.40×10^{-4} $cm^2 \cdot V^{-1} \cdot s^{-1}$) so the net DNA velocity should be positive everywhere along the depth of the channel as shown in Figure 4.3b allowing the DNA to transverse the channel to the positive electrode (Figure 5.11b).

When TE was used as a buffer, the EP and EO mobility are approximately equally (~4.50×10^{-4} versus 4.80×10^{-4} $cm^2 \cdot V^{-1} \cdot s^{-1}$) due to the low ionic strength of the TE buffer, so the migration dynamics are expected to follow those shown in Figure 4.3c where there is a zero velocity point (either at the wall or in the center of the recirculation vortex) which traps the DNA at the center of the channel (Figure 5.11c).

Finally, when PBS was used as a buffer (Figure 5.11d) the DNA migrated partially toward the positive electrode while a large portion of the sample remained in the left side of the channel. The fact that the DNA could not transverse the channel is attributed to both a decrease in the EP and EO mobility so that the recirculation vortex is less prominent while the EP force is also reduced slowing the DNA migration across the channel.

The balance of these two forces, electrophoretic force and the drag force induced by EO flow, therefore determines the DNA migration across the channel. Next, two different approaches are presented to demonstrate the formation of an induced helical EO flow by using numerical simulations and particle visualization.

EO Flow Simulation

The physical model was simplified by assuming a two-dimensional problem using the cross-section area along the channel width. The electrodes are located at the bottom surrounded by glass and connected by top and side PDMS channels (Figure 5.12).

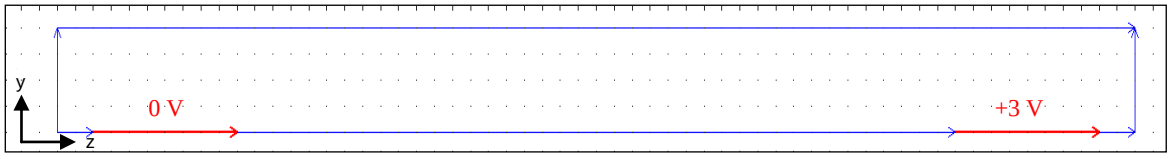

Figure 5.12: 2D geometry representing the cross-section area of the channel.

COMSOL Multiphysics (version 3.3, Burlington, MA) was used for these simulations where the electroosmotic flow can be simulated with MEMS module, by selecting Electroosmotic Flow case in the Microfluidics section and then, Stokes Flow and the

Steady-State Analysis. The Stokes Flow component is used to solve the Stokes equation including the electroosmotic contribution and continuity equation:

$$\mu\nabla^2 u = \nabla p - \rho_E \nabla V \tag{5.1}$$

$$\nabla \cdot u = 0 \tag{5.2}$$

where μ is the fluid viscosity, u the velocity, p the pressure, ρ_E the charge density and V the voltage. At the same time, the Conductive Media DC component is used to solve Poisson equation:

$$\nabla^2 V = -\frac{\rho}{\varepsilon_o} \tag{5.3}$$

being ε_o the vacuum permittivity. The details of all the COMSOL settings for these simulations can be found in Appendix C.

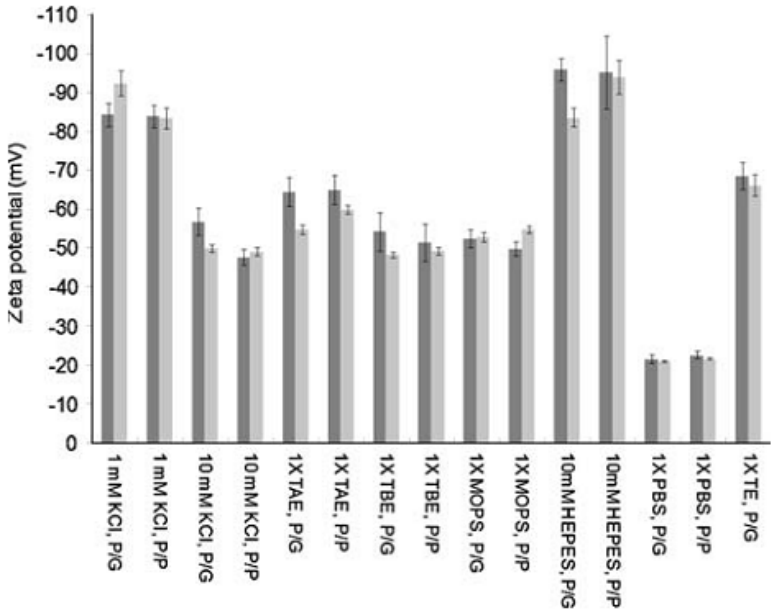

Figure 5.13: Measurements of zeta potentials for selected buffers using PDMS/PDMS and PDMS/glass channels [101].

In order to simulate the EO flow using COMSOL software, it is important to know the zeta potential or EO mobility of the buffer used at the wall of interest, which could be PDMS (top and side walls) or glass (bottom).

According to the literature, the zeta potential at different materials depends highly on the electrolyte type and the ionic strength. As can be seen in Figure 5.13, the difference in zeta potential between the PDMS/PDMS channels and the PDMS/glass varies from buffer to buffer, being higher at PDMS/glass channels in some of the buffers and lower in others [101]. For example, in Figure 5.14 for N-(2-acetamido)-2-aminoethanesulfonic acid (ACES) buffer, it is shown that at high ionic strength the zeta potentials at PDMS/glass and PDMS/PDMS surfaces are comparable but, for low ionic strength, the zeta potential in PDMS/glass is much higher than the one in PDMS/ PDMS [62].

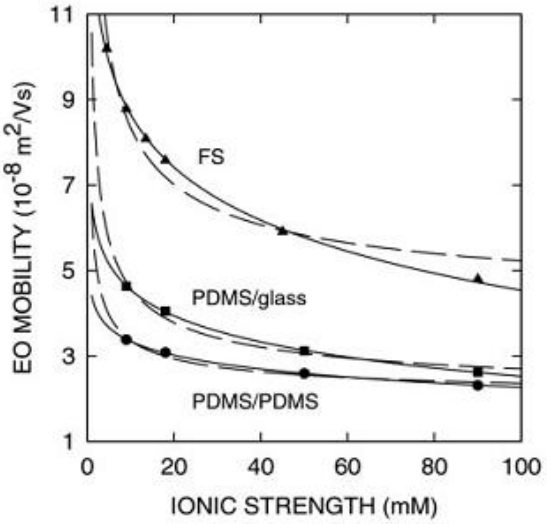

Figure 5.14: EO mobility as function of ionic strength for ACES buffer using fused silica, PDMS/glass and PDMS/ PDMS channels [62].

Table 5.2 summarizes the zeta potential and EO mobility values used in the simulation. The TBE and PBS mobility values were extracted from Figure 5.13, using the light color columns (total length method [101]) and considering that the PDMS/glass value is the average of PDMS/PDMS and glass/glass values to consequently obtain the zeta potential at the glass surface. In the case of TE buffer, PDMS/ PDMS data for that buffer was not provided in the Figure 5.13. Therefore, it was assumed that the zeta potential decreases to -50 mV on PDMS surfaces and then this value was used to calculate the glass zeta potential. The PDMS/PDMS mobility obtained for TE buffer was 3.52×10^{-4} $cm^2\cdot V^{-1}\cdot s^{-1}$ which agrees with Figure 5.14 for low ionic strengths (TE ionic strength=13 mM).

The EO mobilities showed in table 5.2 were used as boundary conditions for the stokes flow while the electrical boundary conditions were 0 and $+3V_{DC}$ in the left and right electrode, respectively, as shown in Figure 5.12, and defining electrical insulation for the glass and PDMS walls.

Table 5.2. Zeta Potentials and EO mobilities at different surfaces for each buffer used

Solution	TBE		TE		PBS	
Material	*Zeta Potential (mV)*	*EO Mobility (cm^2/Vs)*	*Zeta Potential (mV)*	*EO Mobility (cm^2/Vs)*	*Zeta Potential (mV)*	*EO Mobility (cm^2/Vs)*
PDMS/Glass	-48	3.40×10^{-4}	-68	4.8×10^{-4}	-22	1.55×10^{-4}
PDMS	-49	3.45×10^{-4}	-50	3.52×10^{-4}	-23	1.62×10^{-4}
Glass	-47	3.3×10^{-4}	-86	6.05×10^{-4}	-21	1.48×10^{-4}

Figures 5.15, 5.16 and 5.17 show the simulations results obtained for TBE buffer, TE buffer and PBS buffer, respectively. The potential and the electric field streamline are

shown in Figures 5.15a, 5.16a and 5.17a, where the field density increases near the electrode edges and being equal in three cases.

Figures 5.15b, 5.16b and 5.17b illustrate the electric field over the cross section area and the streamlines represent the mean velocity of the fluid. Using different buffers, the generation of two recirculating flow is observed in all of them, where it can be noticed that the vortices are less concentric as the difference between the top and bottom electroosmotic mobilities increases. In addition, these profiles show that near the electrode edge, where the electric field is higher, the formation of small circulation path can be seen as part of a secondary flow.

The bottom graphs, Figures 5.15c, 5.16c and 5.17c, represent the velocity field plotted as a surface plot and velocity arrows showing the velocity profile at different points in the z direction, along the width of the channel. It can be observed that the velocity at the wall is negative and has the same direction as the electric field. This flow represents the movement of the positive charges at the electric double layer near the top and bottom surfaces as shown in the previous chapter (Figure 4.1). Consequently, the bulk fluid moves as a result of the drag forces induced by these ions at the wall. However, the velocity field of the bulk fluid changes direction close to the center of the channel height allowing the flow recirculation due to the enclosing walls to conserve mass.

The EO flow simulation obtained here is similar to the flow proposed in Figure 4.3a in Chapter 4. However, the simulation results are more elliptical due to the high aspect ratio between the width and the height of the device.

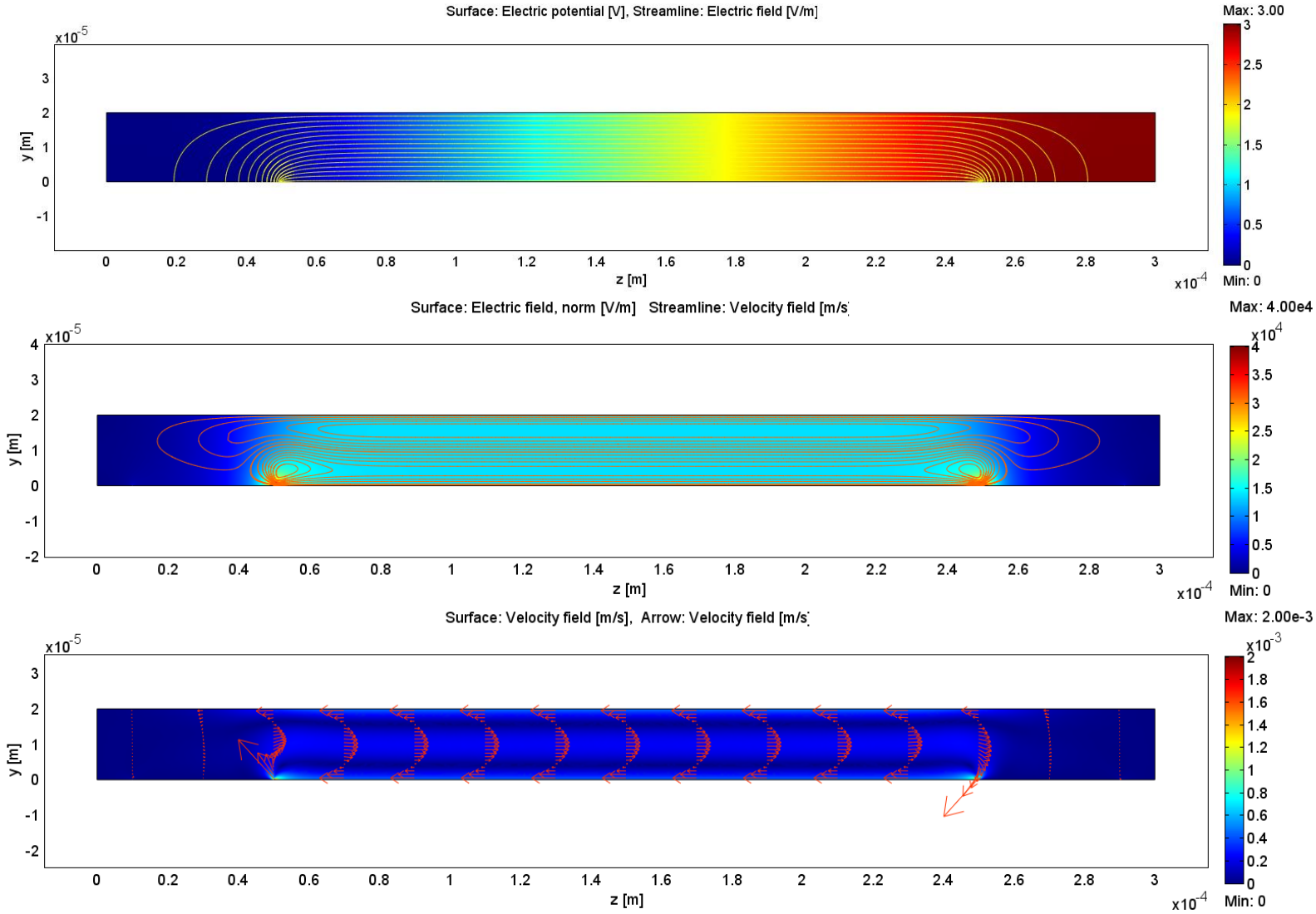

Figure 5.15: TBE buffer case: (a) potential surface plot and field streamlines, (b) field surface plot and velocity streamlines, (c) velocity field surface plot and arrow plot.

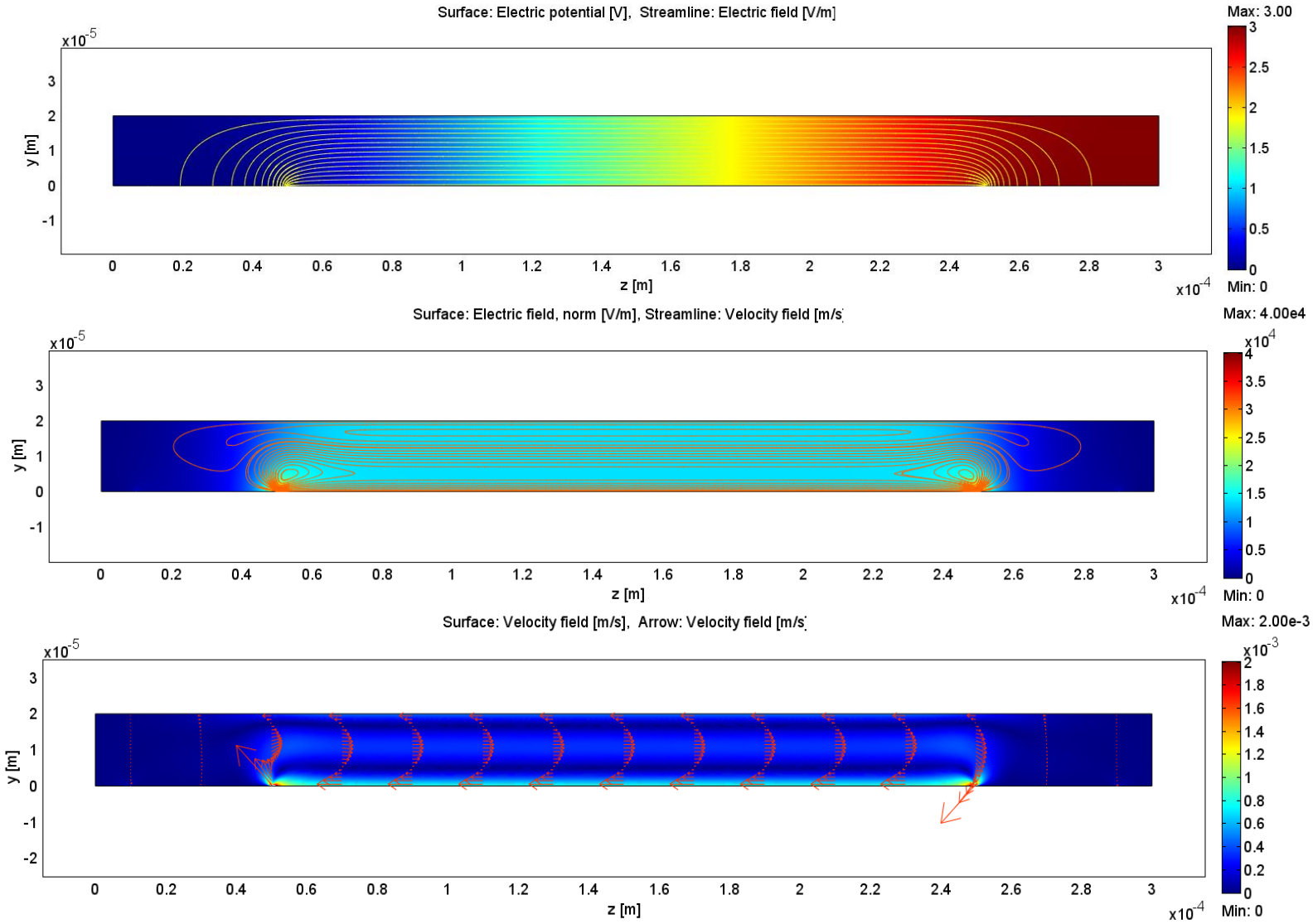

Figure 5.16: TE buffer case: (a) potential surface plot and field streamlines, (b) field surface plot and velocity streamlines, (c) velocity field surface plot and arrow plot.

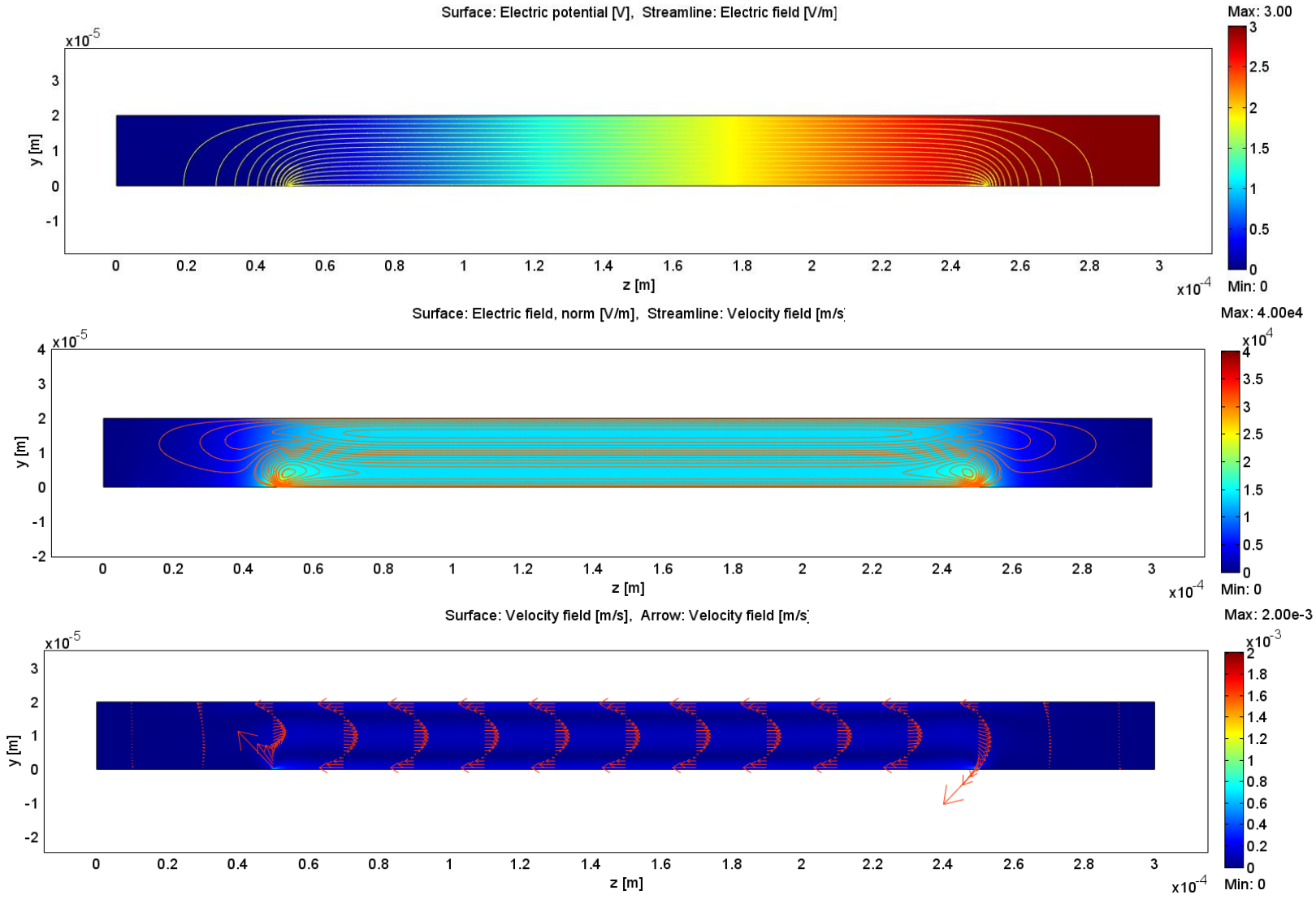

Figure 5.17: PBS buffer case: (a) potential surface plot and field streamlines, (b) field surface plot and velocity streamlines, (c) velocity field surface plot and arrow plot.

The three cases presented differ from each other by the magnitude and the relative difference in EO mobility between top and bottom surface which produce a different velocity magnitude and asymmetry along the channel height.

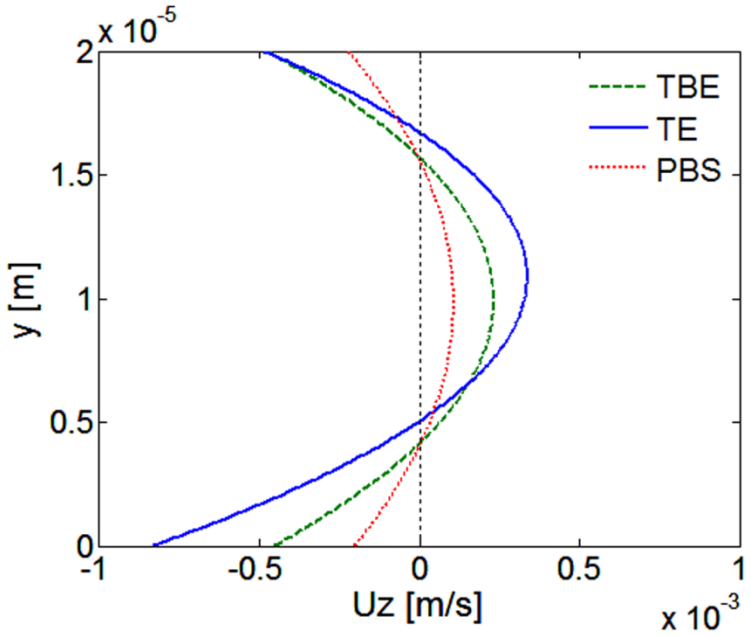

Figure 5.18: Electroosmotic velocity profiles in z direction (U_z) at the center of the channel and across the channel height for TBE, TE and PBS buffers.

Among the three cases, the TE buffer generates the largest and the most asymmetric EO flow as can be observed in Figure 5.18. On the other hand, the velocity generated using PBS buffer is the lowest one due to the EO mobility reduction in high ionic strength buffers. Finally, the TBE case is in between the former cases where the EO flow is still noticeable and approximately symmetric.

To determine the net velocity of DNA traveling within this recirculation flow profile, the EP velocity of the analyte in the corresponding buffer is added to the EO profile to obtain the net velocity of the analyte of interest. From Stellwagen *et al* work [67], the EP

mobility of DNA in TBE was found to be 4.5 $\times 10^{-4}$ $cm^2 \cdot V^{-1} \cdot s^{-1}$, while for DNA mobility in PBS or TE buffer there is no report. However, the DNA mobility in TE is expected to be just slightly higher that the TBE and much smaller in PBS due to the high salt concentration. Using the electric field calculated by the COMSOL simulation, the EP velocity in TBE was found to be 0.62 $\times 10^{-3}$ $m \cdot s^{-1}$ which was added to the EO flow to obtain the net DNA velocity as shown in Figure 5.19. It can be observed there that the net velocity of the DNA is positive all the points along the height of the channel, as predicted in Figure 4.3b, and it goes towards the positive electrode where it was captured during the experiments.

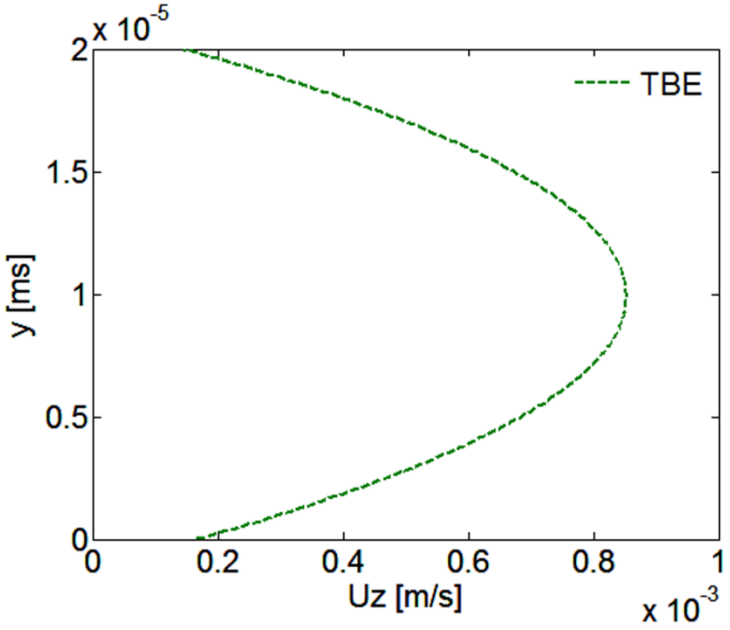

Figure 5.19: Net DNA velocity profile with EO and EP components (U_{EO}+U_{EP}) across the channel height for TBE buffer.

Moreover, if the EP mobility in TE is considered to be similar to the mobility in TBE, then the EP velocity would be also approximately 0.62 $\times 10^{-3}$ $m \cdot s^{-1}$. If this EP velocity is

added to the EO flow velocity for the TE buffer as it is shown in Figure 5.20, the net velocity will not always be positive as seen in the TBE case due to the opposing high EO flow, especially at the glass wall where the EO velocity was found to be higher in magnitude (-0.83 $\times 10^{-3}$ m·s^{-1}) than the estimated EP velocity (~0.62 $\times 10^{-3}$ m·s^{-1}). As a consequence, the net velocity profile have a zero-velocity point near the glass wall where DNA ultimately migrates to this equilibrium position as predicted in Figure 4.3c.

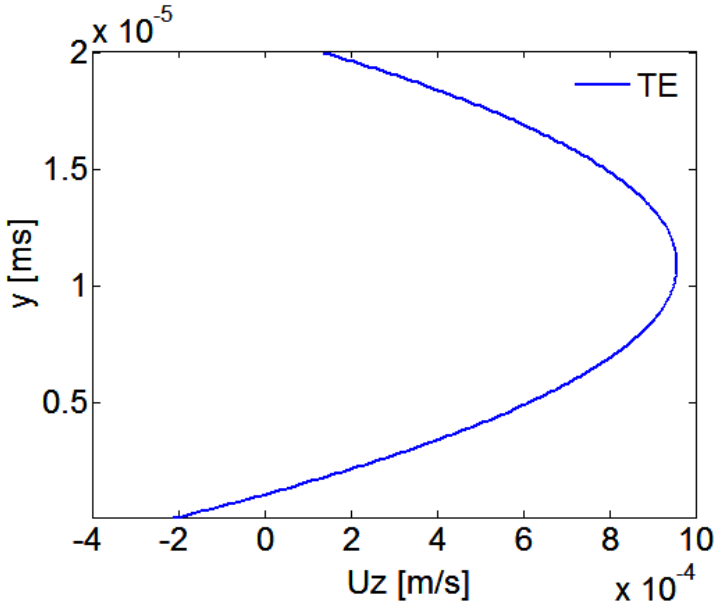

Figure 5.20: Estimated Net DNA velocity profile with EO and EP components (U_{EO}+U_{EP}) across the channel height for TE buffer.

Particle Visualization

There is strong evidence that transverse DC fields in combination with axial fields or pressure driven flows result in a vortical recirculation EO flow profile which follow a helical path down the length of the channel [79, 80]. In order to observe the recirculating

flow, fluorescent uncharged melamine and negatively-charged polystyrene beads suspended in 1× TE buffer were infused allowing visualization of the recirculation vortex.

In Figure 5.21, snapshots of a video acquired at the entrance of the device captured the EO recirculation vortex formation. The charged particles moved quickly to the positive electrodes (thought to be due to the large particle EP mobility). However, the melamine particles recirculated with the EO flow profile moving down the channel in a helical fashion showing the recirculation vortex formed near the center of the channel.

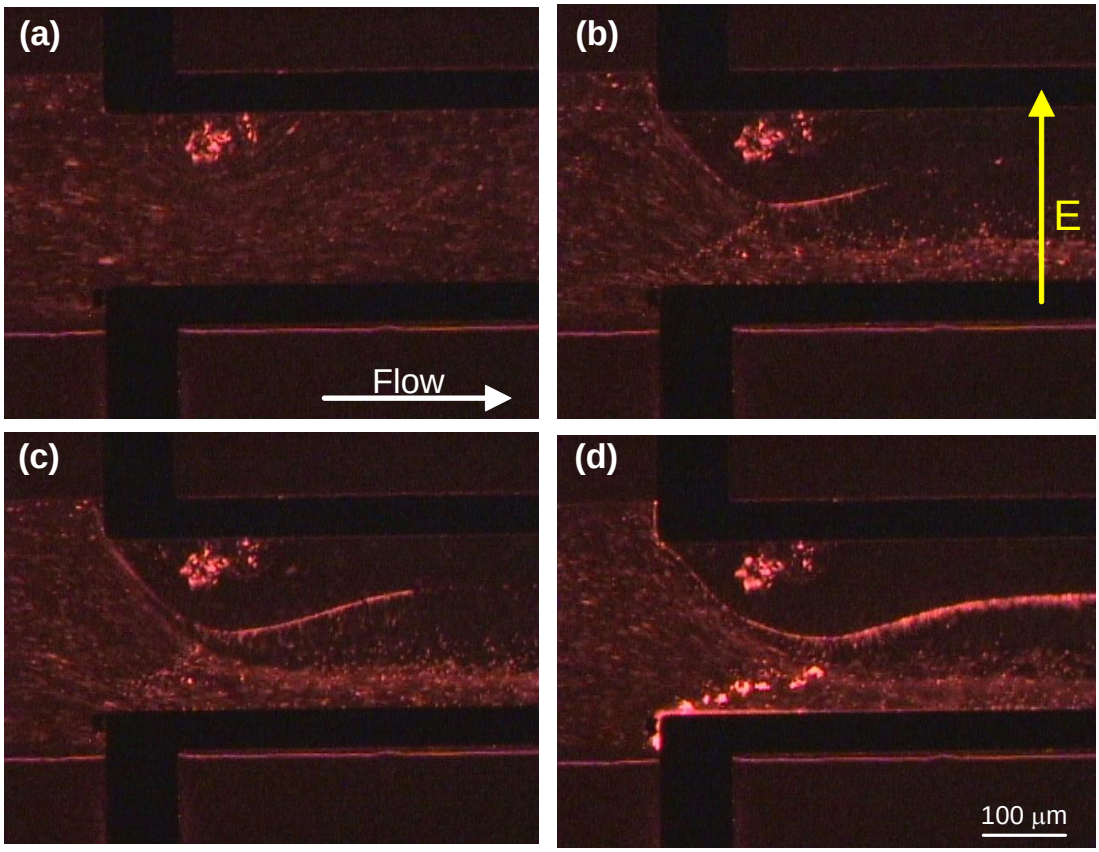

Figure 5.21: Snapshots of a helical flow formation using fluorescent uncharged melamine and negatively-charged polystyrene beads suspended in TE buffer under transverse field.

The visualization shown in Figure 5.21 demonstrates the ability to trap species inside of the channel when a transverse field is applied as a result of the helical electroosmotic flow and the balance with the electrophoresis force.

In summary, a continuous-flow DNA and protein concentration method is demonstrated here by employing uniform DC or pulsed electric fields applied across the width of a microchannel. Negatively charged samples are conjunctly infused in a converging Y-inlet with a receiving buffer of the same conductivity into a main daughter channel where coplanar electrodes running axially along the length of the channel are used to apply a transverse electric field. Depending on the buffer selection, the samples could be concentrated by electrophoretic forces at the positive bias electrode or trapped at an equilibrium position within the channel by balancing the electrophoretic (EP) force with a drag force generated by an induced electroosmotic (EO) flow in the opposite direction. To the author knowledge this is the first report of such trapping and concentration of DNA and protein samples using transverse DC electric fields. Such a technique could have advantages over other electrokinetic preconcentration techniques such as FASS, ITP pH-mediated stacking, and DEP, because it is a simple technique which can be implemented in a continuous flow environment and does not require a conductivity, pH, or field gradient.

In the following chapter, the conclusions for the DNA liquid extraction platform, DNA and protein trapping and concentration will be addressed. In addition, the future work to be explored as a consequence of the finding shown in this research is detailed next.

Chapter 6

Conclusions and Future Directions

The concluding remarks of this original work are presented next, summarizing the results achieved and the future work towards the development of an integrated lab-on-chip device for DNA purification via microfluidic phenol extraction as well as the novel DNA or protein manipulation by transverse electrokinetic balance.

6.1 Microfluidic DNA purification via phenol extraction

Conclusions

In the first part of this dissertation microfluidic platforms have been designed and fabricated using microfabrication techniques to demonstrate DNA purification via liquid phase extraction at the microscale using an aqueous phase containing either protein, DNA or a complex cell lysate and an immiscible receiving organic (phenol) phase.

Initially, a serpentine device was used to investigate protein partitioning between the aqueous and organic phase, and DNA purification when both BSA protein and DNA were mixed in the aqueous phase and infused conjunctly with the phenol phase. This two-phase system was studied using both stratified and droplet-based flow conditions. The

droplet based flow resulted in a significant improvement of BSA protein partitioning (>91% extracted from the aqueous phase into the organic phase) due to the convective flow recirculation inside each droplet improving material transport to the organic-aqueous interface.

A second device was designed and fabricated after the preliminary tests with the serpentine device to specifically extract plasmid DNA from bacterial lysates using only droplet-based flows. The plasmid recovery using the microdevice was high (>92%) and comparable to the recovery achieved using commercial DNA purification kits and standard macro-scale phenol extraction.

These results represent the initial steps towards the miniaturization of an efficient on-chip DNA sample preparation using phenol extraction which could be integrated with post-extraction DNA manipulations for integrated genomic analysis modules.

Future Work

For the first time, phenol extraction was realized at the microscale with high efficiency and comparable with other standard DNA purification methods. In addition, the purification was performed in a continuous manner without the requirements of valves or washing and elution steps, which could allow integration with a pre-conditioning module for cell lysis, and post-extraction manipulation and analysis modules such as enzymatic restriction enzyme digestion and micro-electrophoretic separation.

However, some issues associated with this method must be solved in order to advance full integrated on-chip integration. First, following the DNA extraction module, the

droplets need to be separated into their individual phases where the phenol phase is sent to waste while the aqueous phase containing the DNA can be easily removed and used in downstream processes. For the droplet-based experiments shown here, the two phases were collected together at the outlet and separated by centrifugation outside of the device.

One approach to separate the two phases at a bifurcating outlet could be based on the physical properties and favorable energetic interactions of each solvent with a surrounding wall. By selectively coating one of the outlet channels with a hydrophobic self assembled monolayer (SAM) [54], the phenol phase can be directed into one outlet while the organic phase would be directed to another.

A second approach to investigate is the possibility to extract the organic phase by a pillar array where phenol can be evacuated but the aqueous droplet will not penetrate due to the high interfacial force [102].

After the phase separation is achieved, the phenol trace in the aqueous phase needs to be addressed because it would interfere with downstream steps. The second part of this dissertation was initially proposed to solve this phenol contamination. Next, a summary of the conclusions and future work of the second part of this work is presented and how the phenol decontamination can be approached using a buffer exchange module using transverse electrokinetic forces.

6.2 DNA trapping by electrokinetic forces

Conclusions

Sample pre-concentration can be a critical element to improve sensitivity of integrated microchip assays. In this work a converging Y-inlet microfluidic channel with integrated coplanar electrodes was used to investigate transverse DNA and protein migration under uniform direct current (DC) electric fields to assess the ability to concentrate a sample prior to other enzymatic modifications or capillary electrophoretic separations. Employing a pressure-driven flow to perfuse the microchannel, negatively charged samples diluted in low and high ionic strength buffers were co-infused with a receiving buffer of the same ionic strength into a main daughter channel.

Experimental results demonstrated that, depending of the buffer selection, different DNA migration and accumulation dynamics were seen. Charged analytes could traverse the channel width and accumulate at the positive bias electrode in case of a high ionic strength buffer with low electroosmotic mobility and high electrophoretic mobility, or migrated towards an equilibrium position within the channel when using a low ionic strength buffer with high electroosmotic mobility and high electrophoretic mobility. The various migration behaviors are the result of a balance between the electrophoretic force and a drag force induced by a recirculating electroosmotic flow generated across the channel width due to the bounding walls.

Under continuous flow conditions, DNA samples were concentrated up to 4-folds by trapping in electrodes and 3-folds by balancing transverse electrokinetic forces. The trapping mechanism was demonstrated and reproduced several times using low voltages

(3V) to produce DC fields but also it was observed when using pulsed fields. The DNA reached the steady state position in less than 15 seconds.

The electrokinetic trapping technique presented here is a simple technique which just involves a set of coplanar electrodes and low-voltage requirements allowing two different behaviors depending of the electrolyte solution selection.

Future work

This work demonstrated, for the first time, that DNA and protein samples could be trapped and concentrated under continuous flow conditions by balancing a DC electrophoretic force with the electroosmotic flow force. Such a mechanism could be used as a pre-concentration method prior to DNA loading into a CE separation column. The trapping behavior makes this technique suitable for concentration enhancements of dilute solutions to improve detection.

Approaches will be taken to suppress the non-specific absorption of DNA and/or protein onto the channel surfaces without modifying the wall zeta potential to allow better DNA concentration quantification. This work will also seek to infuse a low concentration DNA solution below the fluorescence detection limit in order to concentrate the DNA to a level that can be detected via epifluorescence microscopy.

A better understanding of the trapping mechanism needs to be addressed to provide the possibility of controlling concentration enhancement and location across the channel in order to expand this technique to concentration or separation of other analytes for downstream processes. This could be explored by different ways. First, the ionic strength

of TE buffer can be varied to investigate the DNA trapping as the ionic strength increases and the electroosmotic drag force gets weaker. Second, the DNA electrophoretic force can be also modified by varying the NaCl salt concentration to study the force balance. Third, the development of high fidelity numerical tools can simulate complex, nonlinear electrokinetic phenomena by coupling electromigration fluxes of all species with the predicted electroosmotic and hydrodynamic flow profiles.

Additionally, the transverse electrokinetic force can be used to solve the phenol contamination problem found in the aqueous phase in the first part of this work. As mentioned previously, high light absorption at low wavelengths (<300 nm) was detected in aliquots of the aqueous phase following the phenol extraction impeding DNA purity quantification by spectrophotometry. To eliminate this contamination, a buffer exchange module can be added after the phase separation to wash and collect DNA in a clean buffer. The device presented in the second part of this work can be used to force the DNA sample to travel to the opposite electrode into a clean receiving buffer. For this buffer exchange application, the device walls needs to be treated first to avoid the generation of electroosmotic flow and assure that DNA is only affected by the electrophoretic force.

Finally, future work will also explore the utilization of the helical electroosmotic flow to improve the efficiency of DNA modifying enzyme reactions (restriction endonucleases, ligases, polymerases, etc.) by infusing them in the receiving buffer and mixing them with the DNA solution for an integrated reaction control.

Bibliography

1. Lui, C., N. Cady, and C. Batt, *Nucleic Acid-based Detection of Bacterial Pathogens Using Integrated Microfluidic Platform Systems.* Sensors, 2009. **9**(5): p. 3713-3744.
2. Lagally, E.T., C.A. Emrich, and R.A. Mathies, *Fully integrated PCR-capillary electrophoresis microsystem for DNA analysis.* Lab Chip, 2001. **1**(2): p. 102-107.
3. Easley, C.J., et al., *A fully integrated microfluidic genetic analysis system with sample-in-answer-out capability.* P. Natl. Acad. Sci. USA, 2006. **103**(51): p. 19272-19277.
4. Kohlheyer, D., et al., *Miniaturizing free-flow electrophoresis - a critical review.* Electrophoresis, 2008. **29**(5): p. 977-993.
5. Sommer, G.J. and A.V. Hatch, *IEF in microfluidic devices.* Electrophoresis, 2009. **30**(5): p. 742-757.
6. Sambrook, J., E.F. Fritsch, and T. Maniatis, *Molecular Cloning: A Laboratory Manual*. 1989, NY: Cold Spring Harbor Laboratory Press.
7. Qiagen, *QIAprep Miniprep Handbook*. 2003: Qiagen Distributors
8. Christel, L.A., et al., *Rapid, automated nucleic acid probe assays using silicon microstructures for nucleic acid concentration.* J. Biomech Eng, 1999. **121**(1): p. 22-7.
9. McMillan, W.A., et al. *Application of advanced microfluidics and rapid PCR to analysis of microbial targets*. in *Proceedings of the 8th international symposium on microbial ecology*. 1999.
10. Breadmore, M.C., et al., *Microchip-Based Purification of DNA from Biological Samples.* Anal. Chem., 2003. **75**(8): p. 1880-1886.
11. Hong, J.W., et al., *A nanoliter-scale nucleic acid processor with parallel architecture.* Nature Biotechnology, 2004. **22**(4): p. 435-9.
12. Wu, Q.R., et al., *Microchip-based macroporous silica sol-gel monolith for efficient isolation of DNA from clinical samples.* Anal. Chem., 2006. **78**(16): p. 5704-5710.
13. Wen, J., et al., *Microfluidic-Based DNA Purification in a Two-Stage, Dual-Phase Microchip Containing a Reversed-Phase and a Photopolymerized Monolith.* Anal. Chem., 2007. **79**(16): p. 6135-6142.

14. Kulinski, M.D., et al., *Sample preparation module for bacterial lysis and isolation of DNA from human urine.* Biomed. Microdevices, 2009. **11**(3): p. 671-678.

15. Bhattacharyya, A. and C.M. Klapperich, *Microfluidics-based extraction of viral RNA from infected mammalian cells for disposable molecular diagnostics.* Sensors Actuat B: Chem, 2008. **129**(2): p. 693-698.

16. Chen, X., F. Cui da, and C.C. Liu, *On-line cell lysis and DNA extraction on a microfluidic biochip fabricated by microelectromechanical system technology.* Electrophoresis, 2008. **29**(9): p. 1844-1851.

17. Hagan, K.A., et al., *Chitosan-Coated Silica as a Solid Phase for RNA Purification in a Microfluidic Device.* Anal. Chem., 2009. **81**(13): p. 5249-5256.

18. Witek, M.g.A., et al., *Purification and preconcentration of genomic DNA from whole cell lysates using photoactivated polycarbonate (PPC) microfluidic chips.* Nucleic Acids Res. **34**(10): p. e74.

19. Reddy, V. and J.D. Zahn, *Interfacial stabilization of organic-aqueous two-phase microflows for a miniaturized DNA extraction module.* J Colloid Interface Sci, 2005. **286**(1): p. 158-65.

20. Mao, X., S. Yang, and J. Zahn. *Experimental Demonstration and Numerical Simulation of Organic-Aqueous Liquid Extraction Enhanced by Droplet Formation in a Microfluidic Channel*. in *Proceedings of the ASME-IMECE*. 2006. Chicago, IL.

21. Zahn, J. and V. Reddy, *Two phase micromixing and analysis using electrohydrodynamic instabilities.* Microfluidics Nanofluidics, 2006. **2**(5): p. 399-415.

22. Morales, M. and J. Zahn. *Development of a Diffusion Limited Microfluidic Module for DNA Purification via Phenol Extraction*. in *Proceedings of the ASME IMECE*. 2008. Boston, MA

23. Morales, M. and J. Zahn, *Droplet enhanced microfluidic-based DNA purification from bacterial lysates via phenol extraction.* Microfluidics Nanofluidics, 2010.

24. Albertsson, P., *Partition of cell particles and macromolecules*. Third ed. 1986, New York, NY: Wiley.

25. Shui, L., J.C.T. Eijkel, and A. van den Berg, *Multiphase flow in microfluidic systems - Control and applications of droplets and interfaces.* Advances in Colloid and Interface Science, 2007. **133**(1): p. 35-49.

26. Christopher, G.F. and S.L. Anna, *Microfluidic methods for generating continuous droplet streams.* J. Phys. D Appl. Phys., 2007. **40**(19): p. R319-R336.

27. Shui, L., J.C.T. Eijkel, and A. van den Berg, *Multiphase flow in micro- and nanochannels.* Sensors Actuat B: Chem, 2007. **121**(1): p. 263-276.

28. Shui, L., et al., *Multiphase flow in lab on chip devices: A real tool for the future?* Lab Chip, 2008. **8**(7): p. 1010-1014.

29. Atencia, J. and D.J. Beebe, *Controlled microfluidic interfaces.* Nature, 2005. **437**(7059): p. 648-655.

30. Helen Song, D.L.C., Rustem F. Ismagilov,, *Reactions in Droplets in Microfluidic Channels.* Angewandte Chemie International Edition, 2006. **45**(44): p. 7336-7356.

31. Squires, T.M. and S.R. Quake, *Microfluidics: Fluid physics at the nanoliter scale.* Rev. Mod. Phys., 2005. **77**(3): p. 977-50.

32. Nguyen, N.T. and S.T. Wereley, *Fundamentals And Applications of Microfluidics*

Second ed. 2006: Artech House Publishers.

33. Purcell, E.M., *Life at low Reynolds number.* American Journal of Physics, 1977. **45**(1): p. 3-11.

34. Brody, J.P., et al., *Biotechnology at low Reynolds numbers.* Biophys. J., 1996. **71**(6): p. 3430-3441.

35. Dreyfus, R., P. Tabeling, and H. Willaime, *Ordered and Disordered Patterns in Two-Phase Flows in Microchannels.* Phys. Rev. Lett., 2003. **90**(14): p. 144505.

36. Xu, J., et al., *Correlations of droplet formation in T-junction microfluidic devices: from squeezing to dripping.* Microfluidics Nanofluidics, 2008. **5**(6): p. 711-717.

37. Guillot, P. and A. Colin, *Stability of parallel flows in a microchannel after a T junction.* Phys. Rev. E, 2005. **72**(6): p. 066301-4.

38. Tice, J.D., et al., *Formation of Droplets and Mixing in Multiphase Microfluidics at Low Values of the Reynolds and the Capillary Numbers.* Langmuir, 2003. **19**(22): p. 9127-9133.

39. Tice, J., A. Lyon, and R. Ismagilov, *Effects of viscosity on droplet formation and mixing in microfluidic channels.* Analytica Chimica Acta, 2004. **507**: p. 73-77.

40. Hibara, A., et al., *Integrated Multilayer Flow System on a Microchip.* Analytical Sciences, 2001. **17**(1): p. 89-93.

41. Surmeian, M., et al., *Three-Layer Flow Membrane System on a Microchip for Investigation of Molecular Transport.* Anal. Chem., 2002. **74**(9): p. 2014-2020.

42. Tokeshi, M., et al., *Continuous-flow chemical processing on a microchip by combining microunit operations and a multiphase flow network.* Anal. Chem., 2002. **74**(7): p. 1565-1571.

43. Link, D.R., et al., *Geometrically Mediated Breakup of Drops in Microfluidic Devices.* Phys. Rev. Lett., 2004. **92**(5): p. 054503.

44. Masumi Yamada, V.K., Megumi Nakashima, Jun'ichi Edahiro, Minoru Seki,, *Continuous cell partitioning using an aqueous two-phase flow system in microfluidic devices.* Biotechnology and Bioengineering, 2004. **88**(4): p. 489-494.

45. Castell, O.K., C.J. Allender, and D.A. Barrow, *Continuous molecular enrichment in microfluidic systems.* Lab Chip, 2008. **8**(7): p. 1031-1033.

46. Xia, H.M., et al., *Chaotic micromixers using two-layer crossing channels to exhibit fast mixing at low Reynolds numbers.* Lab on a Chip, 2005. **5**(7): p. 748-755.

47. Stroock, A.D., et al., *Chaotic Mixer for Microchannels.* Science, 2002. **295**(5555): p. 647-651.

48. Aref, H., *The development of chaotic advection.* Physics of Fluids, 2002. **14**(4): p. 1315-1325.

49. Liu, R.H., et al., *Passive mixing in a three-dimensional serpentine microchannel.* Microelectromechanical Systems, Journal of, 2000. **9**(2): p. 190-197.

50. Song, H., et al., *Experimental test of scaling of mixing by chaotic advection in droplets moving through microfluidic channels.* Applied Physics Letters, 2003. **83**(22): p. 4664-4666.

51. Sober, H. and R. Harte, *Handbook of Biochemistry. Selected Data for Molecular Biology.* 1st ed. 1968, Cleveland, Ohio: The Chemical Rubber Company,.

52. Xia, Y. and G.M. Whitesides, *Soft Lithography.* Angew. Chem. Int. Edit., 1998. **37**(5): p. 550-575.

53. Haubert, K., T. Drier, and D. Beebe, *PDMS bonding by means of a portable, low-cost corona system.* Lab Chip, 2006. **6**(12): p. 1548-1549.

54. Hibara, A., et al. *Novel Two-Phase Flow Control Concept and Multistep Extraction Microchip*. in *Proceeding of the 12th International Conference on Miniuturized Systems for Chemistry and Life Sciences (μTAS 2008)*. 2008. San Diego, CA.

55. Song, H., D. Chen, and R. Ismagilov, *Reactions in Droplets in Microfluidic Channels.* Angew. Chem. Int. Edit., 2006. **45**(44): p. 7336-7356.

56. Wen, J., et al., *Purification of nucleic acids in microfluidic devices.* Anal. Chem., 2008. **80**(17): p. 6472-6479.

57. Hunter, R.J., *Foundations of Colloid Science*. Vol. 1. 1987, Oxford: Oxford University.

58. Probstein, R.F., *Physicochemical Hydrodynamics*. 2003, Hoboken: Wiley.

59. Tandon, V., et al., *Zeta potential and electroosmotic mobility in microfluidic devices fabricated from hydrophobic polymers: 1. The origins of charge.* Electrophoresis, 2008. **29**(5): p. 1092-1101.

60. Kirby, B.J. and E.F. Hasselbrink, *Zeta potential of microfluidic substrates: 1. Theory, experimental techniques, and effects on separations.* Electrophoresis, 2004. **25**(2): p. 187-202.

61. Tseng, W.L., et al., *Effect of ionic strength, pH and polymer concentration on the separation of DNA fragments in the presence of electroosmotic flow.* J. Chromatogr A, 2000. **894**(1-2): p. 219-230.

62. Spehar, A.-M., et al., *Electrokinetic characterization of poly(dimethylsiloxane) microchannels.* Electrophoresis, 2003. **24**(21): p. 3674-3678.

63. Gaudioso, J. and H.G. Craighead, *Characterizing electroosmotic flow in microfluidic devices.* J. Chromatogr A, 2002. **971**(1-2): p. 249-253.

64. Wu, D., J. Qin, and B. Lin, *Electrophoretic separations on microfluidic chips.* J. Chromatogr A, 2008. **1184**(1-2): p. 542-559.

65. Wu, D., J. Qin, and B. Lin, *Self-assembled epoxy-modified polymer coating on a poly(dimethylsiloxane) microchip for EOF inhibition and biopolymers separation.* Lab Chip, 2007. **7**(11): p. 1490-1496.

66. Xiao, D., T.V. Le, and M.J. Wirth, *Surface Modification of the Channels of Poly(dimethylsiloxane) Microfluidic Chips with Polyacrylamide for Fast Electrophoretic Separations of Proteins.* Anal. Chem., 2004. **76**(7): p. 2055-2061.

67. Stellwagen, N., C., C. Gelfi, and P.G. Righetti, *The free solution mobility of DNA.* Biopolymers, 1997. **42**(6): p. 687-703.

68. Chang, H.C. and L.Y. Yeo, *Electrokinetically driven Microfluidics and Nanofluidics* 2010, New York: Cambridge University Press.

69. Viovy, J.L., *Electrophoresis of DNA and other polyelectrolytes: Physical mechanisms.* Rev. Mod. Phys., 2000. **72**(3): p. 813-872.

70. Stellwagen, E. and N.C. Stellwagen, *The free solution mobility of DNA in Tris-acetate-EDTA buffers of different concentrations, with and without added NaCl.* Electrophoresis, 2002. **23**(12): p. 1935-1941.

71. Stellwagen, E. and N.C. Stellwagen, *Probing the Electrostatic Shielding of DNA with Capillary Electrophoresis.* Biophys. J., 2003. **84**(3): p. 1855-1866.

72. Chang, C.C. and R.J. Yang, *Electrokinetic mixing in microfluidic systems.* Microfluidics Nanofluidics, 2007. **3**(5): p. 501-525.

73. Qian, S. and H.H. Bau, *A Chaotic Electroosmotic Stirrer.* Anal. Chem., 2002. **74**(15): p. 3616-3625.

74. Stroock, A.D., et al., *Patterning Electro-osmotic Flow with Patterned Surface Charge.* Phys. Rev. Lett., 2000. **84**(15): p. 3314.

75. Glasgow, I., J. Batton, and N. Aubry, *Electroosmotic mixing in microchannels.* Lab Chip, 2004. **4**(6): p. 558-562.

76. Song, H., et al., *Chaotic mixing in microchannels via low frequency switching transverse electroosmotic flow generated on integrated microelectrodes.* Lab Chip, 2010. **10**(6): p. 734-740.

77. Fu, L.-M., et al., *A novel microfluidic mixer utilizing electrokinetic driving forces under low switching frequency.* Electrophoresis, 2005. **26**(9): p. 1814-1824.

78. Sasaki, N., T. Kitamori, and H.-B. Kim, *AC electroosmotic micromixer for chemical processing in a microchannel.* Lab Chip, 2006. **6**(4): p. 550-554.

79. Lynn, N.S., C.S. Henry, and D.S. Dandy, *Microfluidic mixing via transverse electrokinetic effects in a planar microchannel.* Microfluidics Nanofluidics, 2008. **5**(4): p. 493-505.

80. Kim, S.J., I.S. Kang, and B.J. Yoon, *Electroosmotic helical flow produced by combined use of longitudinal and transversal electric fields in a rectangular microchannel.* Chem. Eng. Commun., 2006. **193**(9): p. 1075-1089.

81. Burgi, D.S. and R.L. Chien, *Optimization in sample stacking for high-performance capillary electrophoresis.* Anal. Chem., 1991. **63**(18): p. 2042-2047.

82. Bharadwaj, R. and J.G. Santiago, *Dynamics of field-amplified sample stacking.* J. Fluid Mech, 2005. **543**(-1): p. 57-92.

83. Gong, M., et al., *On-Line Sample Preconcentration Using Field-amplified Stacking Injection in Microchip Capillary Electrophoresis.* Anal. Chem., 2006. **78**(11): p. 3730-3737.

84. Jung, B., R. Bharadwaj, and J.G. Santiago, *Thousandfold signal increase using field-amplified sample stacking for on-chip electrophoresis.* Electrophoresis, 2003. **24**(19-20): p. 3476-3483.

85. Huang, H., et al., *On-line isotachophoretic preconcentration and gel electrophoretic separation of sodium dodecyl sulfate-proteins on a microchip.* Electrophoresis 2005. **26**(11): p. 2254-2260.

86. Wainright, A., et al., *Sample pre-concentration by isotachophoresis in microfluidic devices.* J. Chromatogr A, 2002. **979**(1-2): p. 69-80.

87. Breadmore, M.C. and J.P. Quirino, *100 000-Fold Concentration of Anions in Capillary Zone Electrophoresis Using Electroosmotic Flow Controlled Counterflow Isotachophoretic Stacking under Field Amplified Conditions.* Anal. Chem., 2008. **80**(16): p. 6373-6381.

88. Schonfeld, F., et al., *Transition zone dynamics in combined isotachophoretic and electro-osmotic transport.* Physics of Fluids, 2009. **21**(9): p. 11.

89. Monton, M.R.N., et al., *Dynamic pH junction technique for on-line preconcentration of peptides in capillary electrophoresis.* J. Chromatogr A, 2005. **1079**(1-2): p. 266-273.

90. Kohlheyer, D., et al., *Free-flow zone electrophoresis and isoelectric focusing using a microfabricated glass device with ion permeable membranes.* Lab Chip, 2006. **6**(3): p. 374-380.

91. Osafune, T., H. Nagata, and Y. Baba, *Influence of the pH on Separating DNA by High-Speed Microchip Electrophoresis.* Anal. Sci., 2004. **20**(6): p. 971-974.

92. Asbury, C.L., A.H. Diercks, and G. van den Engh, *Trapping of DNA by dielectrophoresis.* Electrophoresis, 2002. **23**(16): p. 2658-2666.

93. Asbury, C.L. and G. van den Engh, *Trapping of DNA in nonuniform oscillating electric fields.* Biophys J., 1998. **74**(2): p. 1024-1030.

94. Wang, L., et al., *Dielectrophoresis switching with vertical sidewall electrodes for microfluidic flow cytometry.* Lab Chip, 2007. **7**(9): p. 1114-1120.

95. Fiedler, S., et al., *Dielectrophoretic Sorting of Particles and Cells in a Microsystem.* Anal. Chem., 1998. **70**(9): p. 1909-1915.

96. Du, J.-R., et al., *Long-range and superfast trapping of DNA molecules in an ac electrokinetic funnel.* Biomicrofluidics, 2008. **2**(4): p. 044103-10.

97. Liu, P., et al., *Integrated DNA purification, PCR, sample cleanup, and capillary electrophoresis microchip for forensic human identification.* Lab Chip. **11**(6): p. 1041-1048.

98. Hatch, A.V., et al., *Integrated Preconcentration SDS-PAGE of Proteins in Microchips Using Photopatterned Cross-Linked Polyacrylamide Gels.* Anal. Chem., 2006. **78**(14): p. 4976-4984.

99. Foote, R.S., et al., *Preconcentration of Proteins on Microfluidic Devices Using Porous Silica Membranes.* Anal. Chem., 2004. **77**(1): p. 57-63.

100. Butler, J.N., *Ionic Equilibrium: Solubility and PH Calculations*. 1998 New York: Wiley.

101. Almutairi, Z.A., et al., *A Y-channel design for improving zeta potential and surface conductivity measurements using the current monitoring method.* Microfluidics Nanofluidics, 2009. **6**(2): p. 241-251.

102. Niu, X.Z., et al., *Droplet-based compartmentalization of chemically separated components in two-dimensional separations.* Chemical Communications, 2009(41): p. 6159-6161.

103. Shrewsbury, P.J., S.J. Muller, and D. Liepmann, *Effect of Flow on Complex Biological Macromolecules in Microfluidic Devices.* Biomed. Microdevices, 2001. **3**(3): p. 225-238.

Appendix A

Microfluidic Channel and Electrode Fabrication

Photolithography process using SU-8 2010 and 2050 Negative Photoresist

- Soak substrate (glass or silicon) in acetone, isopropanol and deionized (DI) water baths for 10 minutes each.
- Rinse with DI water and blow dry with nitrogen or filtered air.
- Dehydrated the glass slides at a 150°C for 30 minutes in an oven and let to cool before spinning.
- Dispense the photoresist on the substrate trying to avoid bubbles and overload the substrate that can lead to chuck groove obstruction.
- Spin conditions: for 20 μm (SU-8 2010): 30 sec at 1000 rpm, for 50 μm (SU-8 2050): 30 sec at 1600 rpm.
- Soft-bake for SU-8 2010: 1 minute at 65°C and 4 minutes at 95°C on a hotplate. For SU-8 2050: 2 minutes at 65°C and 6 minutes at 95°C.

- Expose photoresist to UV light using the appropriate recipe for the substrate selected.
- Post-Exposure bake for SU-8 2010: 1 minute at 65°C and 2 minutes at 95°C on a hotplate. For SU-8 2050: 1 minute at 65°C and 4 minutes at 95°C on a hotplate.
- Develop photoresist by immersing slide in SU-8 developer with gentle agitation. For SU-8 2010: 3 minutes. SU-8 2050: 8 minutes.
- Gently rinse the slide with isopropanol.
- Gently dry the glass slide using an air gun.

Silanization

- This process is convenient to help the release of the PDMS from the master and preserve the photoresist.
- Place the clean master in a vacuum chamber together with a clean glass slide with 100 μl of trichloro (1, 1, 2, 2-perfluoocytl) silane for 30 minutes.

Soft lithography process

- Mix 10 parts of PDMS base and 1 part of PDMS crosslinker.
- Pour PDMS mix on top of the master.
- Place it in vacuum chamber to remove air bubbles.
- Cure for 1 hour at 65 C.

- Punch hole on all inlets and outlets.
- Clean and rinse PDMS and glass surfaces with acetone, then isopropanol, then DI water.
- Dry both part thoroughly with filtered compressed air.
- Bond by treating bonding surfaces with corona discharge or using a plasma generator at for 1 minute.
- Align PDMS channel over glass slide. Place the device in oven at 65°C for 1 hour to allow bonding.

Photolithography process using S1818 (Shipley)

- Clean the glass substrate as in the SU-8 protocol.
- Deposit 3-4 drops of hexamethyldisilazane (HDMS) to prime the surface and spin at 3000 rpm.
- Deposit S1818 and spin at 3000 rpm.
- Soft bake at 120°C for 4 minutes and let it cool.
- Expose the photoresist using the Shipley recipe (applying 150 mJ/cm^2).
- Develop in MF-319 for 1-4 minutes.
- Rinse with DI water and blow dry.
- Hard bake: place the substrate in an oven at 120°C for 30 minutes. Let it cool.

- Glass etching: rinse the slide in a bath of buffered hydrofluoric acid (5:1) for 1 minute (Caution: special safety standard operating procedure is required to handle hydrofluoric acid)

Metal Deposition

- Turn on the chiller, open air valve and vent.
- Load the samples.
- Start to pump down and allow pressures to reach between $1x10^{-6}$ to $5x10^{-7}$ torr.
- Then set turbo pump speed to 50% and let it spin down to 80% or less before opening up the argon valve.
- Start platen rotation (10RPM). Turn on motor and select FWD.
- Set the appropriate gas flow rates on the computer. The mass flow controller for argon is MFC1 and set it to 100 sccm. Then open up the valve on the screen.
- Once the turbo pump reaches 50% and the pressure has stabilized, set deposition power settings for the sputtering gun to be used. Turn on SWITCH for the appropriate gun, turn on POWER, then wait 30 sec to 1 min to remove impurities from the target surface.
- Then open the SHUTTER while starting the stopwatch. Sputtering settings: titanium: 4.5 minutes at 200 W, platinum: 10 minutes at 200 W.
- When ready, stop deposition: in this order, close the SHUTTER, turn off the POWER, then turn off the gun SWITCH (all done on-screen).

- Close the gas switch on-screen and shut off argon valve on the wall, behind the machine (leave the air valve ON). Stop all-motion button.
- Wait 5 minutes to let the gas get out of the chamber and then vent.
- Remove platen from machine and remove specimens from the platen. Place platen back into the machine.
- Start pumping and let complete the pumping cycle.
- Turn off these components in this SPECIFIC order: Turbo pump, valve, roughing pump.
- Shut all of the gas valves on the wall, including the house air and turn off recirculation pump.

Appendix B

Sample Preparation and Measurements

BSA Labeling

First, 5-6-carboxy-tetramethylrhodamine (TAMRA) succinimidyl ester dye (Fluka, Switzerland) is dissolved in Dimethyl Sulfoxide (DMSO) (Amresco, Solon, OH) to a concentration of 10 mg/ml. BSA is separately dissolved in PBS to a concentration of 50 mg/ml. Then, the amount of dye to be added to the BSA solution is calculated using the following equation:

$$V_{Rhod}[\mu l] = \frac{C_{BSA} \times V_{BSA}}{MW_{BSA}} \times MW_{Rhod} \times 100 \times MR \tag{B.1}$$

where C_{BSA} is the concentration of BSA in mg/ml and V_{BSA} is the volume in ml of the BSA solution. MW_{BSA} is the molecular weight of the protein, 66000 Daltons, and MW_{Rhod} is the molecular weight of the dye, 527.53 Daltons. MR is the molar ratio of dye to protein. A ratio of 10 was used for this labeling.

The dye solution is added to the protein solution and covered with aluminum foil to keep it out of light. The solution is mixed using a rotary shaker for 30 minutes.

Then, the labeled solution needs to be filtered through a PD-10 desalting column (Sephadex G-25M; GE Healthcare) to remove the free dye from the solution. After removing the top cap of the column and pour off the excess liquid, equilibration of the column with 25 ml PBS buffer is required. Labeled solution is added to the column, and then, same amount of buffer is added and the output is discarded. Finally, buffer is eluted and the output flow is collected with the labeled proteins. The solution could be stored at -20˚C or diluted to the needed concentration. In this project, the concentration used was 0.3 mg/ml.

Spectrophotometry measurements

The samples were loading into the 1ml spectrophotometer cuvette and the reading was taking as a scanning from 250 to 600 nm. Then, the protein concentration can be calculated by the following equation:

$$C_{BSA} = \frac{[A_{280} - (A_{585} \times K)] \times DF}{\varepsilon} \times MW_{BSA} \quad \text{(B.2)}$$

Where A_{280} and A_{585} are the UV-light absorption of the protein solution at 280 and 585 nm; DF is the dilution factor; ε is the extinction coefficient that for BSA is approximately 43,824 M^{-1} cm^{-1}.

DNA Staining

YOYO-1 was intercalated within the DNA backbone at a ratio of one molecule of dye per five base pairs of DNA (1:5), similarly as described in Shrewsbury et al paper [103]. The

average molecular weight of the base pair used was 650 grams/bp mole. The DNA was diluted in TE buffer (10 mM tris-HCl, 1 mM EDTA, from Rockland Inc., Gilbertsville, PA). The dye solution was added conjunctly with β-mercaptoethanol, an oxygen scavenger that protect DNA-dye complex from oxygen radicals, at a final concentration of 4% (v/v). The incubation of DNA and the dye occurred at room temperature in the dark and for a minimum of two hours. The final DNA concentration was 0.075 μg/μl.

Bacteria Transformation, Bacteria Plate and Liquid Culture

- The bacteria transformation was performed using Bio-Rad pGLO bacterial transformation kit following protocol from Bio-Rad (http://www.bio-rad.com/LifeScience/pdf/Bulletin_9563.pdf).
- The bacteria culture in plates was done in 1.5% (LB) agar, 2% arabinose, 100 μg/ml ampicillin pre-poured plates from Teknova.
- Prepare a starter culture by picking a colony from a plate and incubate in tube with 3ml of Luria Broth (LB), 300 μl of Arabinose at 2% and 3 μl of ampicillin at 100 μg/μl. Incubate for 8 hours.
- To make a fresh plate culture, take 50 μl from the starter culture and diluted in 200 μl of LB. Then using a loop, streak the plate as it is shown Qiagen Bench Guide (http://www.qiagen.com/literature/benchguide/pdf/1017778_benchguide_chap_1.pdf). Incubate for 12-14 hours until colonies develop.

- To make a liquid culture, take 10 µl from the starter culture and diluted in culture tube with 3ml of LB, 300 µl of Arabinose at 2% and 3 µl of ampicillin at 100µg/µl concentration. Incubate for 12-14 hours.

DNA Gel Electrophoresis

- Prepare 0.8 liter of 1× Tris acetate EDTA (TAE) buffer in a cylinder.
- In flask, prepare 1% agarose solution by mixing 1 gram and 100 ml of 1× TAE buffer.
- Then heat the solution in a microwave oven until completely melted.
- After cooling the solution to about 60˚C, it is poured into a casting tray. Add the sample comb and allowed to solidify at room temperature.
- After the gel has solidified, remove the side walls of the casting tray and place the casting tray with the gel in the electrophoresis box. Add the rest of the TAE buffer to cover the gel.
- Remove the comb, using care not to rip the bottom of the wells.
- Samples containing DNA mixed with loading buffer are then pipetted into the sample well on the negative electrode side (black electrode).
- The lid and power leads are placed on the apparatus, and voltage is applied (120 V). DNA will migrate towards the positive electrode which is usually colored red. Stop the migration once the loading dye migrated half of the gel length.
- Bring the gel to the ethidium bromide bath and turn on the shaker for 15 minutes.

- Place the gel into the UV illuminator and obtain pictures of the gel.

Appendix C

COMSOL Simulation Parameters

Model Tree and Mesh

- Select MEMS module, then Microfluidics and Electroosmotic Flow and finally Stokes Flow and Steady State analysis.
- It will open the following branches in the model tree: Stokes Flow and Conductive Media DC.
- Import AutoCAD drawing and mesh it completely and re-mesh for a finer mesh near the electrode corners.

Subdomain Settings for Stokes Flow

- In Physics tab: ρ=1000, η=.001, F_x=F_y=0, Thickness=1.
- In Microfluidic tab: ε_r=80, λ=1e-6.

Boundary Settings for Stokes Flow

- Set all boundaries conditions to “Electroosmotic Velocity”.

- In Electroosmotic Velocity tab: in all set $E_x=E_{x\_emdc2}$, $E_y=E_{y\_emdc2}$, electroosmotic mobility at the electrode equal to zero, electroosmotic mobility at glass and PDMS walls according to buffer selected (Table 5.2).

Subdomain Settings for Conductive Media DC

- In Physics tab: σ isotropic=.0739, thickness=1.

Boundary Settings for Stokes Flow

- Select "Electric Insulation" except for the electrodes and set them to 0 V and 3 V potentials.

Solver

- First get the initial value from "Solve" tab. Then go to "Solver parameter" and set Spooles.
- Go to Solver manager, "Initial Value" tab. Click in "Values of variables not solved for and linearization point" the option "Use setting from initial value frame". Then go to "Solve for" tab and select Stokes and Conductive Media, then apply.
- Go to "Script" tab and add current solver settings. Click "Solve using a script" and solve. This will solve Stokes and Conductive Media DC together.
- Repeat these steps in case you want to solve again.

Curriculum Vitae

MERCEDES C. MORALES

Education

2012	PhD in Biomedical Engineering, Rutgers, The State University of New Jersey.
2008	Master of Science in Biomedical Engineering, Rutgers, The State University of New Jersey.
2004	Electromechanical Engineering degree, concentration in Industrial Automation, Universidad Nacional de La Pampa (Argentina).

Experience

2010-2011	Teaching Graduate Assistant, Rutgers, The State University of New Jersey.
2007-2010	Research Graduate Assistant, Rutgers, The State University of New Jersey.
2004-2005	Research Assistant, Universidad Nacional de La Pampa (Argentina).

Journal Publications

- **M. C. Morales,** H. Lin and J. D. Zahn. "Continuous microfluidic DNA and protein trapping and concentration by balancing transverse electrokinetic forces", Lab on a Chip, 2011, DOI: 10.1039/C1LC20605B.
- **M. C. Morales,** J. D. Zahn. "Droplet Enhanced Microfluidic-based DNA Purification from Bacterial Lysates via Phenol Extraction", Microfluidics and Nanofluidics, 2010, 9:1041-1049.